

Chapter II.10

Particle sources

Thomas Thuillier

Laboratory of Subatomic Physics and Cosmology (CNRS-LPSC), Grenoble, France

The particle sources create the beam which will next be used in accelerators. The chapter proposes an introduction to particle sources physics and technology. It starts with basics on the beam emittance formation from particle sources and how to filter unwanted low energy beams prior to their acceleration to high energy. The next part proposes an introduction to the three existing electron sources types and their basics of physics: thermionic, field emission and photo-emission electron guns. The chapter continues with a short introduction to the exotic beam production, taking the example of positron sources. The last part is dedicated to ion sources. After a presentation of the physics processes used to produce positive and negative ions, the main different families of ion sources are shortly presented.

II.10.1 Introduction

Particle sources are the instruments specifically designed to generate the accelerators beams. The physics covered by this topic is very large and choices had to be made to fit within a limited content size. The chapter is divided into four sections. The first section focuses on the basics of beam extraction from particle sources. The second section is dedicated to electron sources and introduces the three main electron gun families: thermionic, field emission and photoemission. Each subsection starts with an introduction to the specific physics behind the extraction of electron from matter. The third section proposes a short introduction of sources of exotic beams, taking the example of positron sources. The last section is dedicated to ion sources, it starts with an introductory part dedicated to the ion creation and ion confinement. Next, a selection of ion sources families are presented: surface, arc discharge, photoionization, negative and finally multi-charged ion sources.

II.10.2 Particle beam formation and filtering

II.10.2.1 Initial kinetic energy

Figure II.10.1 presents a generic particle source beam extraction and its connection to a low-energy beam line. The source includes a boundary surface S where a charged-particle flow is available at very low energy (usually of the order of eV). The inner part of the source and the way of creating particle flow is very specific and is not presented here, but later in this chapter. The collection of particles available at

This chapter should be cited as: Particle sources, T. Thuillier, DOI: [10.23730/CYRSP-2024-003.1529](https://doi.org/10.23730/CYRSP-2024-003.1529), in: Proceedings of the Joint Universities Accelerator School (JUAS): Courses and exercises, E. Métral (ed.), CERN Yellow Reports: School Proceedings, CERN-2024-003, DOI: [10.23730/CYRSP-2024-003](https://doi.org/10.23730/CYRSP-2024-003), p. 1529.
© CERN, 2024. Published by CERN under the [Creative Commons Attribution 4.0 license](https://creativecommons.org/licenses/by/4.0/).

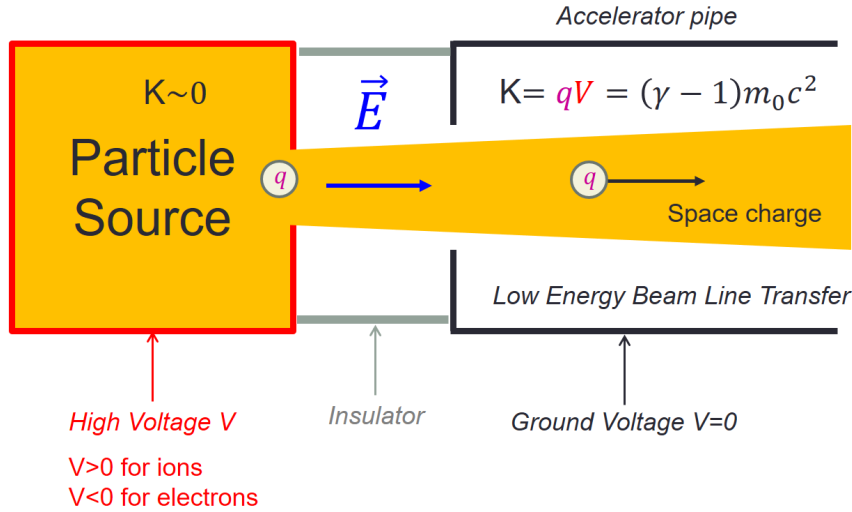


Fig. II.10.1: Sketch of a simple particle beam extraction system from a particle source.

extraction per unit of time can be modeled by

$$\Phi = \int \int_S n(x, y, z) \vec{v}(x, y, z) \cdot d\vec{S}, \quad (\text{II.10.1})$$

where $n(x, y, z)$ is the density of particle available close to the source extraction boundary and $\vec{v}(x, y, z)$ is the local particle velocity. The particle source is generally set to a high-voltage potential V . In its simplest design, the area of beam extraction (particle source electrode) is facing a ground electrode set to the accelerator beam pipe potential. The difference of potential generates a static electric field which accelerates the particle up to the kinetic energy $K = qV$ where q is the particle electric charge. The usual magnitude of high-voltage spans in the range 1-100 kV.

II.10.2.2 Source beam emittance

The build-up of a source beam emittance is a rather complex process. The total transverse beam emittance from a particle source after its initial acceleration can be modelled by the quadratic sum of three terms [1]

$$\epsilon_{tot}^2 = \epsilon_S^2 + \epsilon_{SC}^2 + \epsilon_B^2, \quad (\text{II.10.2})$$

where ϵ_S is the beam emittance due to the particle initial conditions at the source (see Sec. II.10.2.2.1), ϵ_{SC} is the contribution of space charge effect which inflates the beam while it's accelerating to reach its final kinetic energy K (see Sec. II.10.2.2.2) and ϵ_B is the magnetic emittance (explained in Sec. II.10.2.2.3).

II.10.2.2.1 Initial source beam emittance

The 1- σ normalized transverse beam emittance at the source along the direction x is

$$\epsilon = \gamma\beta\sigma_x \cdot \sigma_{x'}, \quad (\text{II.10.3})$$

where γ and β are the usual relativistic Lorentz factors, $\sigma_{x'}$ is the standard deviation of particle momentum at the source

$$\sigma_{x'} = \frac{\sqrt{\langle p_x^2 \rangle - \langle p_x \rangle^2}}{p}, \quad (\text{II.10.4})$$

where p_x is the initial transverse momentum at the source along the x axis and $p = \gamma\beta mc$ (with m the mass at rest and c the speed of light) is the particle momentum after the initial acceleration by the high-voltage V ,

$$\sigma_x = \sqrt{\langle x^2 \rangle - \langle x \rangle^2}, \quad (\text{II.10.5})$$

where σ_x is the standard deviation of the particles position along the transverse direction x integrated on the emissive surface; note that this surface is not necessarily planar or uniformly distributed. In the case of particles following the Boltzmann statistics with a temperature T , one can find that

$$\sigma_{x'} = \frac{1}{\gamma\beta} \sqrt{\frac{kT}{mc^2}}, \quad (\text{II.10.6})$$

where k is the Boltzmann constant. Typical σ_x values for usual emissive source surfaces are proposed in Table II.10.1.

Table II.10.1: Example of root mean squares (RMS) applicable to calculate beam emittances.

circular disk with radius R	$\sigma_x = \frac{R}{2}$
slit extraction with width a (along x)	$\sigma_x = \frac{a}{\sqrt{12}}$

II.10.2.2.2 Space charge beam emittance

The particles are usually created in the source at low energy . The first acceleration stage to reach the source extraction kinetic energy K takes a time Δt . During this time, the particles electric charge repels one from each other, inducing an unavoidable emittance growth ϵ_{SC} due to space charge effect. In the case of an uniform round beam density from the source, the radial electric field acting on individual particles in a continuous beam with intensity I and radius r_0 is

$$F_r(r) = \begin{cases} \frac{qI}{2\pi v(t)} \frac{r}{r_0^2}, & \forall r \leq r_0 \\ \frac{qI}{2\pi v(t)} \frac{1}{r}, & \forall r > r_0 \end{cases}, \quad (\text{II.10.7})$$

where $v(t)$ is the particle axial velocity during the initial beam acceleration phase from $t = 0$ to Δt . The spatial beam growth due to space charge can be approximated for a specific particle source by integrating the equation of motion of individual particles located at the beam edge during their time of acceleration Δt considering the forces from Eq. II.10.7. For an initial round beam at the source with radius r_0 , the beam size will inflate to a higher radius $r_{\Delta t}$ after the time Δt , leading to a transverse emittance relative growth by a factor $\sim \frac{r_{\Delta t}}{r_0}$.

II.10.2.2.3 Magnetic emittance

When the beam is emitted from the source in the presence of a magnetic field, a new term for the emittance appears named the magnetic emittance. This section proposes a step-by-step calculation to retrieve its formula which is not detailed in books. The general expression of the classical Lagrangian of a charged particle in a static electromagnetic field is

$$L = \frac{1}{2}mv^2 - qV + q\vec{v}\cdot\vec{A},$$

where \vec{A} is the potential vector defined as $\vec{B} = \text{curl}(\vec{A})$. If one assumes that the magnetic field is uniform in space $\vec{B} = B\vec{e}_z$, then $\vec{A} = \frac{1}{2}Br\vec{e}_\theta$, where the vectors are expressed in the usual cylindrical coordinate system $(\vec{e}_r, \vec{e}_\theta, \vec{e}_z)$. The Lagrangian of an individual particle at position $\vec{OM} = r\vec{e}_r + z\vec{e}_z$ and velocity $\vec{v} = \dot{r}\vec{e}_r + r\dot{\theta}\vec{e}_\theta + \dot{z}\vec{e}_z$, expressed in cylindrical coordinates, reduces to

$$L = \frac{1}{2}m(\dot{r}^2 + \dot{z}^2 + r^2\dot{\theta}^2) - qV + \frac{q}{2}Br^2\dot{\theta}.$$

The canonical momenta are

$$P_r = \frac{\partial L}{\partial \dot{r}} = m\dot{r} = p_r,$$

$$P_z = \frac{\partial L}{\partial \dot{z}} = m\dot{z} = p_z,$$

$$P_\theta = \frac{\partial L}{\partial \dot{\theta}} = mr^2\dot{\theta} + \frac{q}{2}Br^2 = p_\theta r + \frac{q}{2}Br^2,$$

where p_r , p_z and p_θ are the usual particle momentum in cylindrical coordinates. The associated Hamiltonian expressed as a function of the canonical momenta is

$$H = \frac{1}{2m}[P_r^2 + P_z^2 + (\frac{P_\theta}{r} - \frac{q}{2}Br)^2] + qV.$$

By definition, $\dot{P}_\theta = -\frac{\partial H}{\partial \theta}$. H is not explicitly function of θ , therefore P_θ is a constant of motion. This is known as the Busch's theorem. Now, let us apply this result to a particle source including an axial magnetic field of intensity B_0 at the source extraction, parallel to the accelerator axis. There, $P_\theta = mr^2\dot{\theta} + \frac{q}{2}B_0r^2$. In usual sources, the initial particle velocity is small and related to room temperature energies: $p_\theta \ll \frac{q}{2}B_0r$ and $P_\theta \sim \frac{q}{2}B_0r^2$. In the reasoning below, we consider that the particles are emitted from a uniformly populated disk of radius R . Once the particles have passed the extraction system and have been accelerated up to the kinetic energy $K = qV$, they reach the final momentum p along the z axis and propagate forward in the beam pipe. At some distance, the ion source magnetic fringe field finally goes down to zero. There, the azimuthal canonical momentum of an individual particle reduces to $P_\theta = rp_\theta$, leading to $p_\theta = \frac{q}{2}B_0r$. Assuming that the whole beam is still included in a uniformly populated disk of radius R and considering that $p_x = -p_\theta \sin \theta$, we can now calculate $\sigma_{x'}$ (using Eq. II.10.4)

$$\sigma_{x'} = \frac{qB_0 R}{2p} \frac{R}{2}.$$

Finally, the $1\text{-}\sigma$ RMS normalized magnetic emittance for a beam extracted from an uniformly populated disk of radius R , with a local magnetic field intensity B_0 is

$$\epsilon_B = \frac{qB_0}{2mc} \left(\frac{R}{2}\right)^2.$$

II.10.2.3 Child-Langmuir current limitation and perveance

In the case of a high-current density extraction from a particle source, the space charge carried by the beam generates an electric field which inflates it radially (emittance growth) and reduces the electric field intensity used to extract the beam. A current extraction limitation arises when the net electric field available at the source extraction becomes null (i.e. when the space charge electric field totally screens the static extraction electric field). In the case of a one-dimension infinite planar extraction system, the Maxwell equations in the presence of beam current can be solved exactly. Figure II.10.2(c) presents the geometry of the beam extraction model solved. On the left, particles are emitted at the position $z = 0$ with a potential $V = 0$ and are accelerated toward the plane $z = 1$ where the potential is V . When no particle is present into the accelerating gap, the potential profile is linear and the electric field is constant (see the dashed plots in Fig. II.10.2(a) and (b) respectively). In the presence of the charged beam, the voltage profile in the gap is distorted along with the electric field. At the current density limit J , the charges accumulated in the gap are so high that the electric field, necessary to extract particles from the left plane becomes zero. The Child-Langmuir formula associated with this limit is

$$J \leq \frac{4\epsilon_0}{9} \sqrt{\frac{2q}{m}} \frac{V^{3/2}}{d^2}, \quad (\text{II.10.8})$$

where ϵ_0 is the vacuum permittivity and d is the gap distance. In the case of a real three-dimensions extraction system, the current limitation has the general expression

$$J \leq PV^{3/2},$$

where P is the perveance specific for each extraction system. In the case of an axi-symmetric extraction, very common for particle sources, one can demonstrate that the perveance has the following general expression

$$P = \frac{C}{d^2},$$

where C is a constant.

II.10.2.4 Beam filtering

In the case of ion sources, the beam of interest is generally extracted with a large quantity of unwanted beam that it is necessary to filter as soon as possible. For positive ion sources, the unwanted beams can be ionized air residues present under vacuum, like molecules H_2O^+ , OH^+ , H_2^+ , H_3^+ , H_2^+ , O_2^+ , N_2^+ , CO^+ , etc, or any multi-charged ion derived from the associated atoms in the case of multi-charged ion source. Symmetrically, a negative ion source will co-extract electrons along with the negative ion of interest and possibly other negative ion molecules or atoms. A classical way to filter the beam of interest is by passing it through a bending magnet (dipole) with a tunable magnetic field intensity B and a fixed

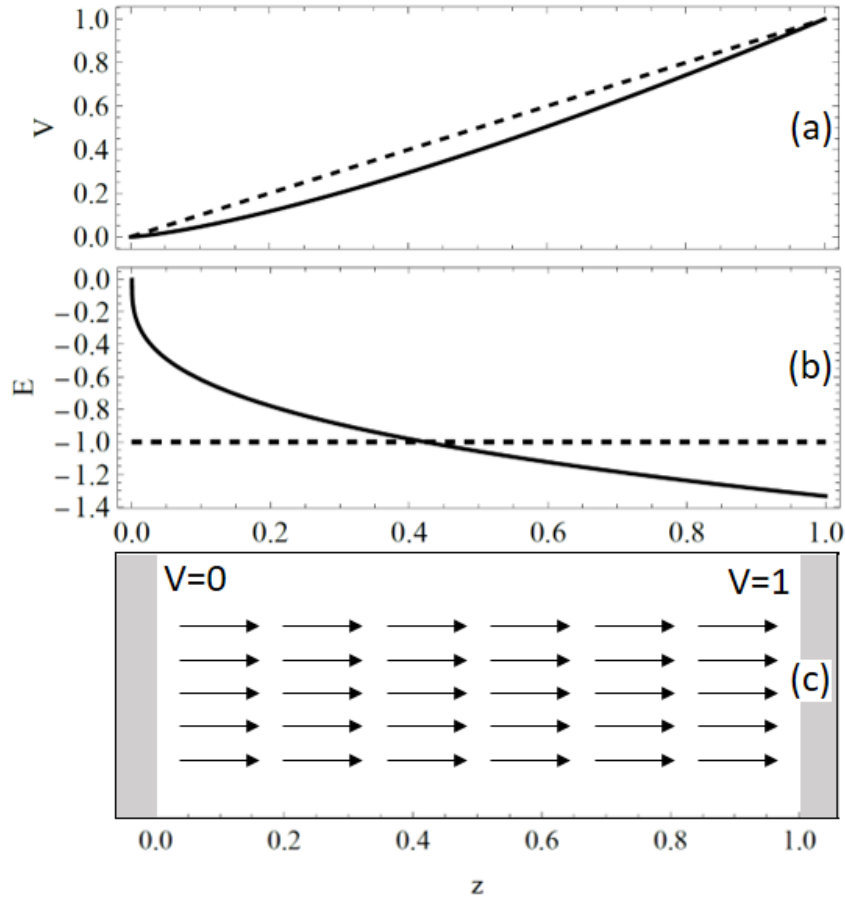


Fig. II.10.2: (a) Voltage profile in the acceleration gap without beam (dashed line) and at the Child-Langmuir limit (solid line). (b) Electric field profile in the acceleration gap without beam (dashed line) and at the Child-Langmuir limit (solid line). (c) Sketch detailing the one-dimension extraction system for which the exact Child-Langmuir formula is obtained. The arrows represent the general particle flow.

mechanical radius ρ . The filtering equation is, for the non relativistic case

$$B\rho = \frac{mv}{q}. \quad (\text{II.10.9})$$

Remembering that $\frac{1}{2}mv^2 = qV$, where V is the ion source high-voltage, one can see that ions are separated according to their mass over charge ratio

$$\rho = \text{const} = \sqrt{\frac{m}{q} \frac{\sqrt{2V}}{B}}. \quad (\text{II.10.10})$$

Usual low-energy dipoles have a mass resolution of the order of $\frac{m}{\Delta m} \sim 100$, while high-resolution ones can reach a few 1000. Figure II.10.3 presents a typical low-energy beam transfer line (LEBT) using a dipole to filter the beam of interest. When adding a detector at the dipole exit, ramping the magnetic field in the dipole allows to record the mass over charge spectrum of species extracted from the source. Another common device to filter ion beams is the Wien filter presented in Fig. II.10.4. Here two metallic plates are polarized to form a transverse electric field $\vec{E} = E\vec{y}$ perpendicular to the beam. A magnetic

field $\vec{B} = -B\vec{x}$ is superimposed at the electric field. A beam with charge q and velocity $\vec{v} = v\vec{z}$ will pass without deviation through the device provided the sum of the electric and magnetic forces compensate exactly

$$\vec{F}_B + \vec{F}_E = q(-vB + E)\vec{y} = \vec{0}. \quad (\text{II.10.11})$$

The condition is fulfilled when $v = \frac{E}{B}$. The Wien filter separates beams according to their velocities. In usual LEBT, the use of a Wien filter is applicable to low-intensity beams and with a mass separation $\frac{m}{\Delta m} < 10$.

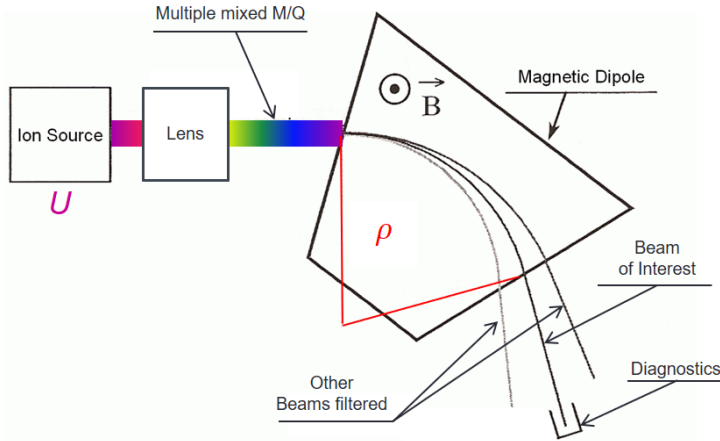


Fig. II.10.3: Dipole magnet filtering coupled to an ion source. The beam of interest is filtered and sent to a diagnostics.

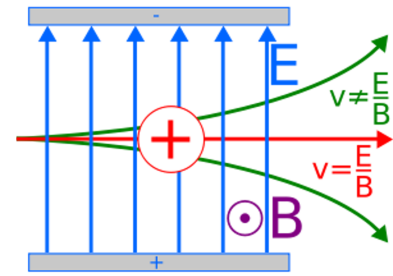


Fig. II.10.4: Sketch of a Wien filter.

II.10.2.5 Particle extraction from a plasma

Many particle sources generate the beam of interest from a plasma under vacuum. The plasma is usually contained into a metallic cavity (the plasma chamber) set to a high-voltage. The beam is usually extracted from the plasma by means of a plasma electrode equipped with a circular hole (see Fig. II.10.5) facing an electrostatic extraction system (see also Sec. II.10.2.1). While extracting particles from a solid surface results in a perfectly defined particle emission location and electric potential geometry, the situation is more complicated with a plasma. The plasma is composed of ions, electrons and neutral atoms. The plasma is quasi-neutral at a macroscopic scale: its core is iso-potential with an electric potential V_p with respect to the walls surrounding it. If the plasma chamber wall is set to a potential V , then the particles inside the plasma core have the potential $V + V_p$. V_p is self-consistently adjusted by the plasma to balance the net charged-particle flux losses to the walls to zero. Because electrons are lighter than ions, electrons move faster than ions and thus escape faster from the plasma. The loss of electrons results in the build up of a positive plasma potential. A positive plasma potential reduces the electron flux to the wall (by decelerating electrons and pushing the colder ones backward), while it accelerates ions to the wall. An important parameter of a plasma is the Debye length λ_D which is approximated by Eq. II.10.12 when the ion temperature T_i is much smaller than the electron one T_e

$$\lambda_D \sim \sqrt{\frac{\epsilon_0 k T_e}{n_e e^2}}, \quad (\text{II.10.12})$$

where e is the electron electric charge and n_e the electron density. λ_D is the characteristic distance

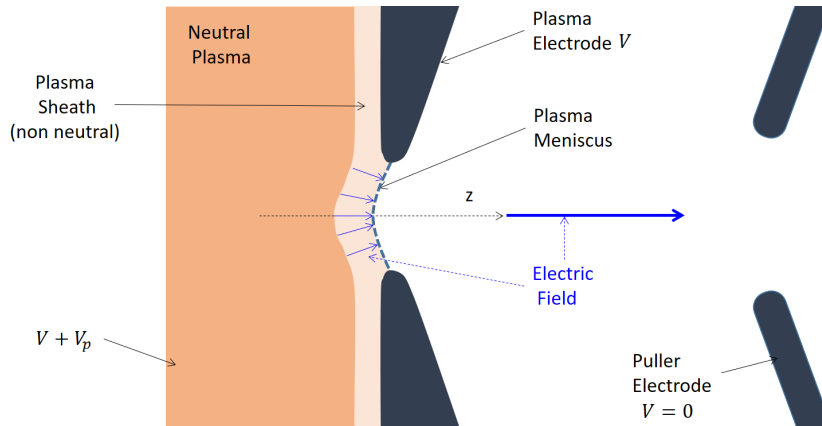


Fig. II.10.5: Sketch presenting the main parameters involved in the particle extraction from a plasma.

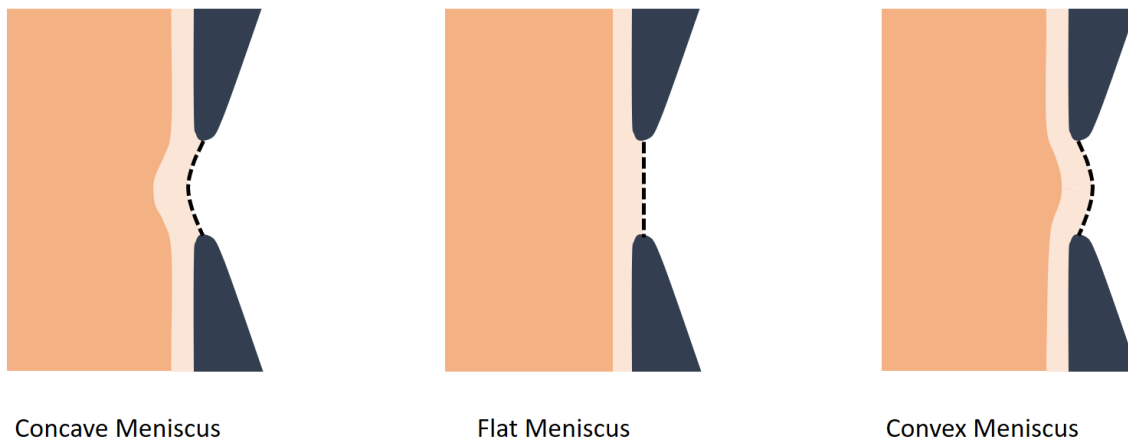


Fig. II.10.6: Illustration of the three possible plasma meniscus curvatures: concave, flat and convex. This change of curvature significantly changes the beam initial conditions from a plasma and hence the beam emittance formation.

below which the plasma is no more neutral and subject to local electric fields. In typical laboratory plasma, λ_D ranges in 0.01-1 mm. The plasma is surrounded by a sheath with a thickness of a few λ_D . It is inside the plasma sheath that the difference of potential with the wall, V_p creates an electric field which acts on the charged particles. The boundary between the plasma and the accelerator is immaterial and the sheath geometry is self-consistently adapted by the plasma. The shape of the sheath in contact with the plasma electrode is named the plasma meniscus. Depending on the charged-particle density, energy, flux, the meniscus shape can be either convex, flat or concave (see Fig. II.10.6). In the case of a homogeneous non-magnetized plasma at thermal equilibrium, theoretical considerations imply that incoming ions entering the sheath must have a minimum velocity v_B

$$v_B \geq \sqrt{\frac{kT_e}{m_i}}, \tag{II.10.13}$$

where m_i is the ion mass of species i . This inequality is known as the Bohm sheath criterion. Modeling the beam extraction from a plasma requires to consider either a prescribed plasma meniscus or solving the plasma boundary using a sophisticated code. The plasma potential value and the meniscus shape strongly change the initial extraction condition of particles from the plasma and any simulation result must be considered with caution as long as an experimental confirmation is not done.

II.10.3 Electron sources

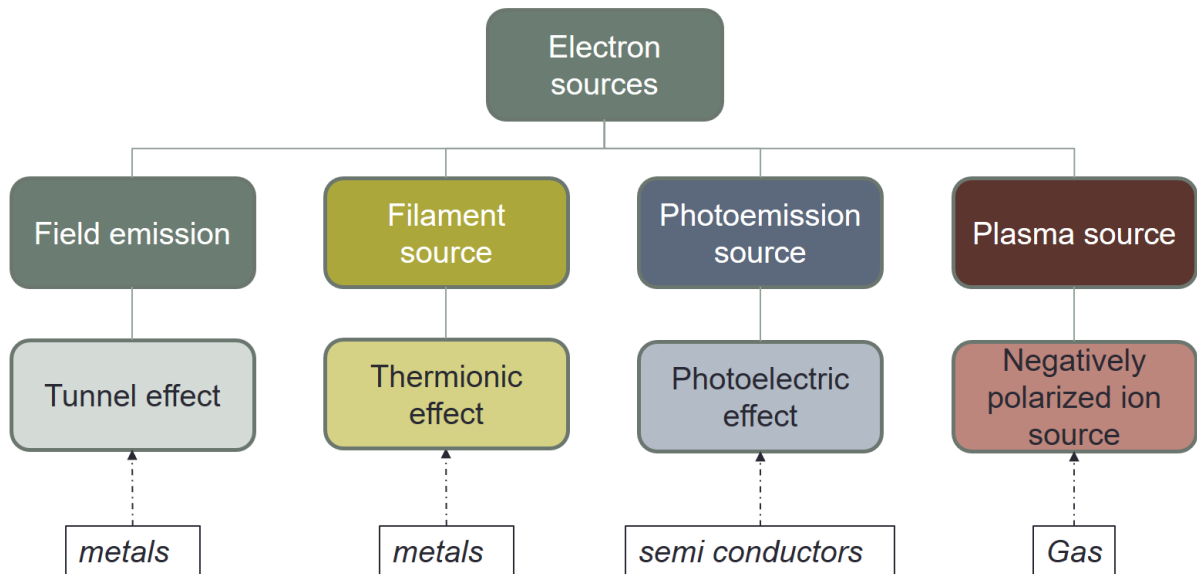


Fig. II.10.7: Overview of the different electron source families used in lepton accelerators.

Figure II.10.7 proposes an overview of the main electron source families: filament, field emission, photo-emission and plasma source. The three first families from the left are presented below, preceded by an introduction to the basics of physics. The fourth method indicated in Fig. II.10.7 corresponds to electron beam extraction from a plasma. This specific technique is indicated for completion but is not common and not detailed in this section, though it is possible and easy to produce hundreds of mA of electrons from a simple commercial plasma ion source by reversing the voltage polarity and adapting its extraction system [2]. A reference proposing an overview of electron source is [3].

II.10.3.1 Thermionic electron sources

A convenient way to produce an electron beam is by using the thermionic emission. When a metal or metal-oxyde is heated, the thermal vibrations of the atoms in the lattice are partially transferred to the conduction band electrons which can populate excited states, above the Fermi level E_F (energy counted from the ground level of the material). Electrons are then naturally emitted out of the material when their final energy E is higher than the work function W . The thermionic emission is the resulting flow of electrons extracted from the heated material. The electron energy density distribution in matter follows

the Fermi-Dirac statistics

$$\frac{d^4 N_e}{dE d^3 V} = g(E)F(E) = g(E) \frac{1}{1 + e^{\frac{E-E_F}{kT}}}, \quad (\text{II.10.14})$$

where $g(E)$ is the density of state in matter and $F(E)$ is the Fermi function. An illustration on how $F(E)$ changes with temperature is presented in Fig. II.10.8. The vertical black dashed line stands for the work function of the material above which an electron will be naturally freed from the material. The

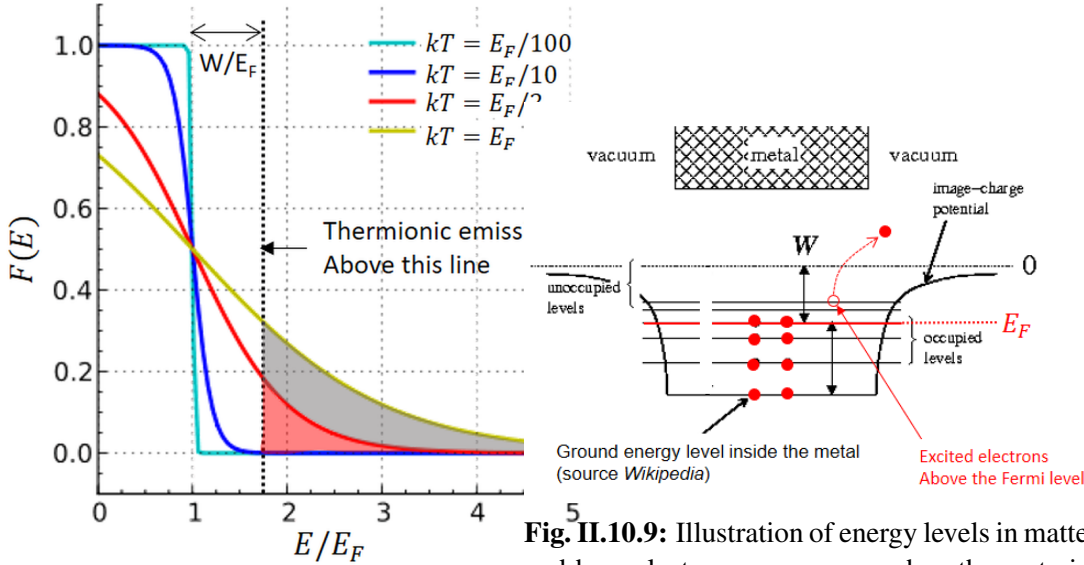


Fig. II.10.8: Evolution of the electron energy distribution function in material as a function of its temperature. The energy is normalized to E_F .

Fig. II.10.9: Illustration of energy levels in matter and how electrons can escape when the material is heated.

density of electrons that can be extracted by thermionic effect is given by

$$J = \langle \rho_e v_z \rangle, \quad (\text{II.10.15})$$

where $\rho_e = eg(E)F(E)$ is the charge density distribution and v_z is the velocity of electrons extracted from the hot matter flat surface along the arbitrary chosen z direction. The condition for electron escape is met when

$$\frac{1}{2} m_e v_z^2 \geq W, \quad (\text{II.10.16})$$

which allows to express now

$$J = \iiint_{v_z \geq \sqrt{\frac{2W}{m_e}}} v_z g(v) F(v) dv_x dv_y dv_z. \quad (\text{II.10.17})$$

Because the electrons meeting the extraction condition are in the hottest energy part of the Fermi distribution tail, it is possible to approximate $F(E)$ by the Maxwell-Boltzmann statistics and calculate the

integral. After a long calculation, one can derive the Richardson Dushman-equation

$$J = \frac{4\pi m_e k^2 e}{h^3} T^2 e^{-W/kT}, \quad (\text{II.10.18})$$

where h is the Planck constant. This equation reproduces well the experimental temperature dependence of the current density, but a correction must be brought to the constant term $A_0 = \frac{4\pi m_e k^2 e}{h^3}$ to account for electric surface effects like oxidation or active layer depositions, not considered in the theory. The correction consists in replacing A_0 by $A = A_0 \lambda$ where λ is the material correction factor [4]. Usual values of A are displayed in Table II.10.2. Typical current density evolutions with the temperature are proposed in Fig. II.10.10. Thermionic electron sources are widely used both in industry and accelerator physics.

Table II.10.2: Work function and correction to the Richardson-Dushman coefficient for usual materials used to produce electron source cathode.

Material	W [eV]	λ	$A = A_0 \lambda$ [A cm ⁻² K ⁻²]
Molybdenum	4.15	0.46	55.2
Nickel	4.61	0.25	30
Tantalum	4.12	0.5	60
Tungsten	4.54	0.5	60
Barium	2.11	0.5	60
Cesium	1.81	1.33	159.6
Iridium	5.4	1.42	170.4
Platinum	5.32	0.27	32.4
Rhenium	4.85	0.83	99.6
Thorium	3.38	0.58	69.6
Ba on W	1.56	0.01	1.2
Th on W	2.63	0.02	2.4
Thoria	2.54	0.02	2.4
Cs-oxide	0.75	0.00008	0.0096
TaC	3.14	0.0025	0.3
LaB6	2.4	0.24	28.8

Depending on the electron source design, the electron beam intensity spans from nA to ~ 100 A. An example of thermionic source applied to scanning electron microscope (SEM) is presented in Fig. II.10.11. Its beam current range of operation is nA to μ A. The electron source is set under vacuum. A tungsten filament is heated by a current power supply until it reaches the thermionic emission condition. The filament is polarized by a main negative high-voltage power supply. A tunable resistor allows to fine tune the difference of potential between an intermediate electrode named the Wenhelt and the filament. In front of the Wenhelt is localised and extraction electrode set to the ground potential. Tuning the resistor allows to reach the condition to get a beam cross over in the acceleration gap, of importance for SEM. Figures II.10.12(a) and (c) show examples of high-intensity, high-perveance, high-compression electron source photos and design [5]. The hot cathode has a spherical shape, the Wenhelt is widely opened and the ground electrode shape is calculated to create a radial electric field in the source which exactly compensates the one of the beam space charge (geometry optimisation known as the "Pierce geometry", or

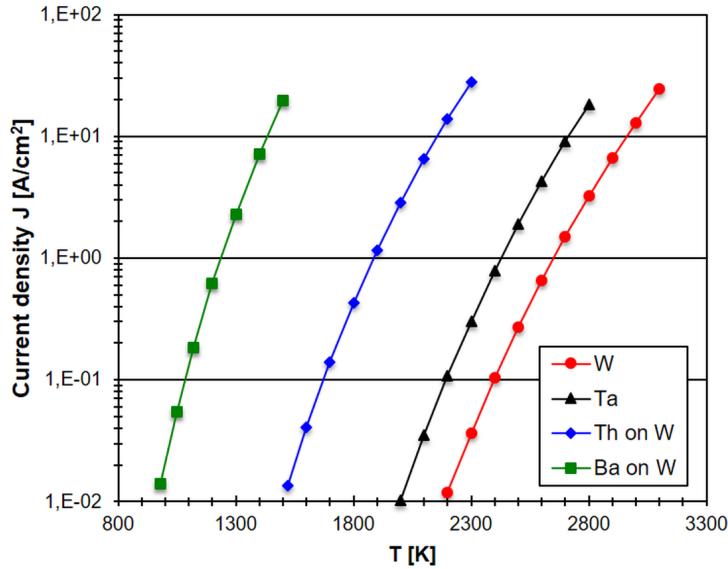


Fig. II.10.10: Thermionic emission electron current density as a function of the temperature for W, Ta, Th on W, Ba on W.

the "Pierce angle"). Intensities up to ~ 100 A are reachable with such technologies. The general limitation of thermionic guns is the filament aging caused by the fact that the electron beam ionizes the residual gas in the accelerator pipe: the ions generated are accelerated toward the electron source and bombard the cathode (sputtering). The lifetime of a filament before it breaks is in the range 10-10000 hours, depending on the design and the condition of operation. Example of cathode damaged by sputtering is shown on Fig. II.10.12(b).

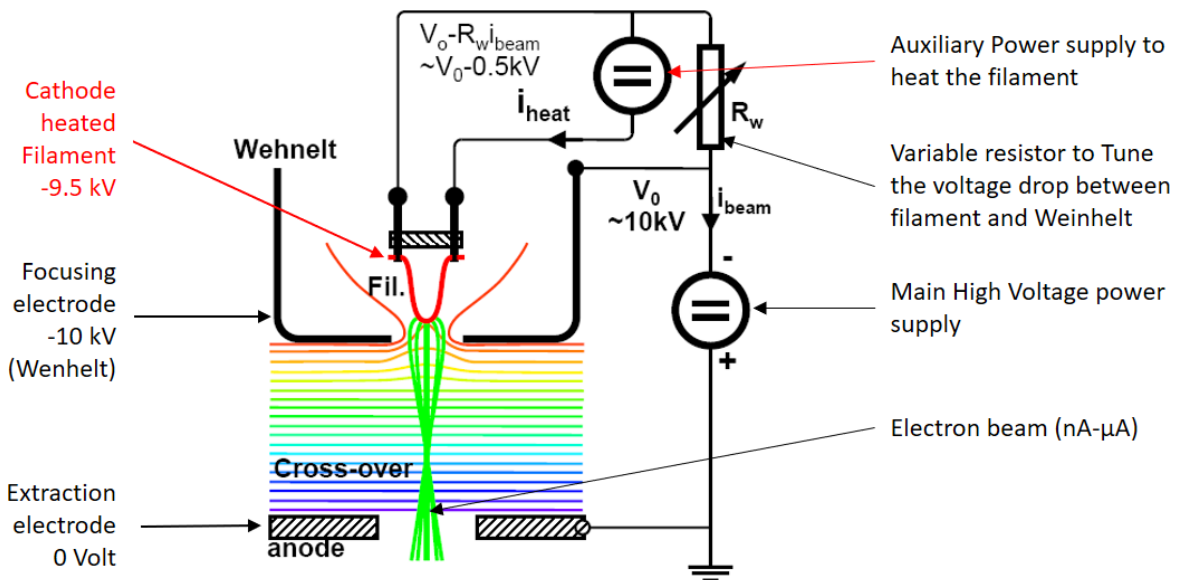


Fig. II.10.11: Thermionic electron source applied to SEM. Partial material re-used from P. Buffat lecture: Microscopie Electronique 2006/2007, EPFL, CH.

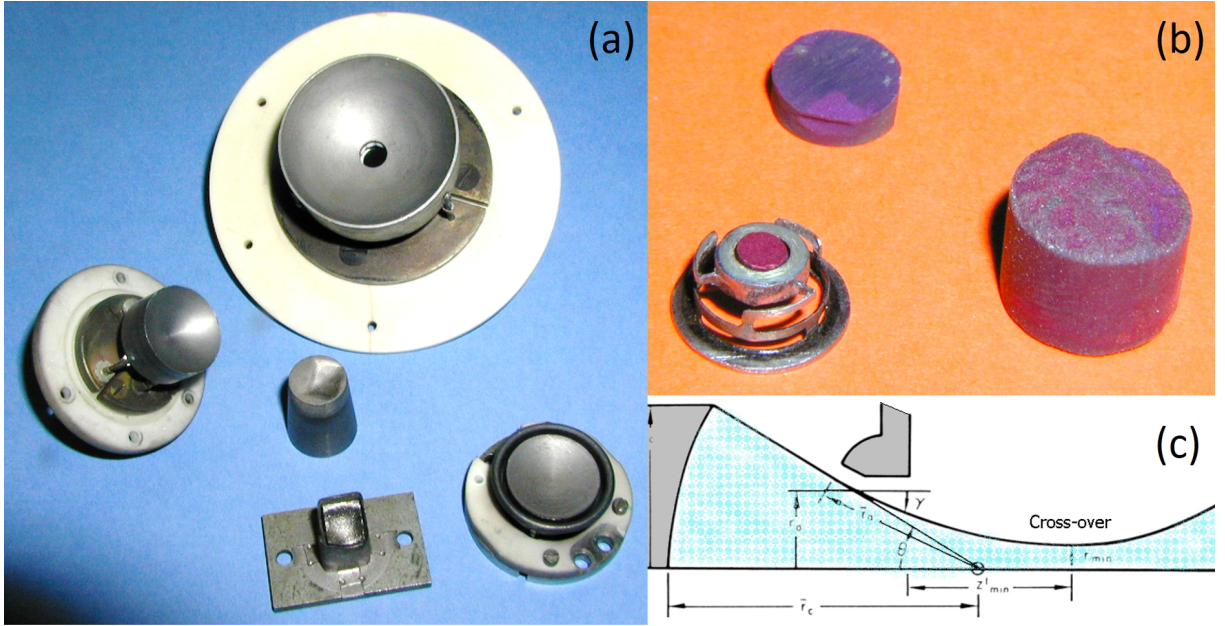


Fig. II.10.12: (a) Photos of high-intensity thermionic guns with a spherical cathode. (b) Photos of thermionic gun cathode damaged by sputtering. (c) Sketch of a high-perveance high-compression thermionic electron source with a spherical cathode. Courtesy of J. Arianer, CNRS-IN2P3.

II.10.3.2 Field emission electron sources

When a conductive solid material is set to an externally applied electric field E perpendicular to its surface, the evolution of the electric potential seen by an electron escaping the metal (from the Fermi energy level) as a function of the distance z to the surface is

$$V(z) = \frac{W}{e} - \frac{e}{16\pi\epsilon_0 z} - E \cdot z. \quad (\text{II.10.19})$$

W is the material work function, while the second term in Eq. II.10.19 stands for the charge image: when an electron escapes the material, a positive hole is present in the material resulting in a local voltage opposing to the electron extraction. The third term corresponds to the externally applied electric field potential. The resulting voltage profile seen by the electron is illustrated in Fig. II.10.13 for two values of E . The presence of the externally applied electric field decreases the potential (and energy) required to extract an electron from the material. The reduction of the work function in the presence of an externally applied electric field (from W down to W_S) is known as the Schottky effect. The associated energy drop is found by solving $\frac{dV}{dz}(z_S) = 0$ from Eq. II.10.19, leading to the position and energy formulas

$$z_S = \sqrt{\frac{e}{16\pi\epsilon_0 E}},$$

$$W_S = \sqrt{\frac{e^3 E}{4\pi\epsilon_0}}.$$

Practical values for W_S and z_S are included in Table II.10.3. A thermionic gun, as presented earlier, will operate with an external electric field of the order of 10^5 V/m, a value easy to achieve with an electrostatic extraction system in continuous working operation. In this case the Schottky effect is negligible ($W_S \ll W$). In the case of a thermionic gun coupled to an accelerating cavity (device known as a RF gun [6], see also Sec. II.10.3.3), the electric field is increased to higher values and the electron work function is reduced. In this case, for a given cathode temperature, the current density of the electron source is increased as in the Eq. II.10.18 (the work function W is replaced by $W - W_S$). When the electric field is increased up to 10^9 V/m, the work function drops by 1.2 eV (see an illustration with the red curve in Fig. II.10.13) and, more importantly, the electric potential barrier close to the material boundary is so narrow (of the order of a nanometer) that now, a bound electron can escape the matter by tunnel effect. In this case, there is no need to heat the material: electrons are emitted spontaneously. The emission is referenced to as a cold cathode emission, or field emission (FE). The quantum mechanics theory explaining the field emission was developed by Fowler and Nordheim in 1928 [7]. A practical formula predicting the current density of field emission can be derived from the theory

$$J = \frac{k_1 E^2}{\phi} e^{-\frac{k_2 \phi^{3/2}}{E}} \quad (\text{II.10.20})$$

with $k_1 = 1.4 \cdot 10^6$ (I.S.), $k_2 = 6.87 \cdot 10^7$ (I.S.) and $\phi = W - W_S$. Field emission electron sources [8] are experimentally achieved by shaping the material electrode to a very sharp tip. When setting a high-voltage to the tip cathode, the electric field is amplified as the inverse of the tip radius end, yielding electron field emission. An example of application of FE is the electron microscope illustrated in Fig. II.10.14. Progresses in micro-electronics allowed the development of arrays of FE cathode known as the Spindt array [9]. In this technology, an array of micrometer size tips is fabricated on a substrate, along with an insulator layer and a metallic upper gate electrode, as illustrated in Fig. II.10.15. Typical experimental currents per molybdenum made tip range in 50-150 μA , with a gate voltage in the range of 50-300 V. One can also cite the ongoing research to develop FE based on carbon nanotubes [10], yielding 1 μA per tube. The safe field emission source requires a very low vacuum level, as in the presence of residual gas in the vicinity of the cathode tip, a breakdown can occur which would damage the tip. The presence of adsorbed gas can also perturbate the electron emission. Jensen proposes a handy formula to calculate the $1\text{-}\sigma$ normalized emittance from a field emission electron source, derived from the Fowler-Nordheim theory [11]

$$\epsilon = \rho_e \sqrt{\frac{2E_F}{m_e c^2}} \left[\frac{4E_F}{\hbar F} (2m_e W)^{1/2} t(y) - 1 \right]^{-1/2}, \quad (\text{II.10.21})$$

where F is the electric force on the cathode, W the cathode work function, E_F the Fermi energy, $t(y) \cong 1 + \frac{1}{9}y^2(1 - \ln(y))$ with $y = \frac{\sqrt{\alpha_f s \hbar c}}{W}$ and α_f is the fine structure constant.

II.10.3.3 Photoemission electron sources

Electron extraction from matter can be done by means of the photoelectric effect [12]. There, an incident photon transfers its energy to a bound electron that can subsequently escape the material. The electron extraction from the material is named photoemission while the electron is called a photoelectron. The

Table II.10.3: Example of Schottky energy and distance for various externally applied electric fields.

E [V / m]	W_S [eV]	z_S [m]	application
10^5	0.03	$1.9 \cdot 10^{-8}$	Thermionic gun
10^6	0.12	$6 \cdot 10^{-9}$	Schottky thermionic gun
10^9	1.20	$6 \cdot 10^{-10}$	Field emission gun

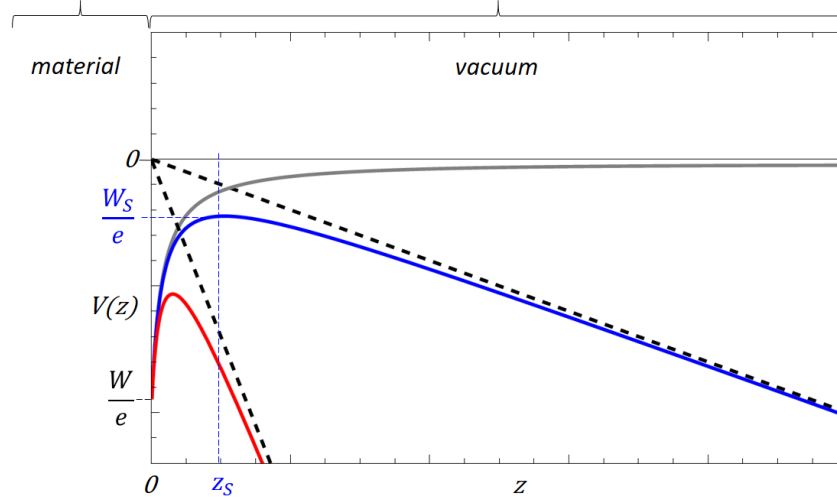


Fig. II.10.13: Evolution of the electric potential at the vicinity of a conductor with an external electric field applied. Grey plot: image charge potential. Blue plot: medium electric field applied. Red plot: High electric field applied. W is the work function, W_S and z_S are the Schottky energy and distance respectively. See text for details.

general scheme to produce an electron beam using photoemission is to hit the material, the photocathode, with an intense and focused pulsed laser beam which results in the emission of a pulse of electrons. The beam is next either accelerated by a DC or a RF electric field toward the accelerator. In the following section, the basics of the electrons photoemission physics are explained. The photocathode materials are presented with their pros and cons and finally a few examples of photoguns are shown.

A sketch presenting the general structure of electron energy levels in a material is presented in Fig. II.10.16. E_{VBM} and E_{CBM} are the energy valence band maximum and the energy conduction band minimum. The difference between E_{VBM} and E_{CBM} is the gap energy E_{gap} and E_F is the Fermi level. When E_F is located in the gap, the material is a semi conductor, while if it is in the valence band, it is a conductor. E_{VAC} is the vacuum energy barrier that prevents electrons in the conduction band from escaping from the material surface. E_{VAC} strongly depends on the properties of the material surface. The energy affinity (EA) is defined as the difference between E_{VAC} and E_{CBM} . I is the ionization energy required to extract an electron from the valence band to the vacuum. The simplest model of photoemission is a one-step process defined by the following energy balance

$$h\nu = I + \frac{1}{2}m_e v^2, \quad (\text{II.10.22})$$

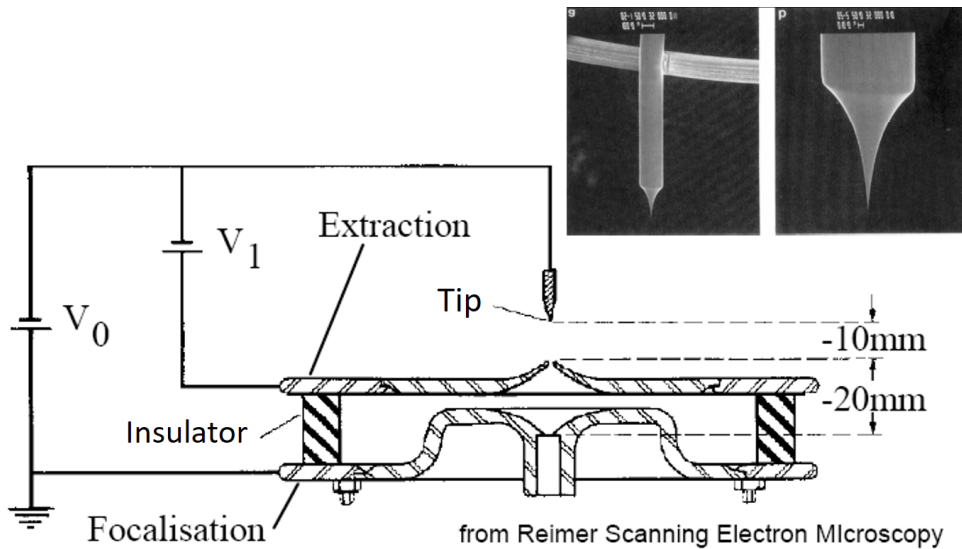


Fig. II.10.14: Layout of a field emission electron source extracted from Reimer lecture, electron spectroscopy. Photos of a cathode tip are presented on the upper right corner.

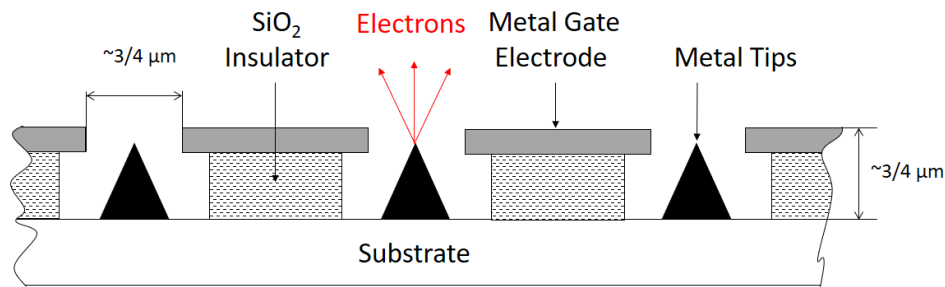


Fig. II.10.15: Layout of a Spindt array design.

where $h\nu$ is the incident photon energy and $\frac{1}{2}m_e v^2$ is the final electron kinetic energy out of the material. In this model, the electron is directly emitted and does not interact with the material before reaching the vacuum level. In many cases, this model is insufficient to reproduce experimental electron emittance and a three-step model is used instead [13], which is as follows: (i) electrons excitation from the valence to the conduction band, (ii) diffusion of the excited electrons through the conduction band, characterized by an energy loss and an increase in the electron energy dispersion, (iii) reaching the surface and escaping the E_{VAC} barrier. An important parameter of photoemission from a photocathode is the quantum efficiency (QE) defined as the ratio between the number of produced electrons and the number of impinging photons. Photocathode use is limited by their dark current, being the spontaneous emission of electron from the cathode in the absence of incoming light. The dark current strongly depends on the purity and the cleanliness of the photocathode. Usual photocathodes applied to electron sources are either made of metals or semiconductors. Metal photocathodes are usually done in Mg, Pb, Cu. They are characterized by a low QE of the order of 0.1%. These metals work functions are quite high (3.6, 4.3, 4.6 eV respectively) and require an ultraviolet laser to extract electrons. The main advantage of metal photocathodes is their very long lifetime (several years) and a quite easy preparation before operation

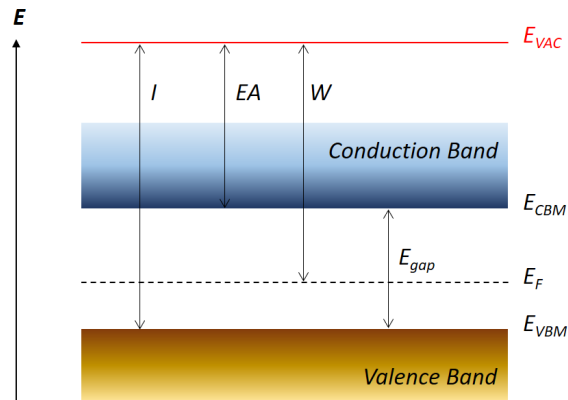


Fig. II.10.16: Sketch presenting the photoemission energy parameters from a material.

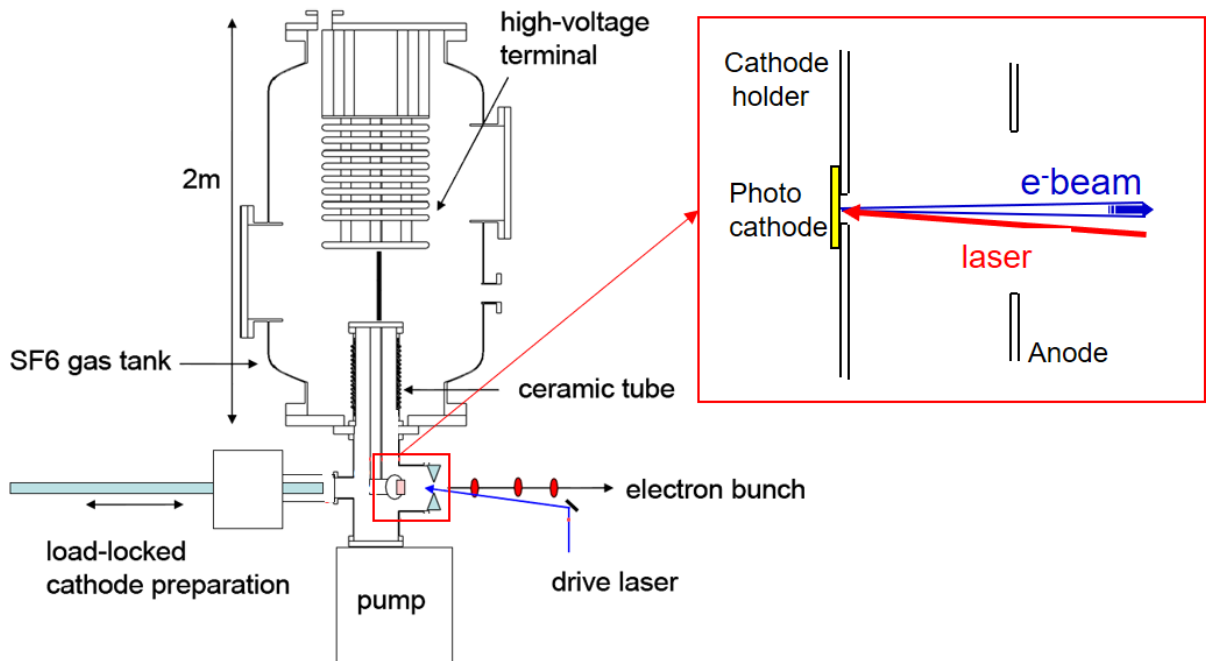


Fig. II.10.17: Conceptual design of the JAEA DC gun [14]. See text for details.

with respect to semiconductor photocathodes, as explained below. Semiconductor photocathodes material usually include an alkali metal in their chemical formula like Cs, K and Na whose work functions are low (2.14, 2.29 and 2.36 respectively). The semiconductor photocathodes are characterized by a low positive electron affinity EA (like Cs_2Te) or even a negative EA when photocathodes (like GaAs or GaN) are coated with cesium plus an oxidant (like O or NF_3). For this latter case, it means that the energy level E_{VAC} is located in the semiconductor energy gap, making the electron emission much easier. The QE of semiconductor cathodes is high and ranges typically in 1-10%. The photoemission from photocathodes is very sensitive to their cleanliness and systematically requires an ultra-high-vacuum for a sustainable operation on accelerators. Non evaporable getters are usually installed in the vacuum chamber holding the photocathode to grant a vacuum level of the order of 10^{-12} mbar. Higher vacuum

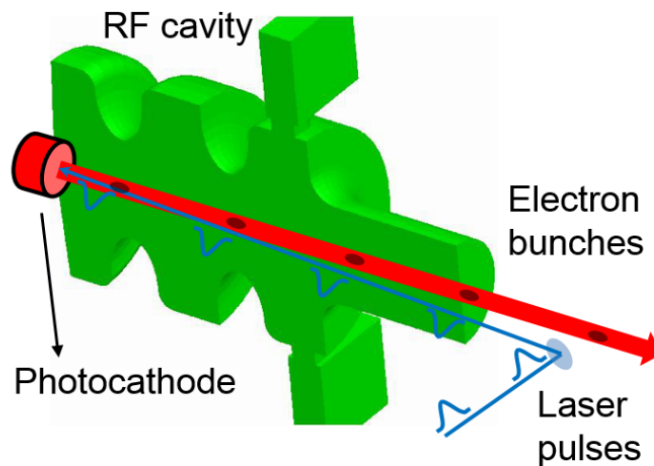


Fig. II.10.18: Conceptual design of a RF gun [16].

level reduces the photocathode lifetime by ion sputtering and cathode chemical contamination by adsorbed polluted gas on the photocathode surface. As an example, the conceptual design of the JAEA DC gun [14] is presented in Fig. II.10.17. The cleaned photocathode is inserted by a load lock system and installed on a cathode holder. The cathode is set to a DC high-voltage (up to 500 kV) fabricated by means of a SF₆ high-voltage terminal. The anode, located in front of the photocathode is set to the ground potential. A 5W DC laser beam, with a 532 nm wavelength, is injected with a small angle with respect to the beam axis [15]. Photoemission can be advantageously coupled to a RF cavity to form a so called RF photogun. A conceptual sketch of a DC gun is proposed in Fig. II.10.18 [16]. The photocathode is placed into a RF cavity. A pulsed laser beam is lighting the cathode in phase with the RF electric field in the cavity to optimize the acceleration of the extracted electron bunch. As an example, ~15 MeV relativistic electron beam with a charge per bunch up to 100 nC can be obtained directly after the RF gun at the AWA facility at Argonne National Laboratory [17]. The RF frequency ranges in 1–10 GHz. RF photoguns are used as injector for X-free laser facilities like X-FEL in Hamburg: the photodiode is directly inserted into a travelling wave cavity allowing for the pulsed electron beam operation up to 43 MeV, with a RF frequency of 12 GHz, a charge per bunch of 40 pC, a pulse duration of 530 fs and a repetition rate of 1 kHz [18]. It is worth mentioning that photoguns can produce polarized electron beams by injecting a circularly polarized laser light onto a GaAs photocathode [19]. A refined technique uses strained GaAs/GaAsP strained superlattice cathodes grown by gas-source molecular beam epitaxy. This technique allows to reach up to 86% spin polarization of the electron beam with a QE > 1% [20].

II.10.4 Source of antiparticles

A physics and societal interest exists for the production of beams of exotic particles. The main beams of interest are positrons, anti-protons and muons. These particles are not easy to produce and require special dedicated large instruments. In this section, a short summary to the positron sources physics and technology is proposed. The reader interested in anti-proton and muon beam production can find information in Ref. [21] and [22] respectively.

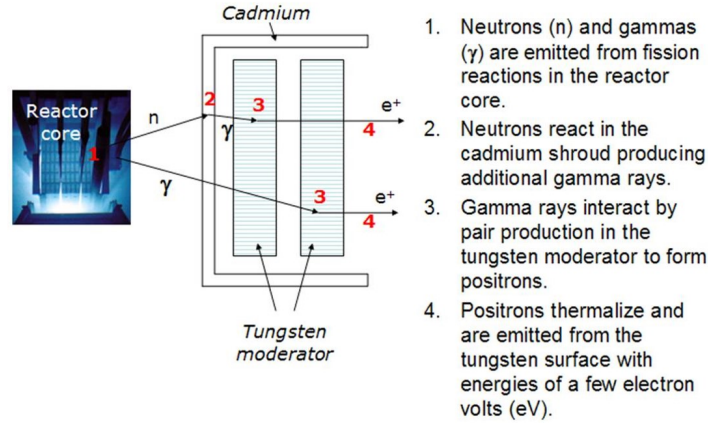


Fig. II.10.19: Sketch illustrating the positron beam formation from the PULSTAR nuclear reactor at the North Carolina State University [23].

Positrons can be produced by the two following reactions: the β^+ decay and the pair production. The β^+ decay is a weak nuclear reaction in which a neutron from an atom nucleus converts to a proton added with a positron e^+ for electric charge conservation and a neutrino ν_e . The nuclear reaction is written



where the initial atom with atomic number Z and mass number A converts to an element with atomic number $Z - 1$. Such nuclear reaction is common as many radioactive atoms can decay through this channel. The second channel of production of positrons is the pair production where an energetic photon, with a threshold kinetic energy $K \geq 2m_e c^2 = 1.22 \text{ MeV}$, impacts a particle X and generates a pair of electron and positron



The pair production effect is dominant for photons with an energy approximately larger than 10 MeV. At low energy, the dominant photon interaction channel is the photoelectric effect (up to $\sim 100 \text{ keV}$), and at intermediate energy, the Compton effect prevails. The higher the photon energy, the higher the pair production yield with respect to these two other photon interaction channels.

II.10.4.1 β^+ decay low-energy positron beam

At the North Carolina State University PULSTAR Reactor laboratory, an intense positron source has been developed to supply a high rate positron beam which is delivered to two experimental caves. Figure II.10.19 presents the principle of the positron beam creation [23]. Neutrons and γ are emitted from the fission reactor core. A part of the thermal neutron flux is converted into γ by radiative capture in a cadmium shroud [24]



The γ flux passes through a tungsten moderator assembly in which the pair production occurs. The tungsten is distributed into an array of strips whose geometry is optimized to allow the positron to thermalize

to an energy of ~ 3 eV before reaching the metal surface. Next, the positrons are extracted at 1 keV and focused by a set of electrostatic lenses, as can be seen on Fig. II.10.20, toward a beam transport line. The beam intensity reaches up to 10^9 e^+ /s when the reactors is set to its maximum 1 MW power. The positrons are mainly used to study material defects and porosity as positrons can penetrate into matter and form a positronium by binding with an electron. This neutral object is naturally accumulated into matter cavities. The final disintegration of the positronium into a photon pair is detected, which allows to reconstruct the location and the size of the cavity inside the sample of interest.

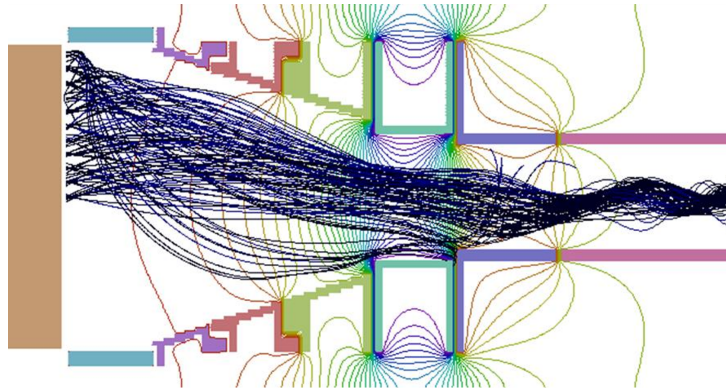


Fig. II.10.20: Simulation of the positron beam extraction and focusing toward the low-energy beam transport line at the Pulsar facility [23].

II.10.4.2 Intense positron beam by pair production

Another field of interest of positron beam is to use its low mass to design a high-energy/high-intensity $e^+ e^-$ collider. The compact linear collider project (CLIC), studied at CERN, is based on this idea [25]. The kinetic energy at the collision would reach three TeV. Three scenarios are considered to produce the required positron beam. The first possibility, illustrated on Fig. II.10.21, consists in impinging an intense 5 GeV electron beam, produced by a primary linac, on a pure tungsten crystal oriented along the $\langle 111 \rangle$ crystallographic axis. The high-energy electrons interact with the dense atoms of the material which produces an intense Bremsstrahlung emission of photons. The photons escape the thick target by channeling, i.e. by following the particular crystallographic direction of space inside the target where no atoms are present. Next, a dipole magnet is installed to filter out any charged-particle generated in the crystal. Finally, a second target made up with amorphous tungsten converts the γ flux into $e^+ e^-$ pairs. The conversion is followed by an adiabatic matching device, equipped with a magnetic field which will focus the positron beam into the first accelerating cavity of a 200 MeV linac. The second possibility to generate an intense positron beam (illustrated in Fig. II.10.22) is by directly generating γ photons inside a synchrotron radiation undulator, with a length of ~ 100 m. This technique avoids to use a tungsten crystal to produce the photons. The positron process creation after the undulator is similar to the former method. The third scenario to produce an intense positron beam is to create the necessary γ photons by the inverse Compton reaction. There, an high-energy electron beam collide with a laser beam. The elastic collision decelerates the electrons and the energy is transferred to the incident photon which can

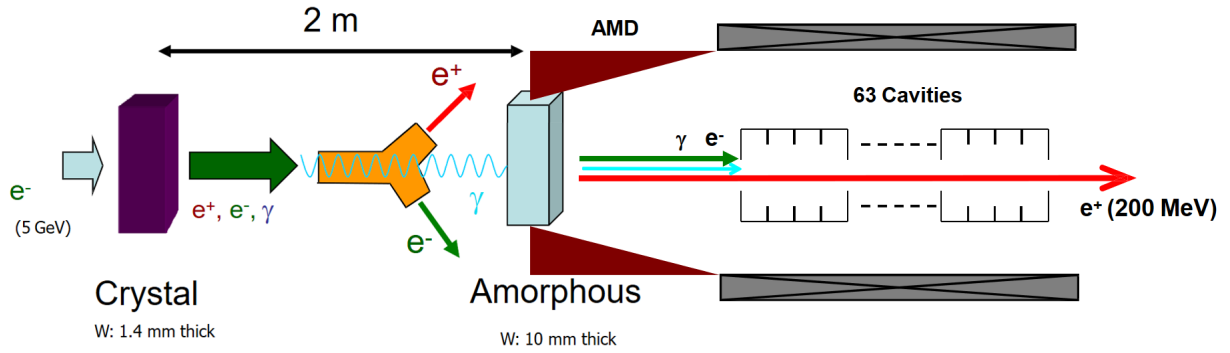


Fig. II.10.21: Sketch showing the process of generating a positron beam from a primary intense electron beam for the CLIC project. Adapted from A. Vivoli, CLIC Positron Source, POSIPOL 2009, Lyon.

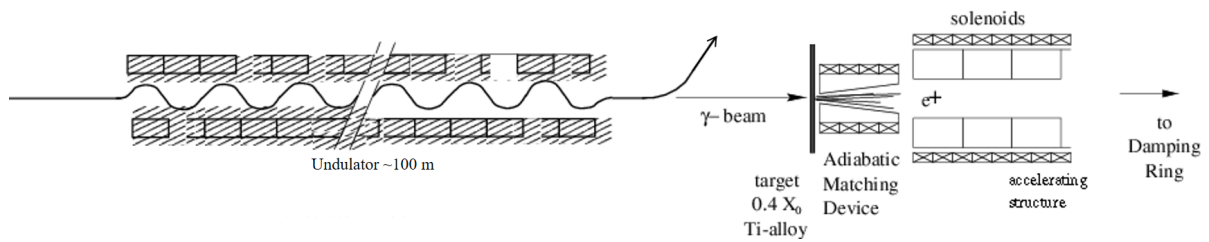


Fig. II.10.22: Sketch showing the process of generating a positron beam using a long synchrotron radiation undulator to generate the necessary γ photons. Second scenario of the CLIC project. Adapted from I. Bailey, Cockcroft Institute, Lancaster university, IWLC, 2010.

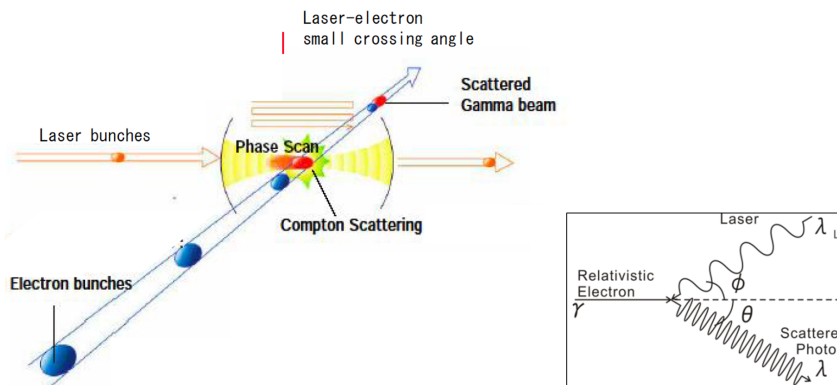


Fig. II.10.23: Sketch showing the process of generating γ photons using the inverse Compton effect. The next steps to generate a positron beam are then the same as the former techniques.

later trigger a pair production in an amorphous tungsten target, as discussed before. The reaction is illustrated in Fig. II.10.23.

II.10.5 Ion sources

Many methods exist to produce an ion beam. An overview of all the types of existing ion sources is proposed in Fig. II.10.24. Ion sources are specifically designed to produce either mono-charged negative

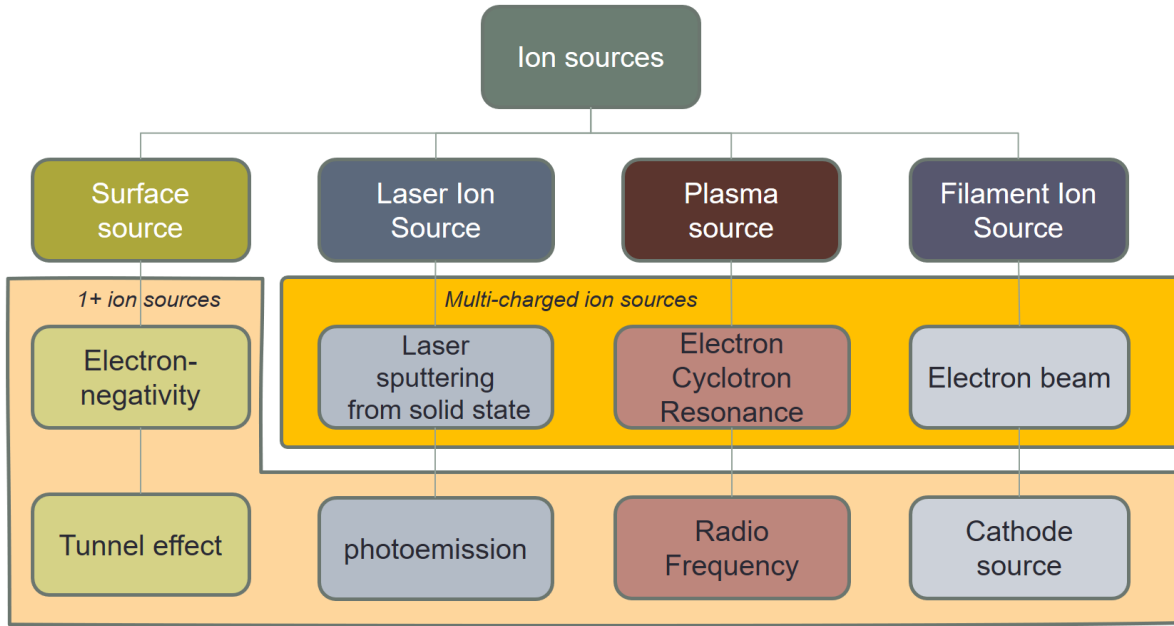


Fig. II.10.24: Overview of the different ion source families used in hadron accelerators.

or positive or multi-charged ion beams. The most common way to create positive ions is by ionising a low-pressure gas in a controlled volume, forming a plasma, and extracting a beam from it. Sustaining the plasma requires to bring a constant flux of energy toward the electron population to maintain the ionization state, while keeping the ion temperature as low as possible to minimise the transverse thermal ion beam emittance. The microscopic physics processes involved in the ion production in plasmas are presented in the next section. Other specific techniques to create ions are later presented: thermal surface ionization, laser ablation, and laser induced photo-ionization. The reader willing to dig further the topic can consult the Ref. [26, 27].

II.10.5.1 Thermal surface ionization

Atoms with a ionisation energy I adsorbed on a heated metal surface, with an electron work function W and a temperature T , can leave an electron to the metal when they are desorbed, resulting in a 1^+ ion ejection. The mechanism is modelled by the Saha-Langmuir equation [28]

$$\frac{n_+}{n_0} = \frac{g_+}{g_0} e^{\frac{W-I}{kT}}, \quad (\text{II.10.26})$$

where $\frac{n_+}{n_0}$ is the ratio of ion to neutral density population, $\frac{g_+}{g_0}$ is the ratio of ion to neutral partition functions. The electron is exchanged by tunnel effect. The surface ionization efficiency yield is given by the ratio

$$\frac{n_+}{n_+ + n_0} = \frac{1}{1 + \frac{g_0}{g_+} e^{-\frac{W-I}{kT}}}. \quad (\text{II.10.27})$$

The physics phenomenon is illustrated in Fig. II.10.25. The ionization process efficiency strongly depends on the respective values of W and I . Thermal ionization is optimal when $W - I > 0$, or at least

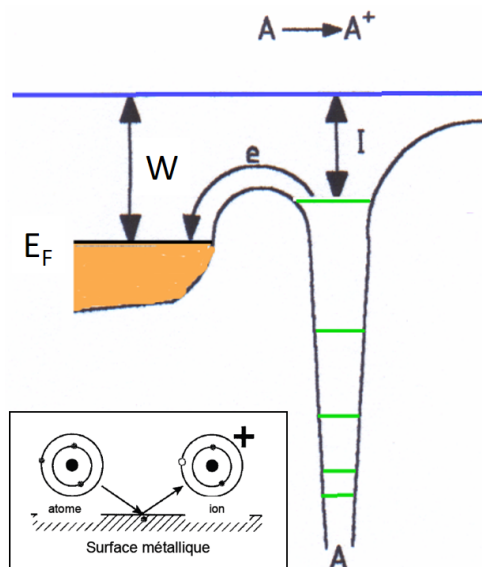


Fig. II.10.25: Electron energy levels of a material along with an adatom illustrating how an electron can be passed from the atom to the material. Encapsulation sketch: artistic illustration of the thermal surface reaction. Source: J. Arianer lecture (CNRS-IN2P3).

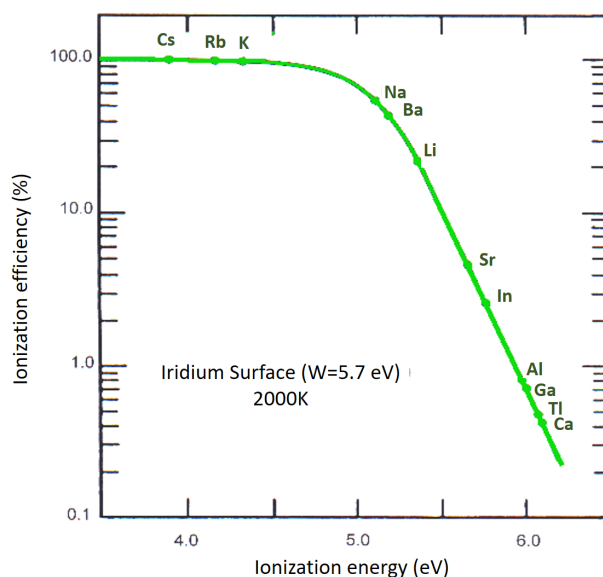


Fig. II.10.26: Surface ionization efficiency of various elements from an iridium surface heated at 2000 K, as a function of the element ionization potential. Adapted from J. Arianer lecture (CNRS-IN2P3).

when $W \sim I$. Raising the metal surface temperature allows to reach high-production yields, sometimes up to 100%. Thermal ionization works well with high work function metals having a high melting point temperature. Usual ionizers are made with W, Ir, C, Re, Pt. The easiest atoms to ionize are those with a low-ionization potential and a high-vapor pressure (i.e. with a low-evaporation temperature under vacuum). The method applies well to ionize alkali like K, Na, Cs and alkali-earth elements like Ba, Sr. It is also applicable to some metals and rare-earth like Al, Ga with lower efficiencies. Figure II.10.26 illustrates how the atoms thermal ionization efficiency evolves as a function of their ionization energy when placed on a 2000 K iridium surface.

II.10.5.2 Negative ion production

Atoms have the possibility to host an extra electron in their electron shell structure to form a negative ion. The associated extra electron binding energy is named electron affinity and labelled E_a later. Depending on the atom species, the attachment of the extra electron is either exothermic ($E_a > 0$), meaning that the negative ion must release energy to keep the new electron or endothermic ($E_a < 0$). The latter case corresponds for instance to the noble gases featuring closed orbital shells, or to the capture of a second extra electron for other atoms. E_a ranges from 0.02 (for Ca) to 3.6 eV (for Cl). Negative ions are stable but very fragile. Negative ions can be formed in volume (in plasmas) or on surfaces.

II.10.5.2.1 Volume production of negative ions

The volume production of negative ions is possible for gas species. The microscopic processes allowing for the negative ion productions are the dissociative attachment:



and the three body collision



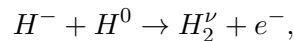
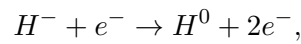
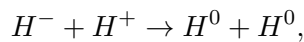
In both reactions, the excess energy is released through the kinetic energy carried away by the atom B . In the specific case of the H^- formation, the process requires two steps as follows: first, the H_2 molecule excitation to a high vibrational state ν by a fast electron



Second, the dissociative attachment of the excited H_2^ν molecule with a low-energy electron



The difficulties of volume H^- production are that it requires both two different electron energies for the two steps and that a subsequent collision of the fresh H^- with any other species can break the bound, with the main following reactions [29]



being respectively mutual neutralization, electron detachment and associative detachment.

II.10.5.2.2 Surface production of negative ions

The production of negative ions on surfaces is a physical effect similar to the one presented in Sec. II.10.5.1, except that now a material with a low work function passes an electron to an atom with a high ionization potential, adsorbed on its surface, by tunnel effect. The process is illustrated

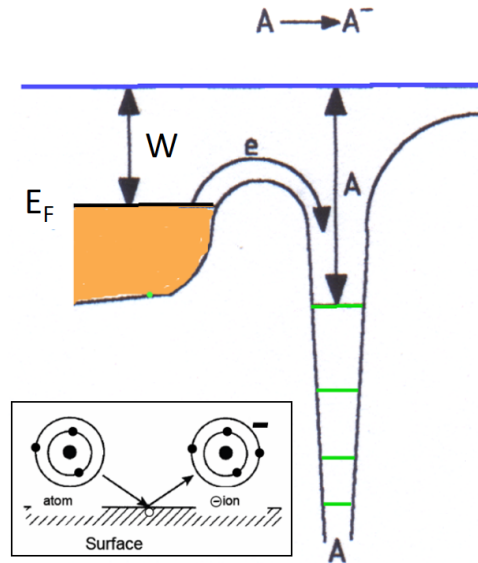


Fig. II.10.27: Electron energy levels of a material along with an adatom illustrating how an electron can pass from the material to the atom, forming a negative ion. Encapsulation sketch: artist illustration of the thermal surface reaction creating a negative ion. Source: J. Arianer lecture (CNRS-IN2P3).

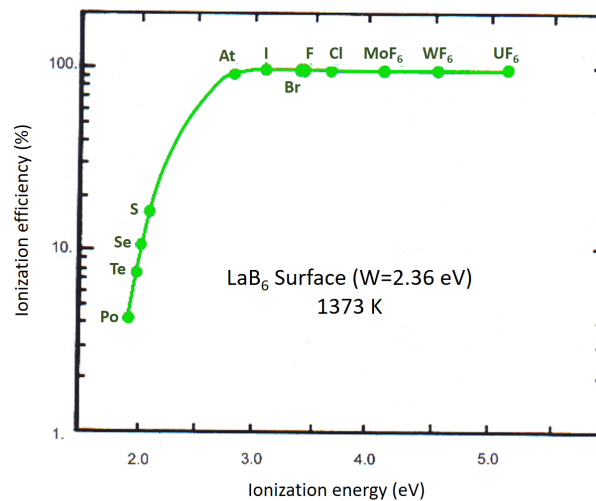


Fig. II.10.28: Surface negative ionization efficiency of various elements from a LaB_6 surface heated at 1373 K, as a function of the element ionization potential. Adapted for a course by J. Arianer (CNRS-IN2P3).

in Fig. II.10.27. Likewise, the increase of the surface temperature helps to desorb the negative ions. The negative surface ionization is also ruled by the Saha-Langmuir equation linking this time the density of neutral atom n_0 to the density of negative ions n_-

$$\frac{n_-}{n_0} = \frac{g_-}{g_0} e^{\frac{W-E_a}{kT}}, \quad (\text{II.10.32})$$

where $\frac{g_-}{g_0}$ is the ratio of the partition functions. A very efficient way to boost the negative ion production on surface is obtained by covering the hot metal surface with a low work function metal like Cs; this latter being easily vaporized at low temperature under vacuum. A common support metal used for this

purpose is Mo, whose work function is 4.6 eV. When it is covered with a full Cs atom mono-layer, the work function decreases to the Cs one (2.1 eV). In fact, the actual surface work function is even decreased down to 1.5 eV when the Cs monolayer coverage factor is partial between 0.5 and 0.7 [30].

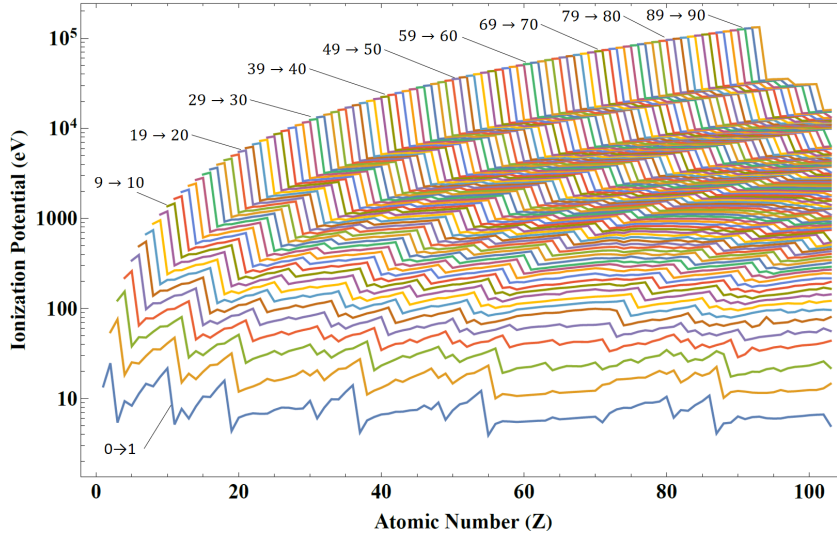


Fig. II.10.29: Electron ionization potentials (IP) as a function of the atomic number Z . The different lines correspond to successive IP required to pass from charge state $n \rightarrow n + 1$.

II.10.5.3 Positive ion production

Creating ions from atoms requires to remove bound electrons. The electron binding energies of the chemical elements are well tabulated [31, 32]. Figure II.10.29 presents the electron binding energy as a function of the atomic charge number Z . The lines correspond to the successive transition levels of ion charge state $n \rightarrow n + 1$. The first ionization potential of atoms varies from 3 to 24 eV, depending on Z , while deepest electrons from heavy ions are above 100 keV (e.g. 129.3 keV binding energy for the last uranium $1s^1$ shell electron). Because of the increasing number of protons, electrons occupying the same orbital are more tightly bound in heavier elements.

II.10.5.3.1 Electron impact ionization

The most efficient way to ionize an atom or ion is by the electron impact collision



where A is an atom/ion with charge state n and the incoming electron has a kinetic energy larger than the n^{th} electron binding energy of the electron removed to form a $(n + 1)$ charge state ion along with an added free low-energy electron. A semi-empirical model proposed by Lotz [33, 34] proposes a fair fit of the experimental electron impact cross sections for low and high charge state ions. For the simpler case

of ions charge state higher than 3+, the cross section model simplifies to

$$\sigma = \sum_{i=1}^N a q_i \frac{\log\left(\frac{E}{P_i}\right)}{E P_i} \text{ cm}^2, \quad (\text{II.10.34})$$

where the sum is done on the different subshells of the atom, E is the energy of the impinging electron in eV, P_i is the binding energy of the electron in the i^{th} subshell and q_i is the number of equivalent electrons in the i^{th} subshell. The constant $a = 4.5 \cdot 10^{-14} \text{ cm}^2 \text{ eV}^2$. Figure II.10.30 shows the evolution of the Lotz differential electron impact cross section as a function of the impinging electron energy for the Argon ions reactions $\text{Ar}^0 \rightarrow \text{Ar}^{1+}$, $\text{Ar}^{7+} \rightarrow \text{Ar}^{8+}$, $\text{Ar}^{11+} \rightarrow \text{Ar}^{12+}$, $\text{Ar}^{15+} \rightarrow \text{Ar}^{16+}$ and $\text{Ar}^{16+} \rightarrow \text{Ar}^{18+}$. Those transitions have been specifically selected as they illustrate how the cross sections peak intensity decreases with higher ions charge states belonging to deeper and deeper electron subshells, associated with higher and higher electron binding energy. Note also the respective increase of the cross section energy threshold. The higher the charge state, the smaller the ion size, the fewer the target electrons around the atom nucleus, and the lower the probability to remove a new electron.

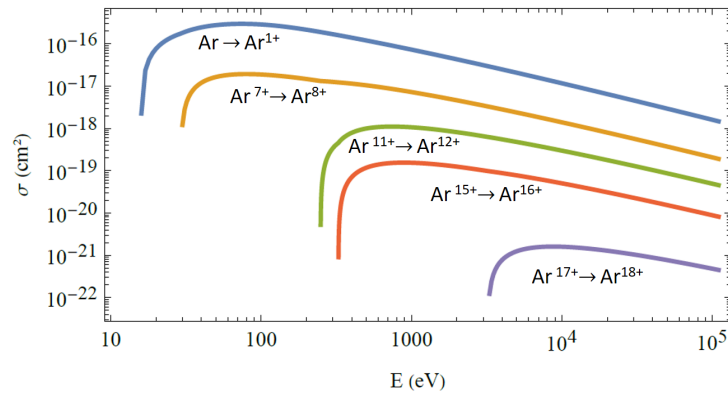


Fig. II.10.30: Electron impact ionization cross section for various argon ion targets. See text for details.

II.10.5.3.2 Charge exchange

The main atomic reaction destroying an ion, or reducing the ion charge state, is the charge exchange where an ion A^{n+} with charge state n crosses the path of a neutral atom B^0 resulting in a charge exchange of i electrons from atom A to ion B



A handy fit formula proposed by Müller and Salzborn [35] for the charge exchange cross section from charge state n to $n - i$ is

$$\sigma_{n \rightarrow n-i} = A_i n^{\alpha_i} (P_0 [\text{eV}])^{\beta_i} \text{ cm}^2, \quad (\text{II.10.36})$$

where P_0 is the first ionization potential of atom B , n is the initial ion charge state and $i = 1, 2, 3, 4$ is the number of exchanged electrons. The tabulated fit values are reported in Tab. II.10.4 for convenience. Figure II.10.31 plots the evolution of the charge exchange cross section between an argon atom and an

initial argon ion of charge state n , for the cases $i = 1, 2$. One can note that the cross section ranges within $10^{-13} - 10^{-14} \text{ cm}^2$, which is two decades higher than the electron ionization cross section in Fig. II.10.30. One can deduce that the steady production of high charge state ions in a plasma requires a neutral density as low as possible to avoid the rapid destruction of the ions.

Table II.10.4: Müller and Salzborn [35] fit parameters for the charge exchange as a function of the number i of electrons exchanged.

i	A_i	α_i	β_i
1	$(1.43 \pm 0.76) \times 10^{-12}$	1.17 ± 0.09	-2.76 ± 0.19
2	$(1.08 \pm 0.95) \times 10^{-12}$	0.71 ± 0.14	-2.80 ± 0.32
3	$(5.50 \pm 5.8) \times 10^{-14}$	2.10 ± 0.24	-2.89 ± 0.39
4	$(3.37 \pm 8.9) \times 10^{-16}$	4.20 ± 0.79	-3.03 ± 0.86

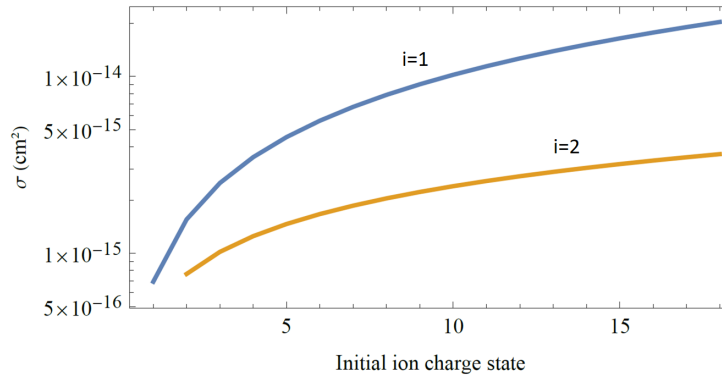


Fig. II.10.31: Evolution of $i=1$ and $i=2$ charge exchange cross section of neutral argon with Ar^{n+} ion as a function of the initial charge state n .

II.10.5.3.3 Photo-ionization

Another way to ionise atoms and ions is by photo-ionization. There, a UV to XUV laser is used to ionize the neutral atom following the reaction



Measured photo-ionization cross sections show values in the range $\sigma \sim 1 - 50 \cdot 10^{-18} \text{ cm}^2$, which is approximately a factor 100 times lower than the equivalent electron impact ionization cross section [36]. This is why ionizing atoms is preferably done with electrons rather than photons. The production of high charge state ions is even more difficult as it requires high-energy photons with still very low cross sections values. Nevertheless, despite its overall low efficiency, an interesting application of photo-ionization is the resonant laser ion source presented later in this chapter.

II.10.5.3.4 Radiative recombination

Radiative recombination (RR) is the process when an ion collides with a low-energy electron resulting in the electron capture and the reduction of the ion charge state



The process is followed by a photon emission (represented by the term $h\nu$ in the above equation) bringing the freshly trapped electron to its final stable binding energy state. A semi-classical formula proposed by Kramers [37,38] gives the RR cross section summed over the orbital quantum number l for hydrogen-like ion configurations with nucleus charge number Z

$$\sigma_{RR} = 2.10 \times 10^{-22} \frac{Z^4 R_y^2}{nE(Z^2 R_y + n^2 E)} \text{ cm}^2, \quad (\text{II.10.39})$$

where R_y is the Rydberg energy constant, E is the incoming electron kinetic energy and n the principal quantum number. A practical extension of the formula to multi-charged ions with a charge state number Q and a nuclear charge number Z can be estimated following the simple expression proposed by Hahn & Rule [39] by substituting the charge number Z in Eq. II.10.39 by an effective charge Z_{eff} defined as

$$Z_{eff} = \begin{cases} \frac{1}{2}(Z + Q) \quad \forall Q \geq \frac{Z}{2} \\ \sqrt{ZQ} \quad \forall Q \leq \frac{Z}{2} \end{cases}. \quad (\text{II.10.40})$$

In typical ion source plasmas, the RR cross section to remove a charge from an ion is several orders of magnitude lower than the charge exchange process. This process is thus neglected in ion source models. For completion, one must cite the dielectronic recombination process, a more complicated collision where a free electron is attached to the ion, like for the RR, but with the concomitant excitation of a bound electron leading to a doubly excited state [40]. Next, either the system decays to the ground state and the ion finally loses an electron, like for the RR, or the system is unstable and one of the electrons is kicked out of the ion, leaving the charge state unchanged.

II.10.5.4 Particle confinement

While the mean free path occurrence of an electron impact collision to produce a 1^+ ion is of the order of 0.1 m in a plasma source, this distance can extend up to several km to produce a very high charge state ion. Because ion sources are compact with a size ranging from 0.05 to 1 m, it is necessary to find ways to keep electrons and ions long enough to allow the production of multi-charged ions. The two classical ways to confine charged particles are magnetically and electrostatically.

II.10.5.4.1 Magnetic confinement

When charged particles propagate in a magnetic field, their velocity is advantageously decomposed into directions respectively perpendicular and parallel to the local magnetic field vector: $\vec{v} = \vec{v}_\perp + \vec{v}_\parallel$ (i.e. \vec{B} and \vec{v}_\parallel are colinear). While the parallel motion is unaffected by the magnetic field, the perpendicular

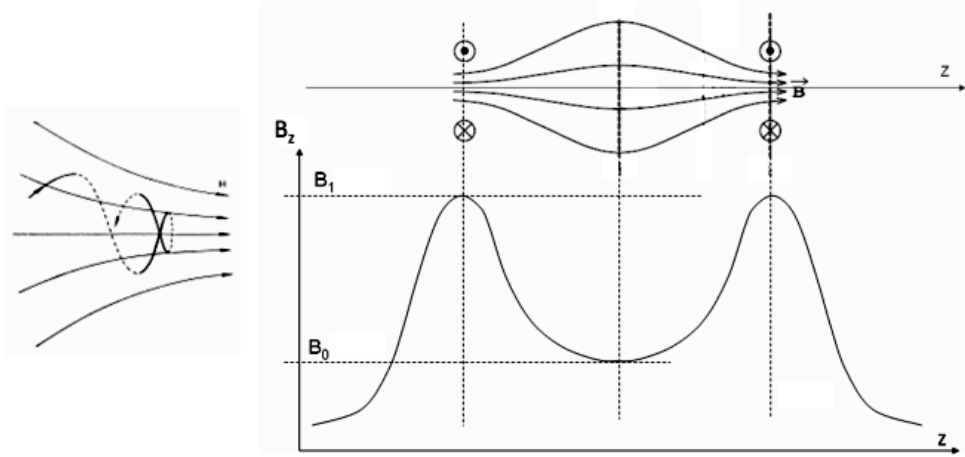


Fig. II.10.32: Top: axial magnetic mirror composed of a set of two axial coils. Bottom: magnetic field profile along the coil axis z . At the coils center the magnetic field intensity is maximum with $B = B_1$ while it passes by a minimum in between at $B = B_0 < B_1$. See text for details.

trajectory becomes a circle or radius ρ such that $v_{\perp} = \rho\omega$ and

$$\omega = \frac{qB}{m}, \quad (\text{II.10.41})$$

where ω , q and m are the angular cyclotron frequency, the particle charge and mass respectively. The particle kinetic energy K is a constant of motion

$$K = K_{\perp} + K_{\parallel} = \frac{1}{2}mv_{\perp}^2 + \frac{1}{2}mv_{\parallel}^2 = \text{const.} \quad (\text{II.10.42})$$

If the magnetic field is varying sufficiently slowly in space and time (i.e. when $\frac{1}{B} \frac{\partial B}{\partial t} \ll 1$ and $\frac{\rho \nabla B}{B} \ll 1$), the particle magnetic moment is an adiabatic invariant of motion

$$\mu = \frac{K_{\perp}}{B} = \text{const.} \quad (\text{II.10.43})$$

Combining Eq. II.10.42 and II.10.43 gives

$$K = K_{\parallel} + \mu B. \quad (\text{II.10.44})$$

In a static magnetic field built on purpose to include a magnetic mirror, like presented in Fig. II.10.32, a charged particle created at a place where B is minimum ($B = B_0$) can be reflected back while propagating toward the coil magnetic field maximum B_1 . This is the magnetic mirror effect, which can be demonstrated as follows. Between the coils, the particle kinetic energy is: $K = K_{\parallel 0} + \mu B_0$. When the particle propagates toward the coils, B increases ($B > B_0$) and consequently, considering the local equality $K = K_{\parallel} + \mu B$, one can deduce that $K_{\parallel} < K_{\parallel 0}$: the velocity component parallel to B decreases. If $\mu B_1 \geq K$, there exist a place along the z axis, before the coil peak field, where $K_{\parallel} \rightarrow 0$. There, the particle velocity is purely perpendicular to the magnetic field. The particle is forced to move backward. Defining the magnetic pitch angle as $\theta = (\vec{B}, \vec{v})$, the initial angular condition to grant a magnetic mirror

reflection can be written as

$$\sin \theta \geq \frac{1}{\sqrt{R}}, \quad (\text{II.10.45})$$

where $R = \frac{B_1}{B_0}$ is the mirror ratio. One can note that the magnetic mirror effect does not depend on the velocity but rather on the local ratio of v_{\parallel} to v_{\perp} . The phase space area where particles are confined is illustrated in Fig. II.10.33. The phase space area associated with a non-confinement of a particle is named the loss cone. The radial magnetic confinement of particle can be efficiently achieved with a multi-pole

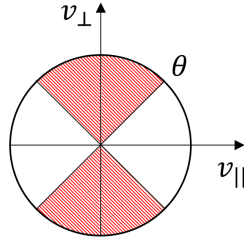


Fig. II.10.33: Particle velocity phase space in a magnetic field. Particles following inequality Eq. II.10.45 are indicated in dashed area.

magnetic field like quadrupole, sextupole, octupole, etc. An ideal multipole with order n generates a transverse magnetic field with the following expression

$$\begin{cases} B_x = B_0 \left(\frac{r}{R_0}\right)^{n-1} \cos(n-1)\theta, \\ B_y = -B_0 \left(\frac{r}{R_0}\right)^{n-1} \sin(n-1)\theta, \\ B_z = 0, \end{cases} \quad (\text{II.10.46})$$

where R_0 is the free multiple radius and B_0 is the multipole intensity at $r = R_0$. By symmetry, the field in the center is null while its intensity increases gradually as the radius increases. The radial multipole magnetic confinement is illustrated in Fig. II.10.34 where half a dodecapole is represented along with a sample of particle trajectories [41]. One can see how particles propagating toward the poles are focused and finally magnetically mirrored back toward smaller radius where the magnetic field intensity is weaker. A drawback of multipole magnetic confinement for plasma is that the particles loss to the wall are concentrated on small surfaces, leading to possible local wall degradation due to sputtering of local wall temperature heating.

II.10.5.4.2 Electrostatic confinement

It is possible to confine a particle species, either positive or negative by creating an electrostatic potential well. An axial electrostatic trap is composed of a set of colinear metallic cylinders biased to specific voltages as illustrated in Fig. II.10.35 where a central hollow electrode set to ground potential is cornered by a positive electrode on the left and on the right. The electric field profile on axis is plotted in red, with a minimum V_0 at the center surrounded by two peak intensities V_1 . If a particle with a kinetic energy K and an electric charge q is present in the trap, it won't be able to escape axially provided that $K < q(V_1 - V_0)$. The radial electrostatic confinement is more difficult to achieve experimentally. For

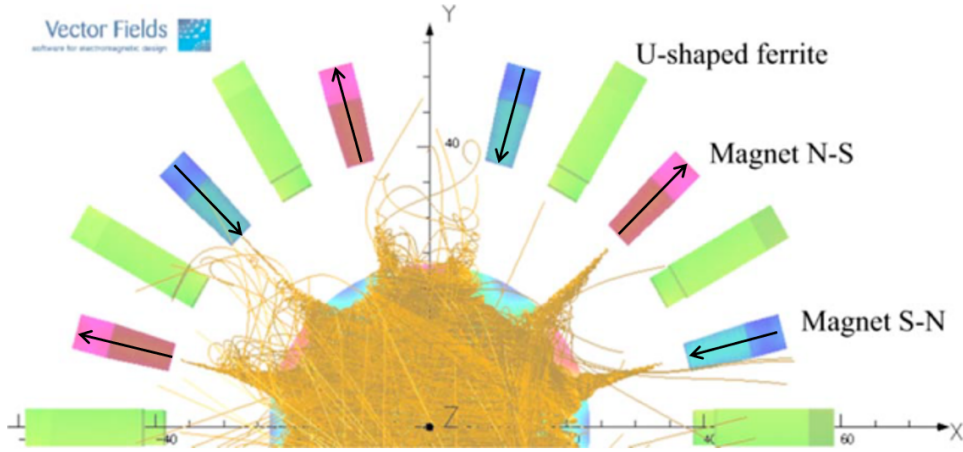


Fig. II.10.34: Simulation result showing how particles are confined by a radial multicusp magnetic field. Reproduced from J. Lettry et al., *Rev. Sci. Instrum.*, 81 (2): 02A723, with the permission of AIP Publishing.

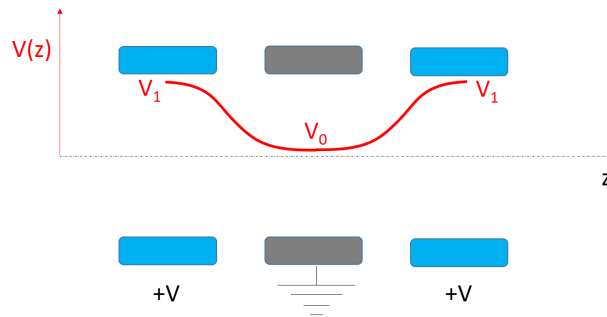


Fig. II.10.35: Set of three concentric biased electrodes forming an axial electrostatic trap for ions.

instance, in an electron beam ion source (see later Sec. II.10.5.10.2), a radial electrostatic confinement $\vec{E} = E_r(r) \cdot \vec{r}$ is achieved by the local space charge generated by the constant flow of an electron beam that can trap ions (see Fig. II.10.36)

$$E_r(r) = \begin{cases} \frac{\rho r}{2\epsilon_0} & \forall r \leq r_0 \\ \frac{\rho r_0^2}{2\epsilon_0 r} & \forall r > r_0 \end{cases}, \quad (\text{II.10.47})$$

where ρ is the local ion beam charge density per unit volume and r_0 is the electron beam radius. The peak electric potential carried by the beam is $V(r_0) = \frac{\rho r_0^2}{4\epsilon_0}$. One should note that when the electron beam is loaded by ions, the total charge density decreases. A limit of ion accumulation is reached when the electron beam is fully space charge compensated by the trapped ions charges.

II.10.5.4.3 Ion production dynamics

When the ions are created in a volume, it is interesting to model the dynamics of ion production using a simple linear zero dimension model (assuming that the process is homogeneously distributed in space).

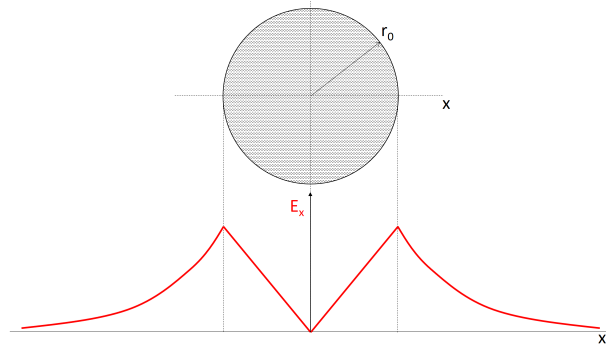


Fig. II.10.36: Electric field generated by a charged-particle beam with radius r_0 as a function of the radius.

The dynamics of an ion species density n_i with charge state i and velocity v_i can be written as [42]

$$\frac{\partial n_i}{\partial t} = n_e n_{i-1} \langle \sigma_{i-1 \rightarrow i}^{ei} v_e \rangle + n_0 n_{i+1} \langle \sigma_{i+1 \rightarrow i}^{ce} v_{i+1} \rangle - n_0 n_i \langle \sigma_{i \rightarrow i-1}^{ce} v_i \rangle - n_e n_j \langle \sigma_{i \rightarrow i+1}^{ei} v_e \rangle - \frac{n_i}{\tau_i}. \quad (\text{II.10.48})$$

While the equation for evolution of the neutral gas density n_0 is

$$\frac{\partial n_0}{\partial t} = \Phi_0 - \sum_{i=1}^{i=Z} n_0 n_i \sigma_{i \rightarrow i-1}^{ce}, \quad (\text{II.10.49})$$

where σ^{ei} and σ^{ce} are electron impact and charge exchange cross sections, v_e is the electron velocity, Φ_0 is the neutral incoming flux. The electron collision rates are calculated with an imposed normalized electron velocity function distribution f as $\langle \sigma v \rangle = \int_0^\infty f(v) dv$. And the term $-\frac{n_i}{\tau_i}$ models the confinement time which depends on the geometry and possible magnetic or electrostatic confinement system. In this simple model, the charge exchange and electron impact are assumed to exchange only one electron per collision. The radiative recombination and photoionizations are also neglected.

II.10.5.5 Surface ionization ion source

This type of ion source uses the thermal ionization physics process (see Sec. II.10.5.1) [43]. The sketch of a typical surface ionization ion source is presented in Fig. II.10.37. A piece of metal of interest is inserted into a reservoir surrounded by a heating system, constituting a metallic oven. When the oven temperature is high enough, the metal evaporates and pressure builds up. The evaporated atoms are then diffusing toward the ionizer stage made up with a porous material. The ionizer is heated by an independent system, to reach a temperature higher than the oven one, to maximise the surface ionization efficiency. The source is set to a positive high voltage. The porous ionizer is facing a set of extraction electrode to accelerate the 1^+ ion beam toward the ground. The advantages of a porous ionizer are (i) an increase of the overall ionization efficiency (by an subsequent increase of the emissive ion surface) and (ii) the possibility to shape freely the porous ionizer geometry to adapt the electric field in the extraction area, like for a solid thermionic electron gun. The intensities achievable with usual surface ionization is ranging in 0.1-100 μA . For further details on surface ionization ion sources, see for instance [44]. An advantage of surface ion sources is that they are highly selective. They are used in radioactive ion beam

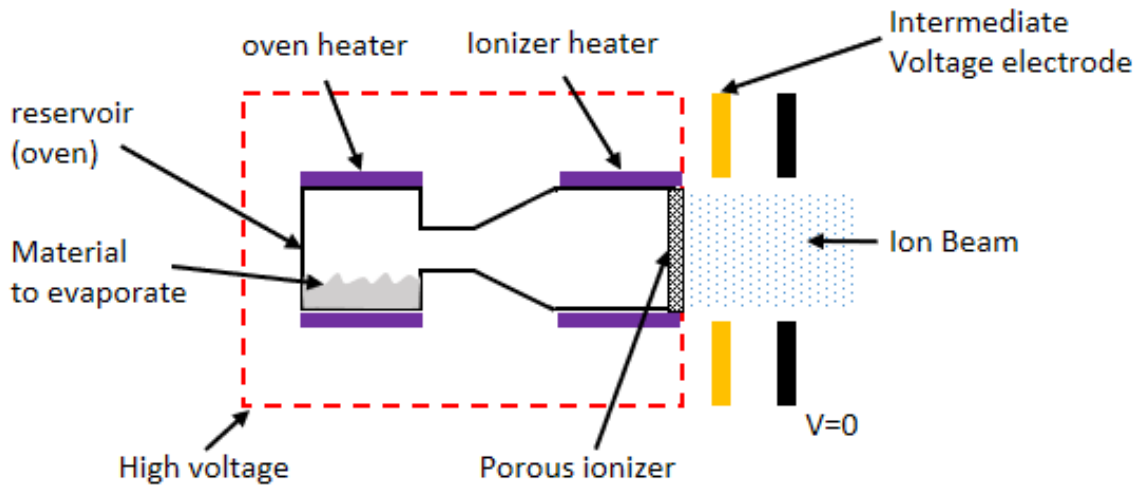


Fig. II.10.37: Block diagram of a typical surface ionization ion source.

facilities to produce radioactive alkali ion beams from targets [45].

II.10.5.6 Filament ion source

Filament ion sources are widely used in the industry because they are very simple to build and maintain. In a filament ion source, an electron beam is produced by a thermionic gun which ionizes a gas injected into a plasma cavity set under vacuum. In this part, three different types of monocharged filament ion sources are presented: the indirectly heated cathode (IHC) ion source used in the industry, the pressure ion gauge source (PIG) used on cyclotrons and the forced electron beam arc discharge (FEBIAD) used in target ion sources system to produce radioactive ion beams.

II.10.5.6.1 Indirectly heated cathode (IHC) ion source

Indirectly heated cathode ion sources (IHC) are included in modern industrial ion implanters to produce very intense beams to dope semi-conductors. CW intensities up to 30 mA of B^+ , F^+ , H^+ , Ge^+ etc, are daily produced with such ion sources. Figure II.10.38 presents the typical layout of an IHC ion source as presented into a patent [46]. The ion source consists first of a rectangular cavity set to a high voltage: the anode. The gas to ionize is injected by a controlled valve into the cavity. The cavity is crossed by a magnetic field, generated by an external dipole magnetic field, aligned with the cavity main axis. On the left (see the zoomed area), a massive cathode is indirectly heated by a smaller heated filament located behind the massive cathode. The massive cathode is set to a potential lower than the anode (-100 to -200 V) which accelerates thermionic electrons toward the cavity. The electrons are guided by the magnetic field through the chamber and are reflected back at the other end (right side on the drawing) by an anti-cathode set to the same potential as the massive cathode. The gas is ionized on flight by electron impact. The source operates in the range $\sim 10^{-3}$ Pa and has an atom to ion conversion efficiency of the order of a few %. The ions are collisional at this pressure and drift toward the slit extraction aperture where they are accelerated by a set of dedicated electrodes (not represented

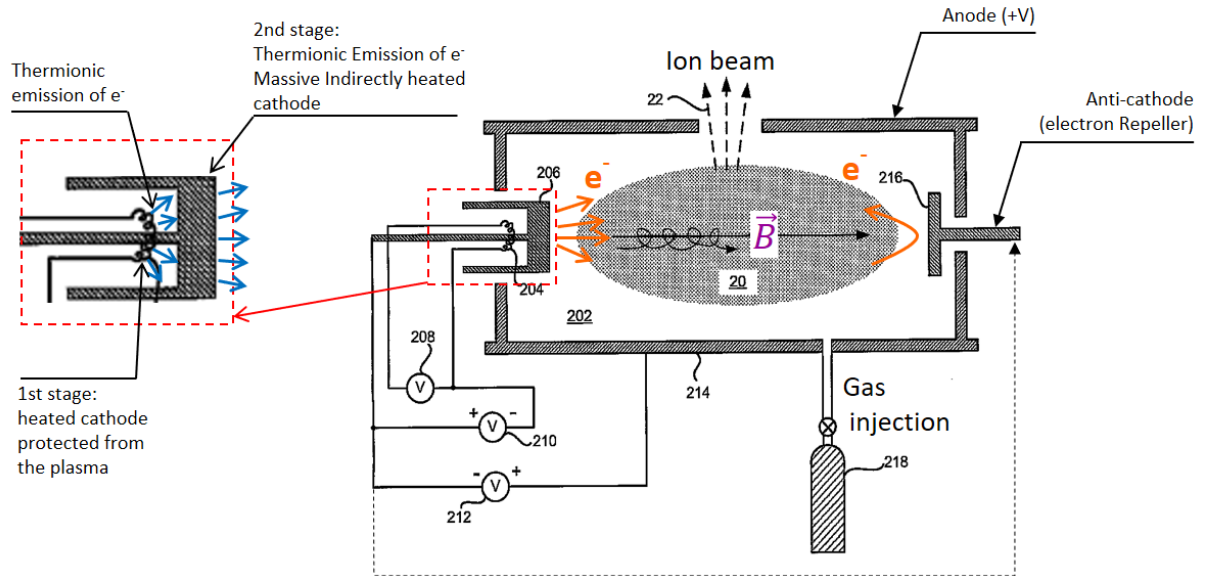


Fig. II.10.38: Sketch of an IHC ion source [46]. See text for details.

in the figure). The main advantage of this technique is that the first stage filament is protected from the arc discharge plasma and does not suffer from direct high-intensity ion bombardment. The massive cathode and anti-cathodes, facing the plasma, are sputtered instead. And, because they are massive, they can withstand long operation without maintenance, up to 1000 to 2000 hours, to be compared with the former generation of Freeman or Bernas ion sources (see Fig. II.10.39(b) showing a Bernas ion source whose filament is directly in contact with the arc discharge, resulting in a cathode lifetime roughly an order of magnitude lower with identical condition of beam production).

II.10.5.6.2 Penning ionization gauge (PIG) ion source

The Penning ionization gauge ion source is an old filament source concept able to produce single and up to medium charge state ions. It still used today on a few pulsed accelerators like GSI [47] and more specifically as an internal source for cyclotrons. A typical layout of a PIG source installed at the center of a cyclotron is presented in Fig. II.10.40 left. The source consists of a thin tube in which the electron beam is confined by the strong central cyclotron magnetic field. The ion source behavior is similar to the IHC. The specificity here is that the extracted beam is accelerated in the cyclotron magnetic field and that the beam turns around the ion source (see Fig. II.10.40 right). Recently, the lifetime of the filament in cyclotron PIG was enhanced by fabricating the cathode with a metal strip plate providing extra mechanics strength to counter the Lorentz force due to the passage of current perpendicular to the cyclotron magnetic field axis [48].

II.10.5.6.3 Forced electron beam arc discharge source (FEBIAD)

Several research facilities in the world are dedicated to the study of exotic nuclei (with short radioactive lifetime) like ISOLDE [49] at CERN. Radioactive nuclei are created in a dedicated target not discussed. The target is heated to facilitate the effusion of condensable radioactive chemical elements toward a

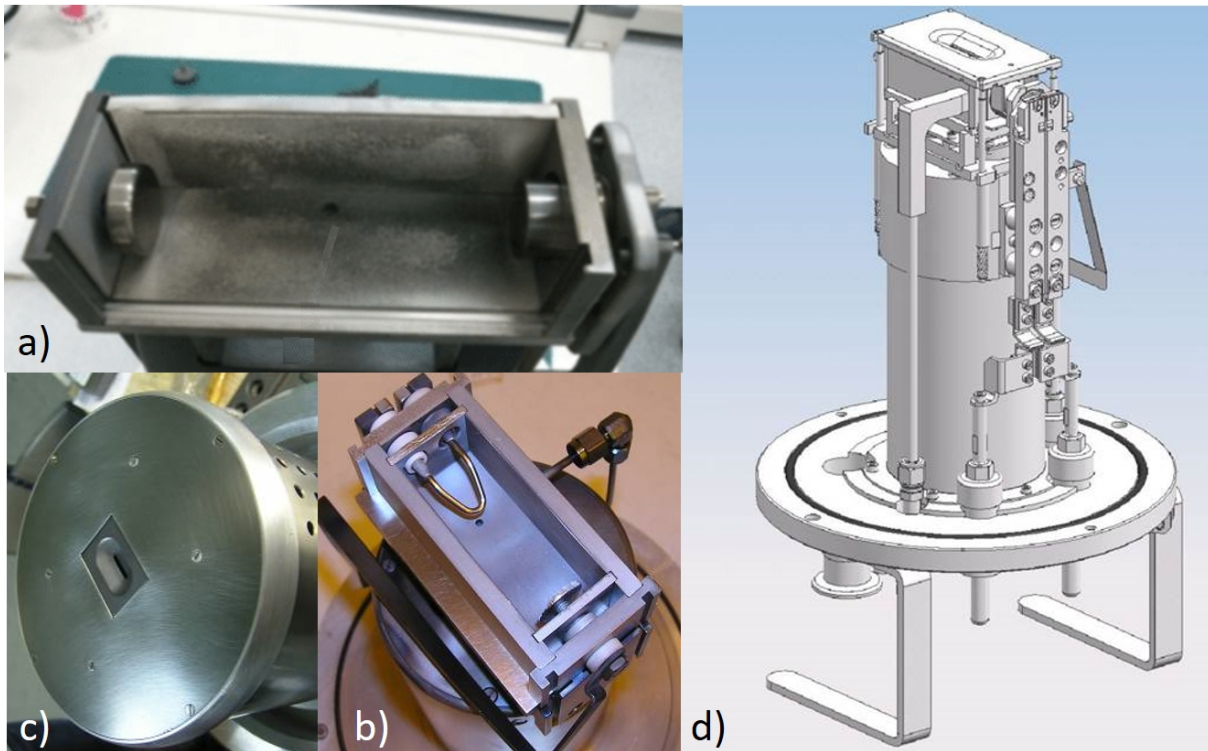


Fig. II.10.39: a) View of a dismantled industrial IHC ion source. The cathode and anti-cathode are visible at each discharge chamber end. b) Former technology Bernas ion source where the filament is directly in contact with the plasma. An anti-cathode is located at the other end of the arc chamber. c) Photograph of a typical slit extraction of an implanter filament ion source. d) Design view of a socket system holding the whole filament ion source mechanics, allowing fast plug/unplug maintenance to maximize the operation time.

specific hot ion source where the atoms are ionized once then accelerated toward an radioactive ion beam (RIB) accelerator for further study. Because of a huge local radioactivity and a high temperature, the lifetime of sophisticated ion sources in RIB facilities is very short, of the order of a few weeks. The requirement for the ion source is that it should be robust, simple, cheap and able to operate for a few weeks run. The forced electron beam ion source arc discharge (FEBIAD) is specifically designed for this purpose [50]. Figure II.10.41(a) proposes an overview of the CERN FEBIAD MK7 target ion source which operates up to 500°C, while Fig. II.10.41(b) shows a zoom of the FEBIAD. An external coil provides an axial magnetic field that guides charged particles in the cylindrical ion source. On the right is located a massive hot Ta cathode which emits electrons toward the arc chamber (the anode) through a grid that allows a fine tuning of the electric field controlling the electrons energy and their spatial distribution. The hot radioactive gaseous atoms emitted by the target are diffusing toward the source by a hot transfer line and injected through the grid into the arc chamber. The ions are produced by electron impact and are guided by the magnetic field toward the extraction system. The ionization efficiency of this device is in the range 20 to 70%. It can produce beam intensities of 1^+ ions of the order of $1 \mu\text{A}$. Other versions of FEBIAD exist for higher working temperature operation up to 1900°C. With these versions, evaporated condensable radioactive elements (e.g. Au, Bi, Pb, Pd, Ge, etc) can be ionized and transformed into an ion beam.

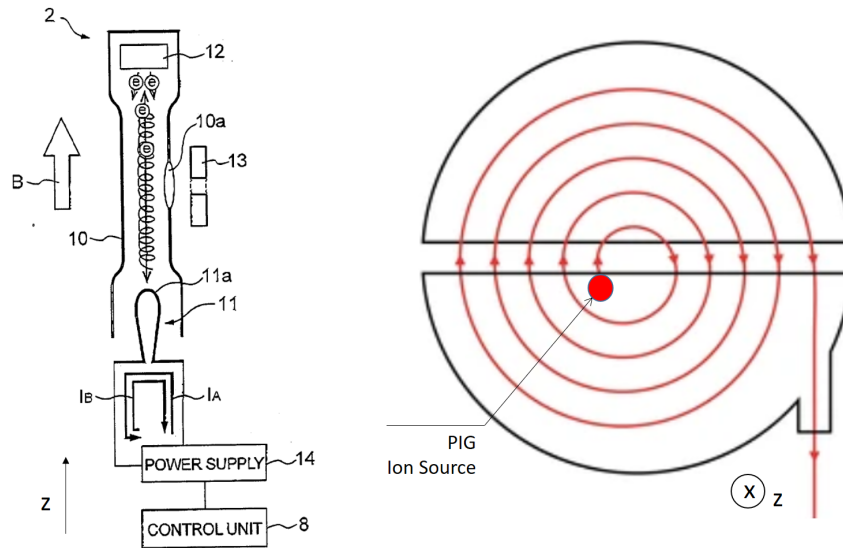


Fig. II.10.40: (Left) Layout of a PIG ion source for cyclotron extracted from the patent EP13020087NWA1 [48]. (Right) Top view of a cyclotron showing how the ion beam turns around the PIG source.

II.10.5.7 Resonant ionization laser ion source

Resonant ionization laser ion sources (RILIS) use photoionization to ionize atoms. As a single laser with a photon energy higher than the first atom ionization potential would ionize many unwanted chemical species, a step-wise resonant excitation of the atom by a combination of several laser wavelengths is used to ionize a specific atomic species. In RILIS, up to three different laser wavelengths are fine tuned to populate successive electron excited levels until the atom reaches either an auto ionization state or a Rydberg level. A detailed review of RILIS is available in the open publication by Fedosseev [51] and used below to explain the RILIS physics. Figure II.10.42 presents an overview of the possible step-wise photon excitation of the electron energy levels leading to an atom ionization in RILIS. Three main electron excitation pathways are used to eventually expel an electron, depending on the atom ionization potential level (referred to as E_i on the plot). The first common step is to promote a valence electron to a high-lying energy level. This step is done with one or several laser pulses, depending on the atom configuration. The blue arrows in Fig. II.10.42 indicate transition requiring the generation of higher harmonics of laser radiation (with energy $\hbar\omega_L$): $2\omega_L$, $3\omega_L$ or $4\omega_L$. Next, three paths are possible. The first possibility is a non-resonant transition to the continuum (see green arrow paths to A, D, I, L in Fig. II.10.42), but the low ionization efficiency of the transition requires high energy laser and the final ion production yield is limited by the laser available power. The second step is through the autoionization state mechanism (labelled *ais* in Fig. II.10.42, see transitions B, E, H, J, M) where several laser pulses raise the energy level of two or more electrons so that their total energy excitation is larger than the ionization limits: the consequent electron energy re-arrangement leads to the emission of a free electron. When it is available, it is advantageous to use *ais* mechanism as the associated cross sections are 2–3 orders of magnitude higher than the autoionization transition ones. Finally, when *ais* is unpracticable, the last path is to populate Rydberg states where the highly excited electron state is a few meV away from the ionization

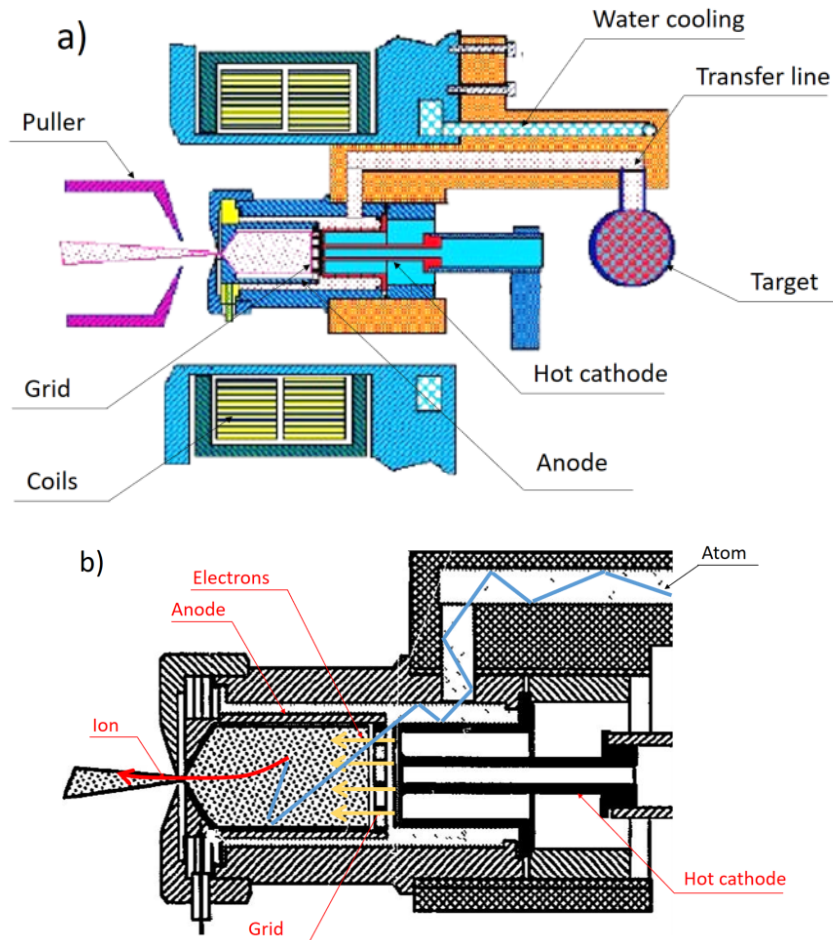


Fig. II.10.41: a) Overview of the CERN FEBIAD ion source MK7. b) Zoom around the source plasma chamber.

level (transitions C, F, K, N). The extra missing energy to free the electron is brought for instance by an externally applied electric field or a collision with another atom. RILIS are used in target ion sources assemblies in RIB facilities (see also discussion in Sec. II.10.5.6.3). Figure II.10.43 proposes a cut-away view of the CERN RILIS target ion source. The ionization is achieved in a 3 mm diameter and 34 mm length tube heated up to 2000°C. The laser beams are injected through the ion source extraction electrode hole. The resistive heating of the tube provides a small electric field which helps the ion extraction from the source. RILIS used as a target ion source offers several advantages: i) the source mechanics is simple and robust, while the complexity, coming from the tuning and maintenance of lasers is external and is done in a safe place without radioactivity, ii) the ionization of atoms is specific to a given chemical species, which means that the source extracts only isotopic ions with the same nucleus charge number Z and excludes any unwanted isobars. Hence, the later beam selection with a bending magnet (selecting according to $\frac{A}{q}$, $q=1^+$) allows to filter any unwanted atomic mass A and provides highly pure RIB species for which physics experiments can be achieved even with very small intensities of ions.

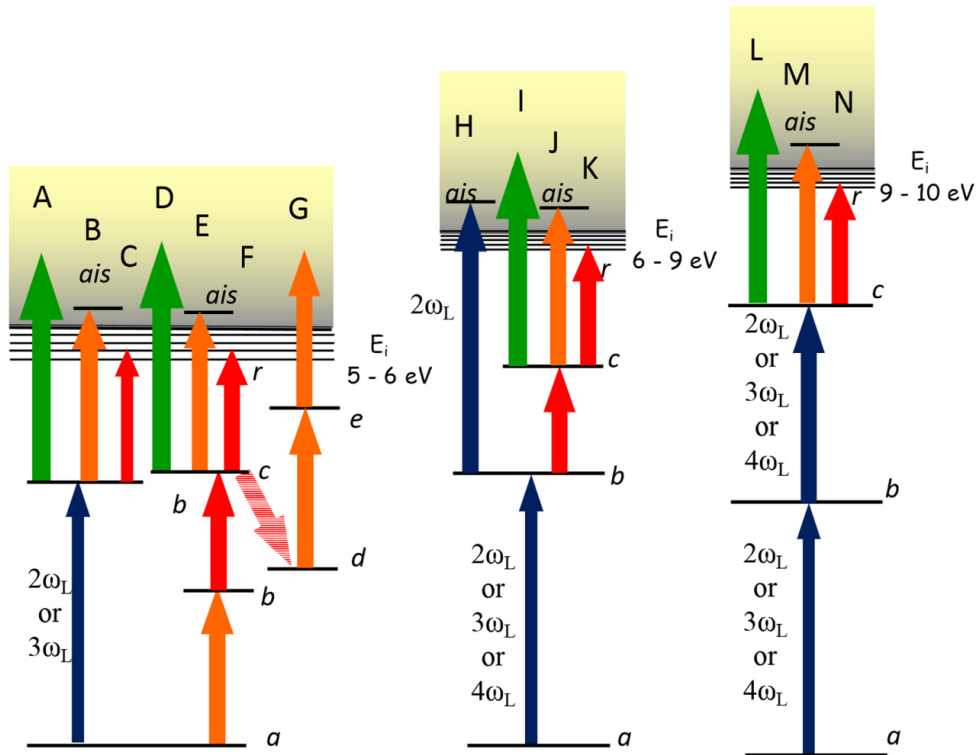


Fig. II.10.42: Resonance ionization pathways used by the ISOLDE RILIS. See text for details. Reproduced from [51] under CC 3.0 licence.

II.10.5.8 Negative ion sources

Negative ion sources are used in accelerators when it is found advantageous. Indeed, it is very easy to convert a negative ion beam into a positive one by passing it through a simple stripping foil. The instant change of particle beam sign can be an excellent advantage for a variety of accelerators as it tricks with the Liouville theorem. One can cite for instance the stripping of negative ion beam in the core of a tandem electrostatic accelerator, allowing to finally double the beam energy once outside of the tandem. Or the enhancement of the delicate proton beam extraction from a cyclotron using a H^- stripper. And also the simplification of injecting protons into a storage ring, replacing the extreme ramping requirements on injection kickers by an elegant charge exchange device. And last but not least, negative H^- ion sources allow for the injection of neutrals into tokamaks to provide ohmic heating of the fusion plasma. In this section, three negative ion sources will be briefly presented: the magnetron driven surface ion source, the RF driven negative ion source, and the neutral injectors of the ITER tokamak. Reader willing to learn further on the topic could for instance read these references [29, 52]. Finally, it is reminded that the physics processes involved in these ion sources operation have been introduced in Sec. II.10.5.2.

II.10.5.8.1 Magnetron surface negative ion source

The concept of magnetron surface negative ion source was invented in the USSR [53]. It was next copied and enhanced in several laboratories. Figure II.10.44(top) presents a schematic of such an H^- ion source. Hydrogen gas is injected by a slit into a cavity having the shape of a racetrack. An external oven injects

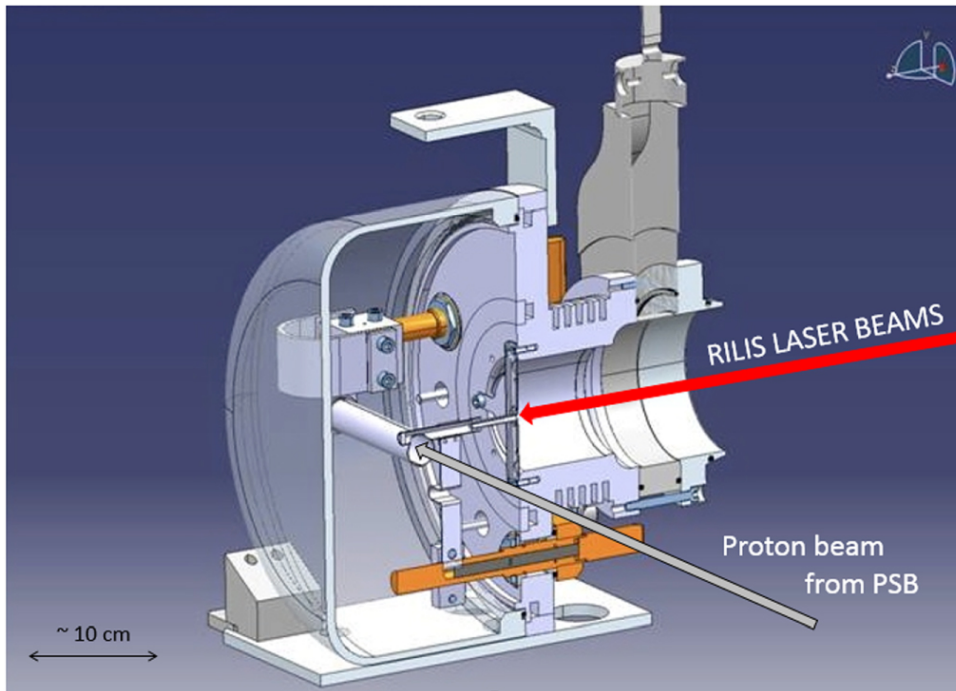


Fig. II.10.43: Cut away view of the computer assisted design of the CERN RILIS target ion source.

permanently a flux of Cs vapors that scatter and cover the whole cathode surface (as Cs atoms transiently stick on the surface before being re-evaporated). The source is surrounded by magnets providing the field necessary to sustain the magnetron arc discharge in the space between the anode and the cathode. The source is set to a high voltage and the H^- beam is co-extracted with electrons. The magnetic field used by the magnetron is favorably used to filter the unwanted electron beam out of the way, thanks to their magnetic rigidity, being much lower than the ions' one. A photograph of the Brookhaven National laboratory magnetron ion source is displayed in Fig. II.10.44(bottom) [54]. This type of ion source can produce ~ 100 mA of H^- in pulsed operation with a pulse width of $700 \mu\text{s}$ and a repetition rate of 7 Hz. Typical discharge voltage/current values are 150V/15A. Like electron sources, such a device suffers from sputtering and the source must be maintained after ~ 270 days.

II.10.5.8.2 Radio-frequency negative ion source

The radio frequency (RF) negative ion source is used to produce intense pulsed H^- beams. Figure II.10.45(top) proposes a sketch of this ion source. The chamber is surrounded by a multicusp magnetic field confining the plasma (see Sec. II.10.5.4.1). A RF internal antenna, operated at 2 MHz inductively creates eddy currents in the plasma sheath that heats electrons up to ~ 30 eV. The warm electrons diffuse toward the center of the chamber where they excite H_2 molecules to a high vibrational state H_2^v (see Sec. II.10.5.2). Close to the source exit, a weak dipolar magnetic field prevents the warm electrons to go further, while the excited atoms can pass through. The plasma after the filter is composed of low-energy electrons suitable to produce H^- by collision with the excited H_2^v molecules. The distance between the volume production of H^- and the plasma extraction electrode is limited to a few cm to minimize the probability of H^- destruction by collision. The H^- production is completed by a surface

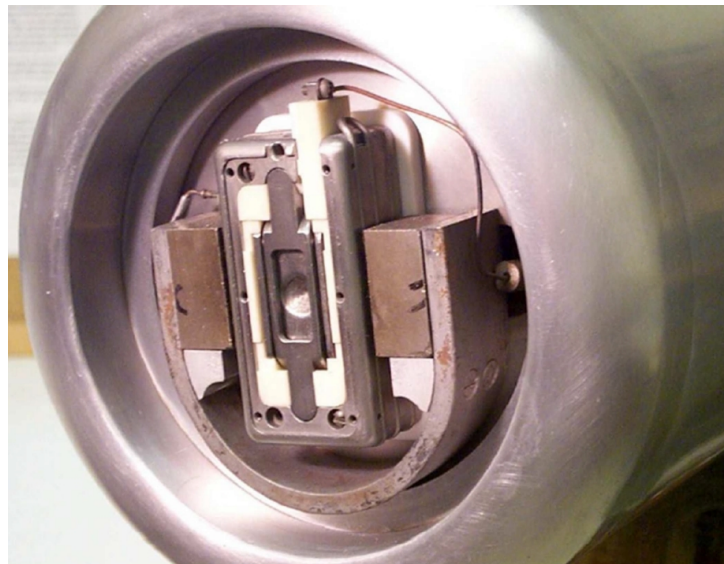
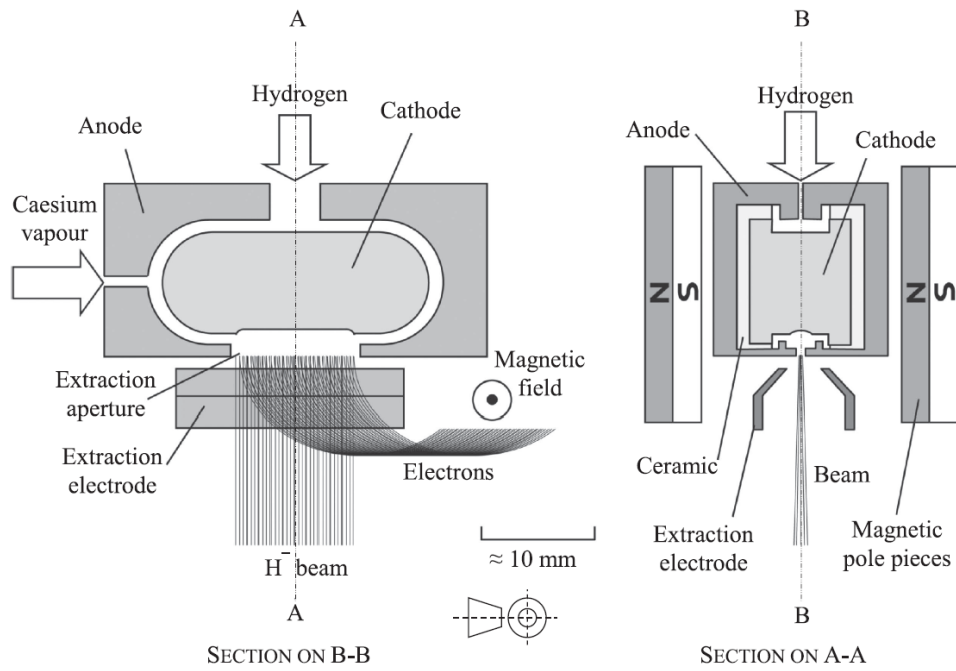


Fig. II.10.44: (Top) Schematic of a magnetron surface negative ion source [29]. (Bottom) Photo of the BNL magnetron source with the extraction electrode removed to see the inside [54]. The permanent magnets blocks sustaining the discharge are visible on both sides of the source.

production concentrated on the inner surface of a short collar located close to the extraction area. There, a Cs oven continuously provides Cs atoms sticking to the surface in contact with the plasma. This type of ion source produces ~ 50 mA of H^- beam during 1 ms with a 6% duty factor. The RF power required is ~ 50 kW. One should note that triggering the plasma requires a pre-existing seed plasma. It can be achieved by sending a 14 MHz pre-RF pulse, or by injecting a plasma puff generated by an auxiliary compact plasma source [56].

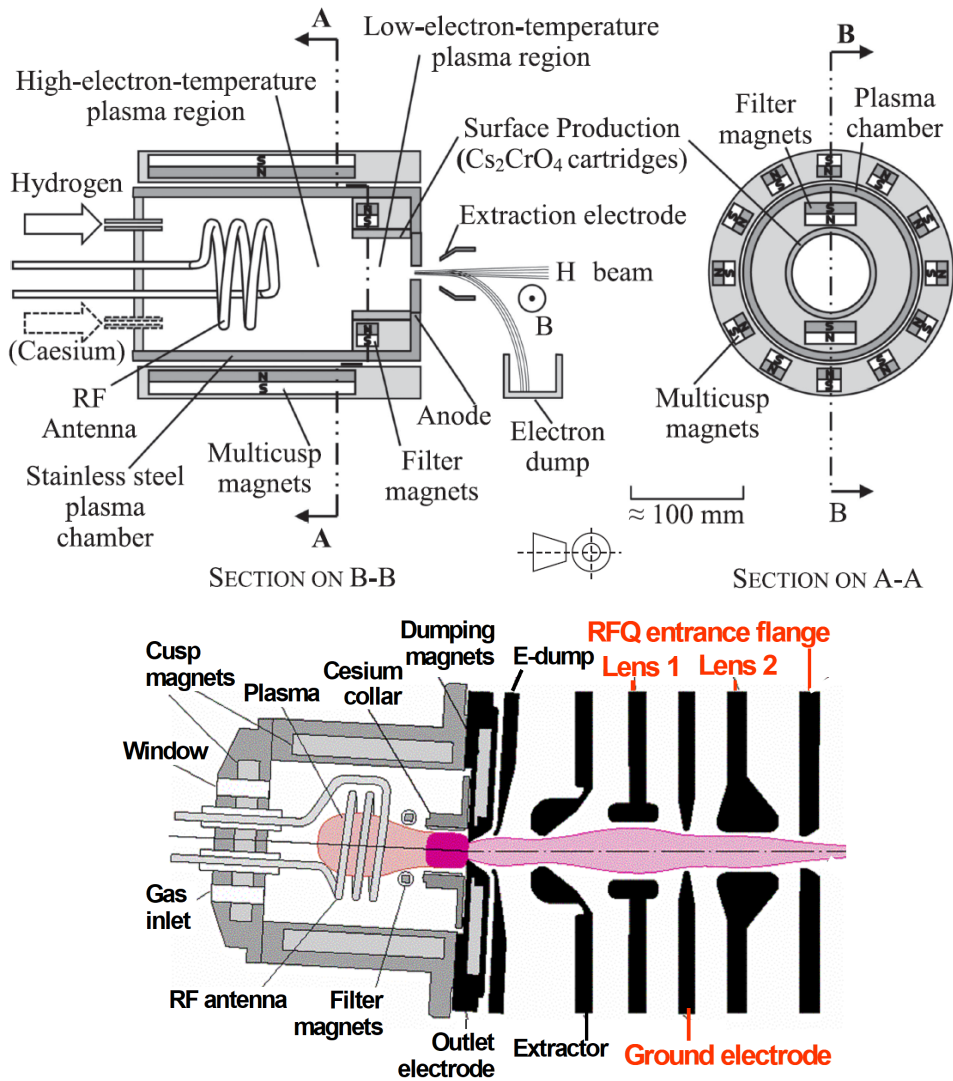


Fig. II.10.45: (Top) Schematic of a radio-frequency negative ion source both using volume and surface negative ion production [29]. (Bottom) Layout of the ONL radio-frequency source showing its sophisticated ion extraction system [55]. Courtesy of M. Stockli, Oak Ridge National Laboratory.

II.10.5.8.3 Neutral injectors for tokamaks

One of the ways to heat/sustain a tokamak magnetic fusion plasma is by injecting a heated neutral beam tangentially to its torus. The neutral beam energy must be adapted so that it reaches the plasma core and produce ohmic heating. The larger the plasma, the higher the neutral beam energy required to reach the plasma center. In the case of ITER, the neutral beam injection must be done at a kinetic energy of 1 MeV. Because the neutralization efficiency of a positive H^+ ion beam in a charge exchange cell is dramatically decreasing above a few 100 keV, it was chosen to use negative ion sources for which neutralization efficiency remains very high even at high energy. The total beam intensity from ITER source is expected at 40 A, a quite huge current for an ion source. The neutral injection for ITER is done by two sources delivering 20 A each. Each source is composed of eight individual negative RF ion source drivers set in a 2x4 array. This type of source has been presented in Sec. II.10.5.8.2. A sketch of a single

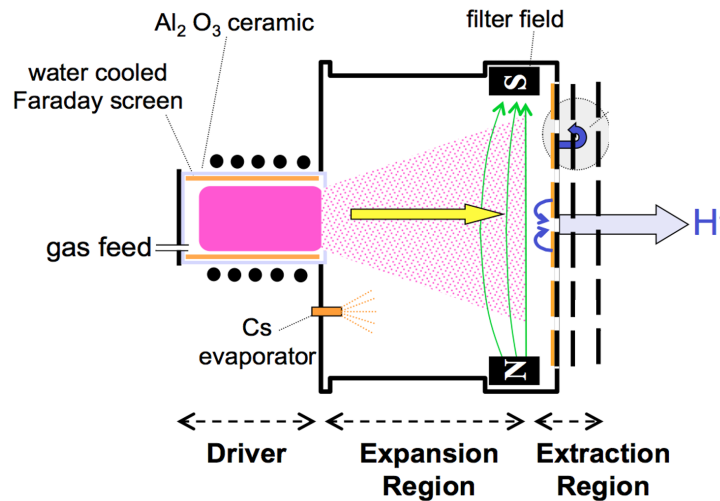


Fig. II.10.46: Sketch of an individual H^- ion source driver of ITER. W. Kraus, CERN Accelerator School 2012.

driver is presented in Fig. II.10.46. It is composed with a RF plasma source driver continuously fed with H_2 or D_2 gas. Next the plasma expands radially into an expansion chamber (whose transverse dimension is $\sim 0.3 \times 0.6 \text{ m}^2$). An evaporator projects Cs atom vapors through the expansion chamber in the same direction as the plasma. A dipolar magnetic field is located at the right end of the expansion chamber to block the warm electrons (H^- killers) created by the RF antenna while letting through the ions and neutrals. Finally, a set of three stacked grids are closing the chamber. See grid details in Fig. II.10.47(d). The first one is the plasma grid, which is set to the same electric potential as the driver. Cs atoms stick on the first grid, along with the former plasma content: H^- surface ionization occurs there. The second grid has the same potential as the plasma grid but is equipped with a network of small magnets which filter electrons and prevent them from being co-extracted. The third grid is set to a potential of +20 kV with respect to the source's driver. Focused beamlets of H^- are accelerated through each of the individual (14 mm diameter) circular holes forming the accelerating grid. Figure II.10.47(c) shows a cutaway view of a single driver assembly, while (a) and (b) display the whole ion source assembly composed of eight drivers respectively from the rear (drivers visible) and the front (extraction grid visible). At the final ITER installation, each source will be set to a 60 kV potential, then attached to a stack of five accelerating electrodes with a voltage difference of 200 kV.

II.10.5.9 Microwave source

The microwave source, or Taylor source [57], uses the electron cyclotron resonance (ECR) to heat the electrons in a plasma. The ECR condition is reached when an injected electromagnetic wave oscillates in a cavity at the same angular frequency ω_{RF} as the electrons rotating in a magnetic field B_{ecr} (see Eq. II.10.41)

$$\omega_{RF} = \omega_{ce} = \frac{qB_{ecr}}{m_e}, \quad (\text{II.10.50})$$

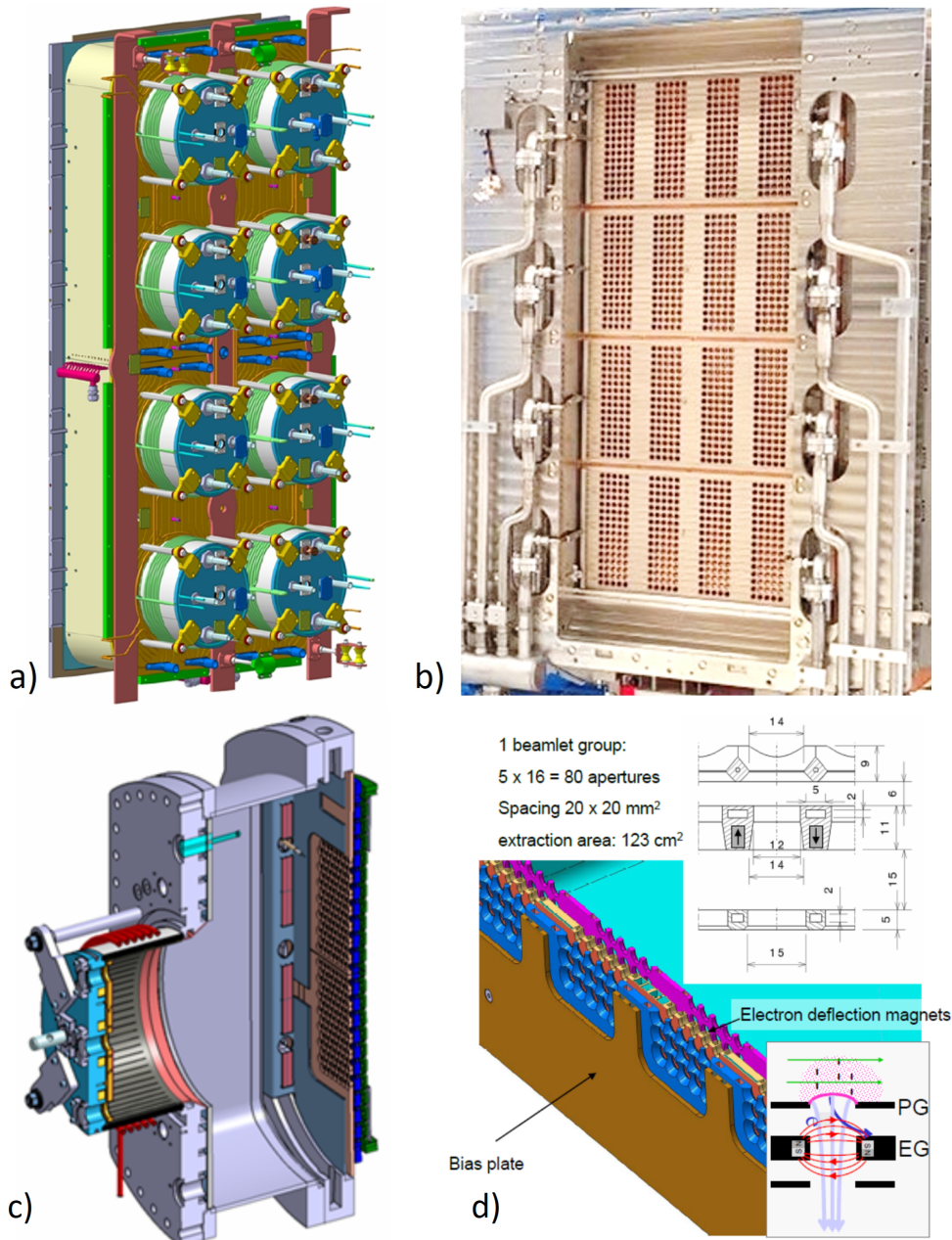


Fig. II.10.47: (a) Rear view showing a full ITER ion source module with eight drivers. (b) Front view photo of full ITER ion source module. (c) Cutaway view of an elementary driver source. (d) Details of an individual source extraction grid including magnetic H^- beamlet focusing. W. Kraus, CERN Accelerator School 2012.

where m_e and q are the mass and charge of electron and the frequencies are in unit of rad/s. Figure II.10.48 presents a layout of the SILHI ECR ion source installed at the SPIRAL2 accelerator [58]. The plasma cavity is a cylinder of ~ 10 cm diameter and ~ 10 cm length. The RF injected is produced by a 2.45 GHz 1 kW magnetron. The cavity is surrounded by a set of three permanent magnet cylinders generating a quasi flat axial magnetic field in the cavity, with the important condition that there exists at least one surface inside the chamber where the magnetic field intensity equals B_{ecr} , respect-

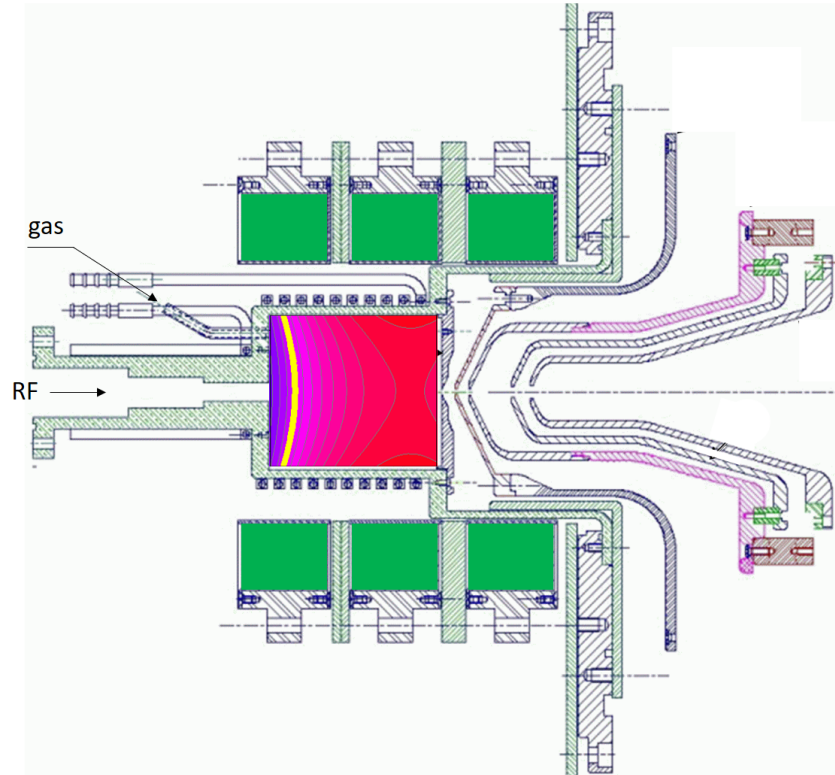


Fig. II.10.48: Layout of the SPIRAL2 SILHI ECR ion source installed at GANIL. Courtesy of R. Gobin, CEA, France. The density plot inside the cavity shows the magnetic field intensity and the yellow line the ECR magnetic surface (place where $B = B_{ecr}$).

ing Eq. II.10.50. When a cold electron passes the resonance zone (identified with the yellow line in Fig. II.10.48), it undergoes a resonance acceleration that increases its energy to ~ 10 -100 eV, allowing for subsequent electron impact ionization of the gas injected in the cavity. The charged particles in the plasma follow the magnetic field lines and ions are guided toward the plasma extraction electrode on the right side. This type of ion source is advantageously used to produce intense light gas ion beams of the order of ~ 100 mA. The axial magnetic field profile in the source is plotted in Fig. II.10.49 for both the original Taylor ion source and the SILHI version at SPIRAL2. Both sources can produce 100 mA of proton beam, despite a quite significant difference in the position and number of ECR magnetic surfaces (one for SILHI, two for Taylor). The main advantage of the ECR ion source with respect to arc discharge ion sources is that the power coupling to the electron is intangible: there are no filaments nor wearing parts. The maintenance of such an ion source ranges from three months to years, depending on the ion beam intensity extracted.

II.10.5.10 Multicharged ion sources

Multicharged ion sources are conveniently used to produce ion beams for accelerators, as accelerating a high charge state ion can either result in a higher final beam energy (case of cyclotron) or a shorter accelerator to provide a given final energy (case of linac). Modern and commonly used multi charged ion sources are electron cyclotron resonance ion sources (ECRIS) and electron beam ion sources (EBIS).

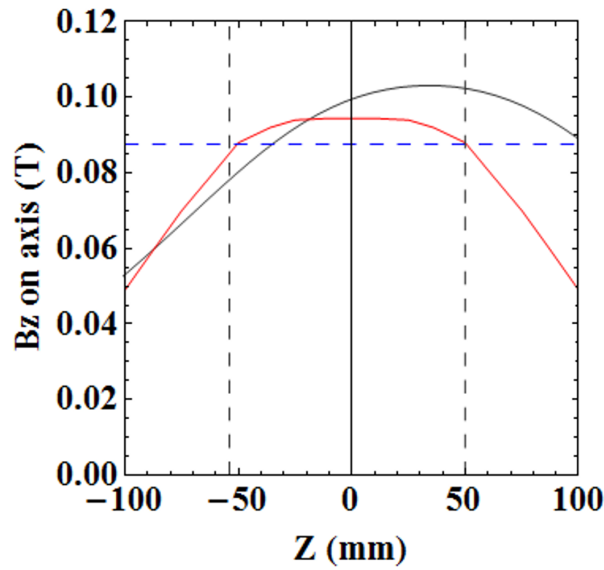


Fig. II.10.49: Magnetic field profile on the axis of the microwave source. The black curve is for the SILHI source at SPIRAL2, while the red curve shows the original Taylor magnetic design. The dashed blue line shows the magnetic field intensity for the ECR frequency of 2.45 GHz. The vertical dashed black lines indicate the position of the plasma microwave cavity.

Both are presented in this section, along with another R&D technique, yet under study: the laser ion source (LIS).

II.10.5.10.1 *Electron cyclotron resonance ion source*

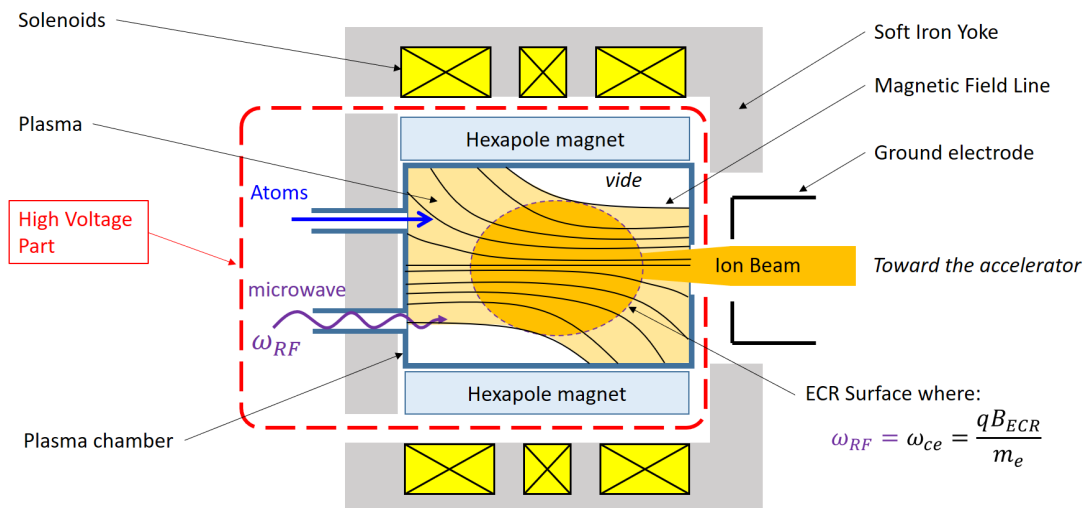


Fig. II.10.50: Sketch of a multicharged electron cyclotron resonance ion source.

Electron cyclotron resonance ion sources (ECRIS) were invented in the 60's by R. Geller [59] at Commissariat à l'Energie Atomique Grenoble (France). A sketch of a typical room temperature ECRIS is

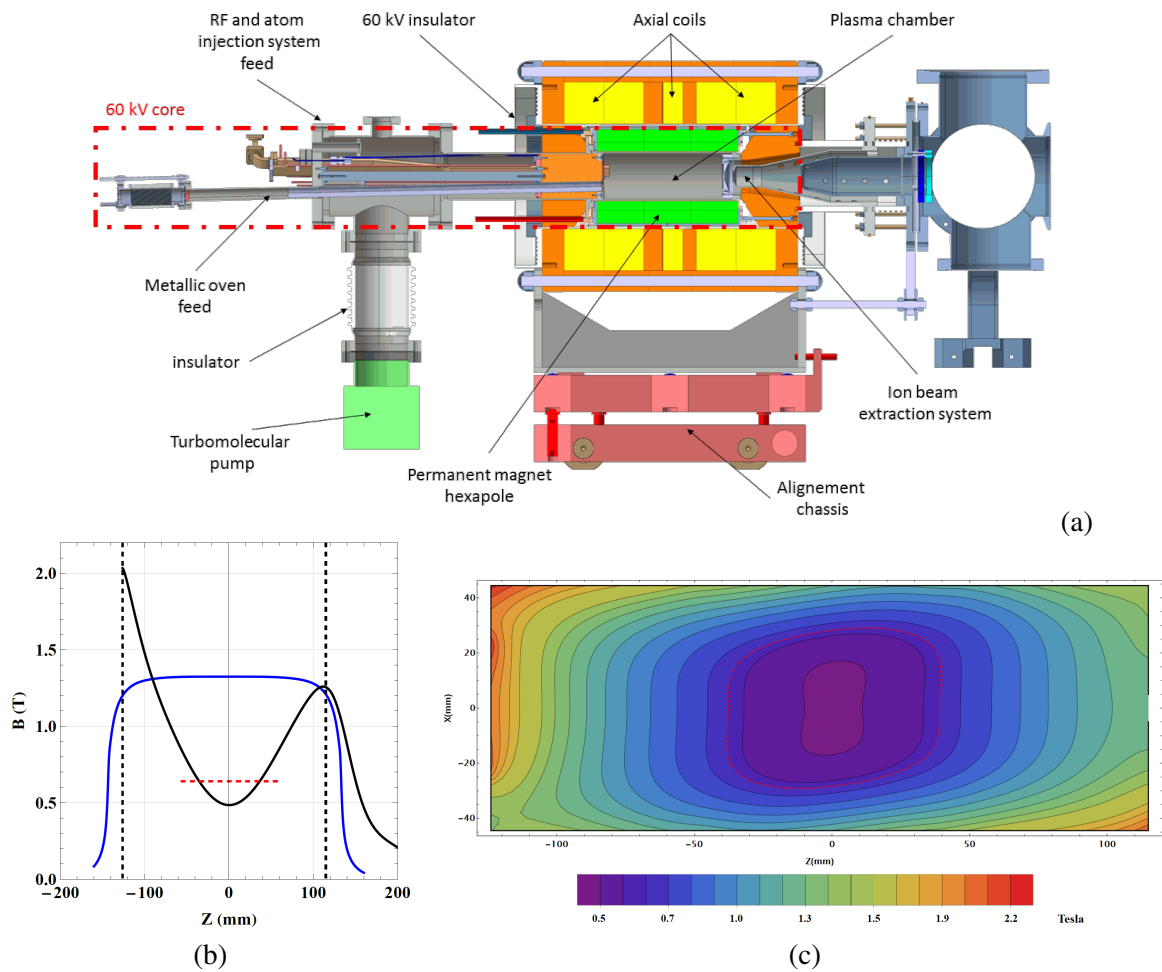


Fig. II.10.51: Example of the 18 GHz PHOENIX V3 ECRIS (GANIL) mechanics and magnetic field structure (a) ECRIS sectional view. (b) Axial magnetic profile (Black curve), radial hexapole magnetic profile measured at the plasma chamber wall (Blue curve). (c) Sectional view of the iso- B lines inside the plasma chamber. The resonance line $B=0.64$ T is indicated in dashed red in both (b) and (c) plots.

proposed in Fig. II.10.50. The ECRIS cylindrical plasma chamber is surrounded by a set of coils which generate an axial magnetic mirror (see Sec. II.10.5.4.1) and a hexapole, often made with permanent magnets. The superposition of the two magnetic field creates a magnetic bottle, or B -minimum, where the magnetic field intensity is minimum at the center and maximum at the plasma chamber wall. The magnetic field is especially designed to have a closed magnetic surface, the ECR zone, located far from the wall, where electrons can resonate with the injected microwave (see Sec. II.10.5.9, Eq. II.10.50 and Fig. II.10.50). The charged particles in the plasma follow the local field lines in the source, indicated in black solid lines in Fig. II.10.50. After an electron passes through the ECR surface, it gains kinetic energy and propagates toward the plasma chamber walls. But, because the magnetic field intensity increases, it can undergo a magnetic reflection (see Sec. II.10.5.4.1) and go back toward the ECR surface where it will be heated again. Magnetically confined electrons can make multiple passages through the ECR zone and reach a mean kinetic energy of the order of a few keV. Likewise, the ions are magnetically confined in the plasma and can be trapped up to hundreds of ms. The ions remain cold in the plasma

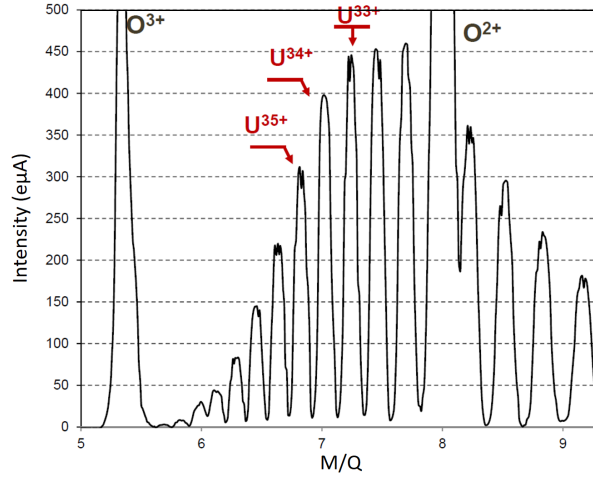


Fig. II.10.52: Ion beam spectrum recorded from the 28 GHz superconducting VENUS ECRIS (Lawrence Berkeley National Laboratory) operated at 28 GHz frequency. [60]

with a temperature of the order of $kT \sim 1\text{-}10$ eV. The hot electrons and the long ion lifetimes allow a step-by-step ionization of ions. A consensus exists on the presence of a dense electron population in the center of the cavity, around the ion source axis, which confines electrostatically the ions and helps to produce high charge state ions. The ECR plasma is strongly magnetized, out of equilibrium, anisotropic and inhomogeneous, making its modelling and understanding very complicated. The plasma is sustained by the constant injection of a microwave, of the order of 1 kW, and the injection of atoms. The collisions in the plasma redistributes the charged-particle velocities and constantly feeds the axial magnetic loss cone (see Sec. II.10.5.4.1) which brings the particles to the edge of the plasma where a round extraction electrode is located. The axial magnetic mirror is engineered to be asymmetric with the highest peak intensity on the injection side (the place where atoms and RF are injected) and the weakest axial peak on the extraction side (the place where ions are extracted, see Fig. II.10.51(b) and text below). With an asymmetric magnetic mirror, particles preferentially drift toward the extraction area to form an ion beam. The plasma chamber is set to a high voltage and the ion beam is accelerated by an electric field toward the following low-energy beam line. An important feature of ECRIS is that the ionic current extracted is proportional to the plasma density, which in turn is proportional to the RF frequency to the square

$$I_{\text{beam}} \approx \omega_{\text{RF}}^2 \approx B_{\text{ecr}}^2. \quad (\text{II.10.51})$$

This equation is known as the ECR scaling law: to produce a higher intensity multicharged ion beam, one can design an ion source with a higher magnetic field, but there is a catch. The optimal magnetic field to produce high charge state ions requires the last closed magnetic surface in the plasma chamber to be $B \sim 2B_{\text{ecr}}$ and an injection peak intensity on axis $\sim 3.5\text{-}4 B_{\text{ecr}}$ (see text below and Fig. II.10.51(b)). So increasing the plasma density requires to increase homothetically the overall intensity of the magnetic bottle. Figure II.10.51(a) presents a sectional view of the 18 GHz PHOENIX V3 ion source in operation at GANIL. The axial magnetic field (Fig. II.10.51(b)) is done with a set of axial room temperature coils. The soft iron yoke surrounding the coils allows reaching the iron saturation of $\sim 2\text{T}$ on the atom injection

side of the plasma chamber, while the other axial mirror peak, located on the ion extraction side, is set to a lower value (1.3 T here) to favor particle loss on this side. The hexapolar magnetic field is done with a Hallbach hexapole delivering a 1.25 T intensity at the wall. The ECR magnetic field to ensure a resonance at 18 GHz is $B_{\text{ecr}} = 0.64$ T and is indicated with a dashed red line on the plot. The iso-B lines inside the chamber are plotted in Fig. II.10.51(c). One can see that the magnetic field intensity is minimum at the center and increases toward the chamber walls to confine the plasma. The twist of the ECR zone (closed dashed red line) is a consequence of the interaction of the parasitic radial component generated by the axial coils and the hexapolar magnetic field. Above 18 GHz, ECRIS must use superconducting coils to produce the required plasma magnetic confinement intensity. An example of a uranium ion beam spectrum recorded with the VENUS 28 GHz superconducting ECRIS [60] is presented in Fig. II.10.52. The atom-to-ion conversion efficiency is of the order of 80% in ECRIS when gas is ionized. The production of various metallic elements is achieved with dedicated ovens that inject evaporated metallic atoms into the plasma where they are ionized in flight. The ionization efficiency for metals is in the range of 1–20%, and in some cases, up to 50-70% when the plasma chamber surface is heated to allow metal re-evaporation. The operational range of pressure in an ECRIS is $\sim 10^{-6}$ - 10^{-8} mbar.

II.10.5.10.2 Electron beam ion source

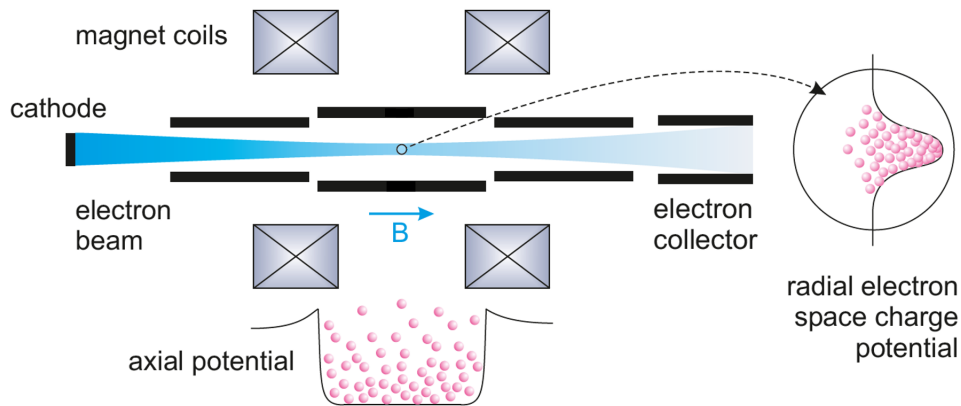


Fig. II.10.53: Diagram showing the principle of operation of an electron beam ion source (EBIS) [62].

The concept of electron beam ion source (EBIS) was invented at the Joint Institute for the Nuclear Research (Russia) in 1969 by Donets and his collaborators [61]. Figure II.10.53 presents the diagram of an EBIS [62]. On the left, a thermionic gun generates an electron beam which is accelerated toward an ion trap equipped with a set of drift tubes (voltage biased electrodes) and immersed into an axial magnetic field. The electron beam is focused by the magnetic field inside the trap. The electron beam is next dumped on an electron collector at the exit of the trap. Figure II.10.54 presents the distribution of electric potential in the EBIS. The electron gun is set to a negative potential U_K . The three drift electrodes are set to a positive high voltage U_1 , U_2 and U_3 respectively. The high voltage of the drift tubes accelerates the electron beam to reach (depending on the type of EBIS) an energy of a few keV to ~ 200 keV. All voltage electrodes are independently tunable. At the exit of the trap is located the

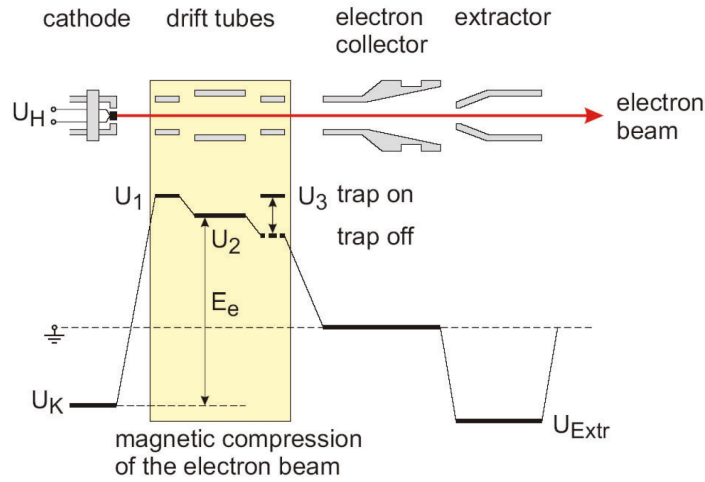


Fig. II.10.54: Electrical scheme of EBIS operation: U_K , cathode potential; U_{Ext} , ion extraction potential; U_H , potential at the cathode heater; U_1 , trap potential at the side of the electron gun; U_3 , trap potential at the ion extraction side (switched for pulsed ion extraction); U_2 , potential at the middle drift tube [62].

electron collector set to the ground potential (place where the electron beam is decelerated, defocused and eventually dumped) and finally the ion beam extraction electrode with a negative potential U_{Ext} . The electrodes inside the trap are biased to form an axial electrostatic well, where $U_2 < U_1$ and $U_2 < U_3$, which axially confines ions (see Sec. II.10.5.4.2). The space charge of the electron beam creates a negative potential that confines the ions radially (see also Sec. II.10.5.4.2). The electron beam energy is tuned to optimize the multicharged ion production by electron impact. The EBIS operates as follow to create an ion beam. First, the gas of interest is injected into the trap. Then, the atoms of the gas are bombarded by the energetic electrons. Once an atom is ionized in the electron beam, it is automatically trapped electrostatically in the source, both axially and radially. The ion will next undergo a step-by-step ionization by electron impact. Thanks to a very low base vacuum in EBIS (in the range 10^{-12} to 10^{-10} mbar), the charge exchange process is very limited in the trap and very high charge state ions can be produced. The accumulation of ions into the trap is limited by the total electric charge ΔQ of the electron beam in the trap of length L [62]

$$\Delta Q = \frac{I_e L}{v_e} = \frac{I_e L}{\sqrt{2K_e/m_e}}, \quad (\text{II.10.52})$$

where $I_e = \frac{dQ}{dt}$ is the electron beam intensity, $v_e = \frac{dz}{dt}$, K_e , m_e are respectively the electron velocity, kinetic energy and mass. Once the ion trap is full, the voltage U_3 is set to a value lower than U_2 : the axial electrostatic trap is opened on the extraction side. A bunch of ions is accelerated by the extraction system toward the beam line. The trapping time of ions in EBIS can reach seconds when one wants to produce very high charge state or even bare ions. During this time, ions are being slowly heated by collisions. If one reduces the voltage U_3 in such a way that $U_2 < U_3 < U_1$, a constant flow of ions will be extracted from the EBIS, those whose velocity (increased by collisions) is sufficient to overcome the potential barrier. Figure II.10.55 illustrates the simulated evolution of a xenon ion charge state distribution (CSD) into an

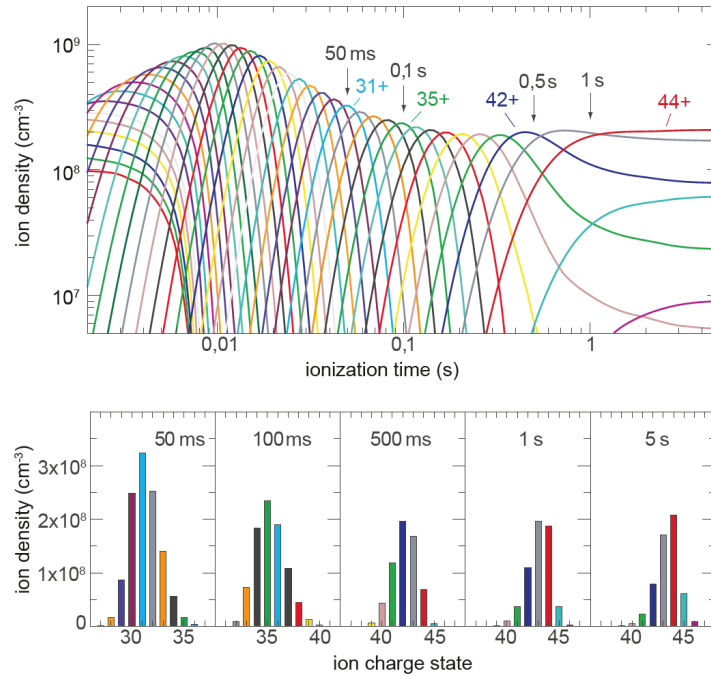


Fig. II.10.55: Simulation of the evolution of a xenon population ion charge state in an EBIS trap at Dresden as a function of time with $I_e = 40$ mA, $E_e = 15$ keV and $P = 2 \cdot 10^{-9}$ mbar [62].

EBIS at Dresden [62] as a function of time. One can see how the CSD evolves with time from low to high charge ions and finally reaches an equilibrium after 5 s with an ion density distribution peaked on Xe^{44+} . One can note that EBIS CSD is concentrated on a few charge states, to be compared with the ECRIS CSD width on Fig. II.10.52. It is possible to produce beams from condensable elements by injecting a bunch of 1^+ ions in the EBIS by its extraction size, reducing transiently the voltage of U_3 to let the 1^+ ion in and increasing U_3 once the ion bunch is injected to trap the ions [63]. The subsequent multi-ionization process is identical as the one previously explained. A state of the art high-intensity EBIS is the RHIC-EBIS [64] installed at Brookhaven National Laboratory, USA. Its mechanical design is displayed in the Fig. II.10.56. This ion source has a 188-cm-long ion trap and utilizes 7-10 A of electron beam with a 5 T superconducting solenoid. Because the drift tube is very long, it can store a large quantity of ions (80 nC per pulse) and produce high-intensity pulses of various chemical elements by using the 1^+ ion injection technique described earlier. The beam pulse intensity from the RHIC source can reach 1.7 mA for 10-40 μs with a 5-10 Hz repetition rate. A beam of interest for the accelerator is Au^{32+} . Finally, it is worth mentioning that EBIS are conveniently used as charge breeders [65] to boost the radioactive ion beam (RIB) charge state in dedicated facilities as the EBIS low operation pressure provides RIB with a purity compatible with the needs of the physics experiments.

II.10.5.10.3 Laser ion source (LIS)

A laser ion source (LIS) consists of a vacuum chamber equipped with a solid target. See the example of the CERN R&D LIS developed in the early years of 2000's decade on Fig. II.10.57. A powerful short laser pulse is sent on the target. The laser is located outside of the chamber, in a dedicated room. The

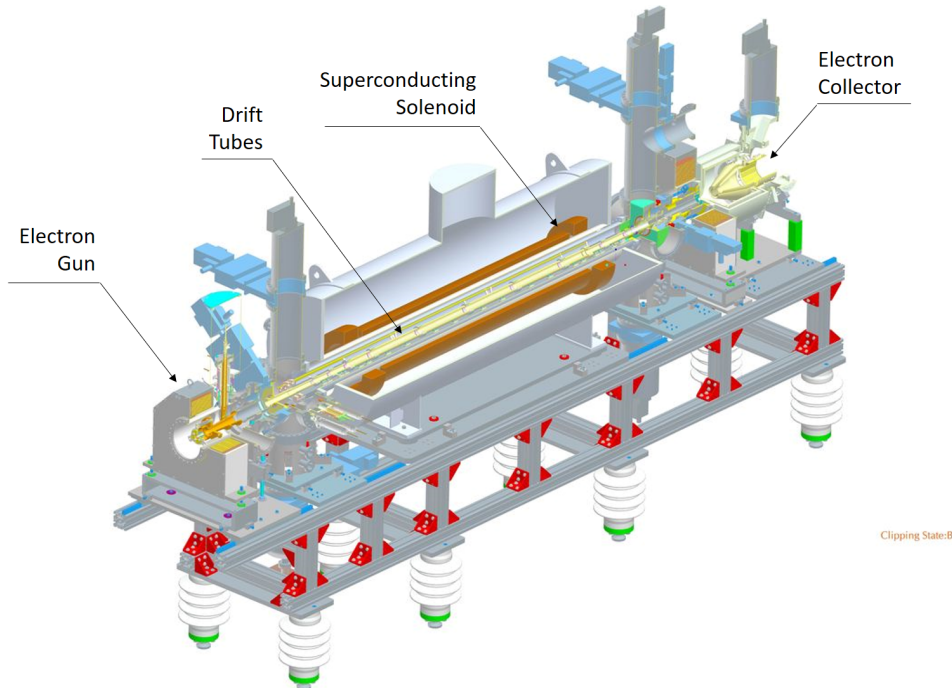


Fig. II.10.56: Cutaway view of the state-of-the art RHIC-EBIS mechanical design [64].

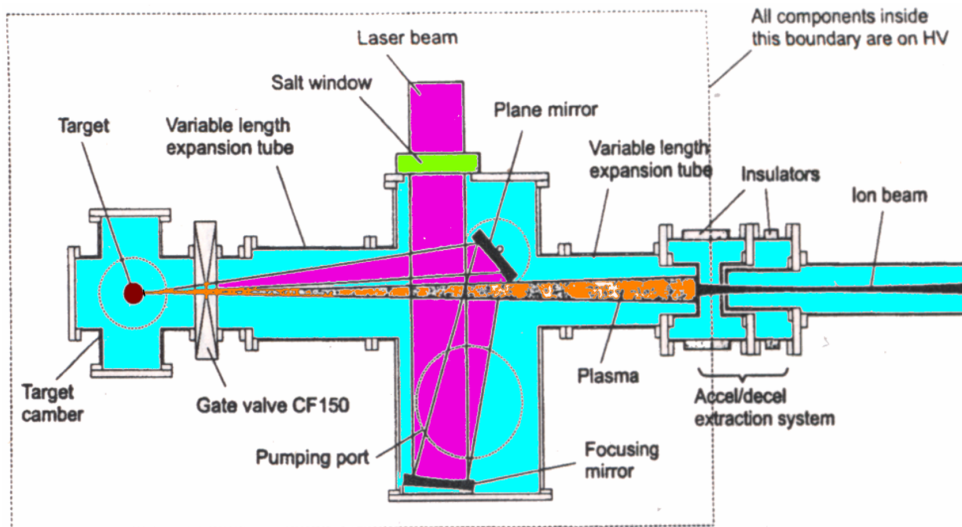


Fig. II.10.57: Layout of the CERN prototype laser ion source studies in the early years 2000.

laser pulse is guided toward the reaction chamber by a set of mirrors and finally focused on the target to maximise the local power density deposition. The local energy deposited by the laser is sufficient to vaporize the target surface. The subsequent heating of the vapor by the laser electromagnetic wave creates a dense hot plasma (meaning that the ions and electrons are at a thermal equilibrium) with a temperature of the order of ~ 10 keV. This high temperature allows to multi-ionize very efficiently the atoms from the target. Naturally, a plasma jet is formed and expands in the chamber with a direction perpendicular to the target surface. In the case of the CERN LIS, the target chamber is set to a high voltage and the plasma

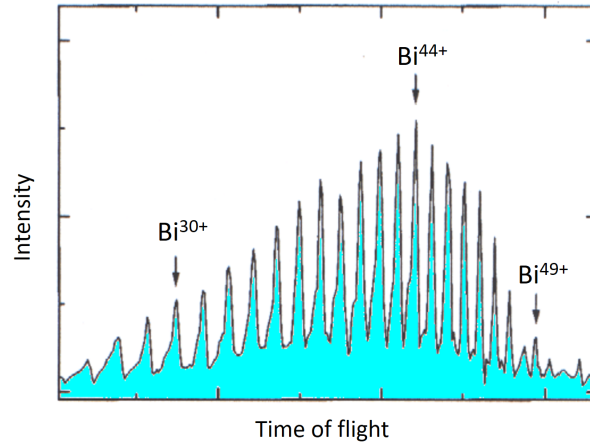


Fig. II.10.58: Bismuth ion beam charge state distribution function measured in a Faraday cup after the CERN LIS.

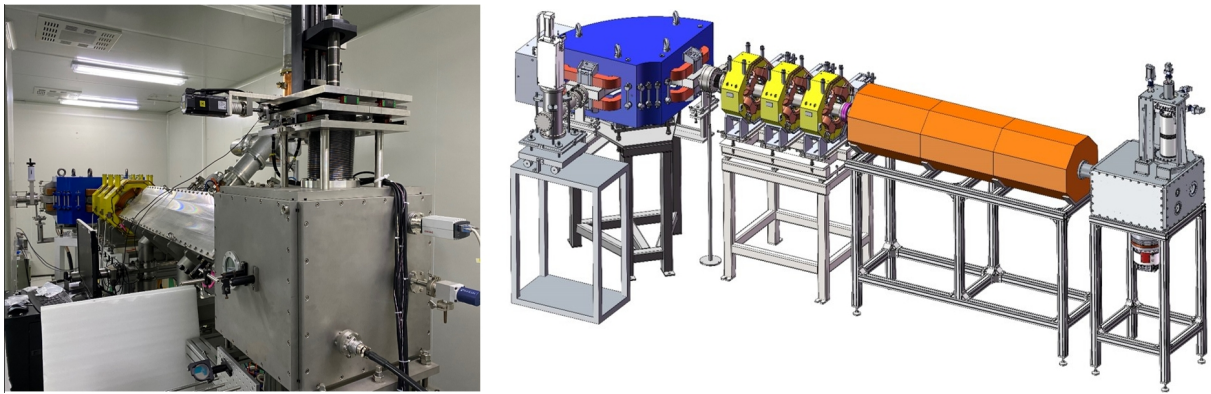


Fig. II.10.59: Photograph and mechanical design view of the IMP CAS LIS test bench. From left to right, one can see the LIS chamber, RFQ and the LEBT. Courtesy of Y. Zhao, IMP CAS.

beam is accelerated by a set of high voltage electrodes. The laser was providing a 100 J energy pulse over the 50 ns pulse. The power density at the target reaches $10^{13} \text{ W.cm}^{-2}$. Figure II.10.58 shows an example of ion beam CSD measured in a Faraday cup upstream the source (time of flight measurement: the ions reach the detector at different times, depending on their velocity, function of the ion charge state). Impressive charge state up to Bi^{49+} was recorded. The drawback of the LIS hot plasma is that the ions are produced with an important ion transverse energy spread ($\sim 10 \text{ keV}$). To cope with the large transverse beam emittance, the ion beam is immediately injected into a RFQ, granting both focusing and acceleration of the ion charge state of interest. The goal of this R&D was to explore the possibility to take advantage of the high-intensity and short pulse length to inject in one turn the beam directly into a LHC chain storage synchrotron at once, instead of making a multi-turn injection with a classical pulsed ion source (having a lower intensity and a longer pulse duration). The project was stopped by lack of funding. In the 2010's years, a new R&D on LIS started at the Institute of Modern Physics of Lanzhou (China) with possible societal applications like hadron therapy and pulsed neutron beam generation. Here, the source uses a commercial laser with a wavelength of 1064 nm, a power of 1-8 J and a pulse

duration of 8 ns. The source produces for instance 180 mA of pulsed C^{6+} & Al^{11+} . Using the RFQ and LEPT presented in Fig. II.10.59, 13 mA of pulsed C^{6+} beam were measured after the bending magnet in a Faraday cup with an energy of 586 keV/A. The energy spread is measured at ± 8 keV/A. The R&D on LIS is still going on, with interesting prospects.

II.10.6 Exercises

II.10.6.1 Electron source beam emittance

A thermionic electron source has a flat disk shape cathode with radius $R = 5$ mm. The cathode is heated at $T = 2000$ K. The electrons are accelerated by a high voltage potential of -100 kV. The horizontal normalized beam emittance is defined by

$$\epsilon_{N,x} = \gamma\beta\sigma_x\sigma_{x'} \quad ,$$

where γ , β are the usual relativistic factors, σ_x is the root mean square of beam position along the direction x and $\sigma_{x'}$ is the root mean square of the electron velocity distribution function along direction x .

1. Show that $\sigma_x = \frac{R}{2}$.

It is assumed that the electrons are uniformly extracted from the cathode disk.

2. Show that $\sigma_{x'} = \sqrt{\frac{kT}{m_e}}$.

It is assumed that the electrons are following the Maxwell-Boltzmann statistics. The associated normalized electron velocity distribution function along x is given by

$$\frac{dp(v_x)}{dv_x} = \left(\frac{m}{2\pi kT}\right)^{\frac{1}{2}} e^{-\frac{mv_x^2}{2kT}} \quad .$$

It is recalled that

$$\int_{-\infty}^{+\infty} e^{-x^2} dx = \sqrt{\pi} \quad .$$

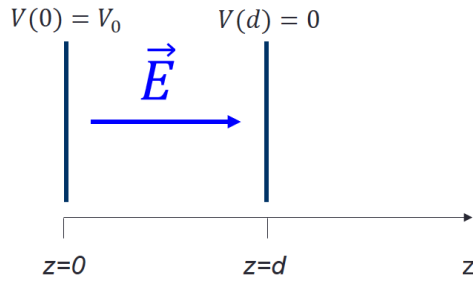
3. Calculate $\epsilon_{N,x}$.
4. What would be $\epsilon_{N,y}$ value?

II.10.6.2 Ideal particle extraction

Assuming a one dimension problem, with two infinite parallel plates separated by a distance d and creating a difference of potential V_0 , demonstrate from $\Delta V = -\frac{\rho}{\epsilon_0} = 0$ that

$$\vec{E} = \frac{V_0}{d} \vec{z} \quad ,$$

$$V(z) = V_0 \frac{(d-z)}{d}, \quad z \leq d \quad .$$

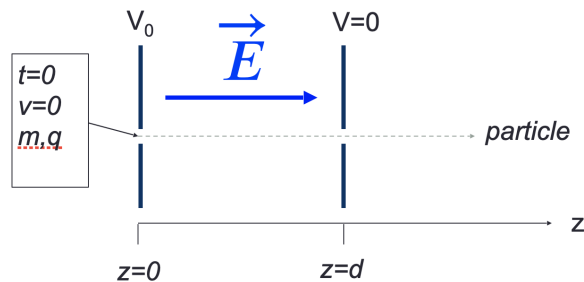


II.10.6.3 Particle acceleration at extraction

Using Newton's second law, assuming a geometry similar to the exercise in Sec. II.10.6.2, derive the evolution of the velocity of a particle with charge q , mass m , versus z in the accelerating gap (for non-relativistic particles)

$$v(z) = \sqrt{\frac{2qV_0z}{m}}, \quad z \leq d \quad ,$$

$$v(z) = v(d) = \sqrt{\frac{2qV_0}{m}}, \quad z > d \quad .$$



II.10.6.4 Particle acceleration at the extraction

A transverse constant velocity is added with respect to the previous exercise (see Sec. II.10.6.3)

$$\vec{v}_y = v_y \vec{y}, \quad \text{notation: } v_z = v = v_z(d) \quad .$$

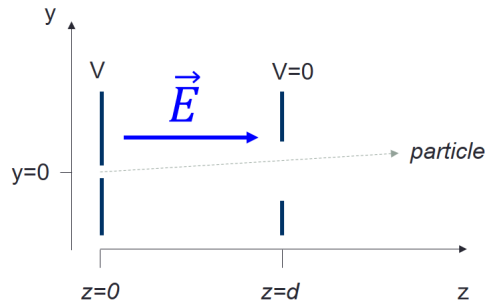
Show that

$$y(z) = \frac{v_y}{v} 2\sqrt{dz}, \quad z \leq d \quad ,$$

$$y(z) = \frac{v_y}{v} (z + d), \quad z > d \quad .$$

II.10.6.5 The Child Langmuir law: space charge limitation of particle extraction

Assume a one dimension extraction of particles (mass m , charge q). The geometry and notations for the problem are identical to the exercise 2 (see Sec. II.10.6.2). The static electric field generated by the two



electrodes is

$$\vec{E}_0 = \frac{V_0}{d} \vec{z}.$$

Assume now the charge density of particles $\rho(z)$ in the gap. There, the particles create a space charge electric field $\vec{E}_{sc}(z)$ which disrupts the former static electric field \vec{E}_0 so that the actual local electric field is now

$$\vec{E}(z) = \vec{E}_0 + \vec{E}_{sc}(z) \quad .$$

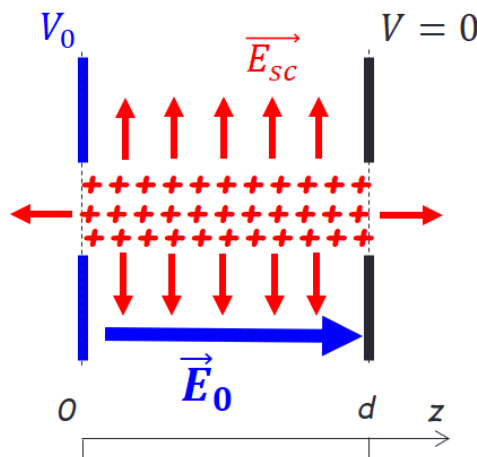
In this exercise, it is proposed to calculate the actual electric field (and associated electric potential) in the extraction gap. To solve the problem, the following general equations are used

$$\Delta V = -\frac{\rho(z)}{\epsilon_0} \quad ,$$

$$\text{div } \vec{J} = \frac{\partial \rho(z)}{\partial t} \quad ,$$

$$\vec{J} = \rho(z) \vec{v}(z) \quad ,$$

where V is the electric potential, \vec{J} the electric current density and \vec{v} the particle velocity.



II.10.6.5.1 Using the conservation of energy, show that

$$v(z) = \sqrt{\frac{2q(V_0 - V(z))}{m}} \quad , \quad 0 \leq z \leq d \quad .$$

II.10.6.5.2 Assuming a stationary problem, show that

$$J(z) = J(0) = J_0 = \rho(z)v(z) \quad .$$

II.10.6.5.3 Show that $V(z)$ is a solution of

$$\frac{d^2V(z)}{dz^2} = -\frac{J_0}{\epsilon_0} \sqrt{\frac{m}{2q}} (V_0 - V(z))^{-1/2} \quad .$$

We set $k = \frac{J_0}{\epsilon_0} \sqrt{\frac{m}{2q}}$ and $U(z) = V_0 - V(z)$, the equation writes

$$\frac{d^2U}{dz^2} = kU^{-1/2} \quad .$$

II.10.6.5.4 Introducing the electric field $E(z)$ and using $\vec{E} = -\vec{\nabla}V$, show that

$$\frac{d^2U}{dz^2} = E \cdot \frac{dE}{dU} \quad \text{and} \quad EdE = kdU/\sqrt{U} \quad .$$

II.10.6.5.5 Deduct that

$$E^2(z) - E^2(0) = 4k \left(\sqrt{U(z)} \right), \quad \forall 0 \leq z \leq d \quad .$$

II.10.6.5.6 The condition for the particle extraction to be blocked by space charge is reached when the space charge density in the gap is so high that it screens the electric field at $z = 0$, $E(0) = 0$. Then, available particles cannot be accelerated anymore. Integrate from $z = 0$ to $z = d$ to find

$$\frac{4}{3} [U(d)]^{3/4} = \sqrt{4kd} \quad .$$

II.10.6.5.7 Deduct that the current density J_0 blocking the particle extraction is such that

$$J_0 = \frac{4\epsilon_0}{9} \sqrt{\frac{2q}{m}} \frac{V_0^{3/2}}{d^2} \quad .$$

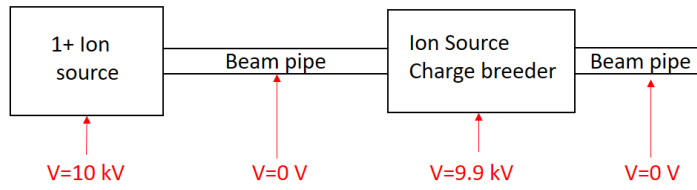
This is the Child Langmuir current density limit!

II.10.6.6 Ion Charge breeding

A 1^+ ion source delivers a ^{39}K potassium beam. Then ion source potential is set to 10 kV.

II.10.6.6.1 What is the ion velocity? Is it relativistic?

It is reminded that the atomic mass unit is $amu = 931.49 \text{ MeV}/c^2$.



II.10.6.6.2 The ions are injected into an ECR charge breeder whose plasma is set to the high voltage of 9.90 kV. At what energy does the ^{39}K ions pass into the plasma? What is their velocity?

II.10.6.6.3 The mean electron kinetic energy in the plasma is 90 eV. The ionization potential to pass from $^{39}\text{K}^+$ to $^{39}\text{K}^{2+}$ is $P_{1\rightarrow 2} = 31.63$ eV. The number of electrons on the outer subshell is $g_1 = 6$. Using the simplified Lotz formula below, calculate the electron impact cross section σ to pass from $^{39}\text{K}^+$ to form $^{39}\text{K}^{2+}$.

The simplified Lotz cross section formula is

$$\sigma \sim 4.5 \times 10^{-14} g_1 \frac{\log\left(\frac{K}{P_{1\rightarrow 2}}\right)}{K P_{1\rightarrow 2}} \text{ cm}^2, \quad (\text{II.10.53})$$

where K is the electron kinetic energy responsible for the ionization process.

II.10.6.6.4 The plasma electron density is $n = 10^{12} \text{ cm}^{-3}$. Calculate the ion mean free path associated with the electron impact collision of the former question

$$\lambda = \frac{1}{\sigma n}.$$

II.10.6.6.5 The plasma length is $L = 50 \text{ cm}$. Demonstrate that the number N of remaining $^{39}\text{K}^+$ beam after the crossing of the plasma is $N(L) = N(0)e^{-L/\lambda}$. Deduce the actual ratio of $^{39}\text{K}^+$ converted to $^{39}\text{K}^{2+}$ in the plasma.

II.10.6.7 Electron Beam Ion Source (EBIS)

An EBIS is equipped with a planar LaB_6 thermionic cathode heated at 2000 K with a disk diameter of 4 mm.

II.10.6.7.1 What is the electron beam intensity generated?

Use the modified Richardson-Dushman equation to calculate the current density.

$J = A_0 \lambda T^2 e^{-W/kT}$, with $A_0 = \frac{4\pi m_e k^2 e}{h^3} = 1.20173 \times 10^6 \text{ A/m}^2/\text{K}$ and $\lambda = 0.24$. The LaB_6 work function is 2.4 eV.

Table II.10.5: Argon ionization potential energies (IP).

IP	1	2	3	4	5	6	7	8	9	10	11	12	13	14	15	16	17	18
(eV)	16	28	41	60	75	91	124	143	422	479	539	618	686	756	855	918	4121	4426

II.10.6.7.2 *The electron beam surface is compressed by the EBIS magnetic field by a factor of 10. What are the beam radius and the electron current density J in the EBIS?*

II.10.6.7.3 *The electron beam is accelerated by a -6 kV high voltage. A population of N Ar^{1+} ions is trapped in the EBIS. Ar^{2+} ions are created by electron impact. The population evolution of Ar^{1+} and Ar^{2+} ions with time is noted $N^{1+}(t)$ and $N^{2+}(t)$ respectively. Show that*

$$N^{2+}(t) = N(1 - e^{-\nu t}).$$

$\nu = n_e \sigma_{1+ \rightarrow 2+} v_e$ is the collision rate.

$J = en_e v_e$ is the current density, e the electric charge.

v_e is the electron velocity.

$\sigma_{1+ \rightarrow 2+}$ is given by the simplified Lotz formula (see Eq. II.10.53 in Sec. II.10.6.6, considering $g_1 = 5$).

II.10.6.7.4 *Calculate the time when $N^{2+}(t) = N^{1+}(t) = \frac{N}{2}$.*

II.10.6.7.5 *The electron beam voltage is set to 900 V. What is the maximum argon ion charge achievable in the source?*

The argon ionization potential are proposed in the Tab. II.10.5.

II.10.7 Solutions

II.10.7.1 Solutions to exercise 1 (see Sec. II.10.6.1)

Uniformly distributed random points inside a circle of radius R

With the cartesian coordinates, the probability distribution function is

$$f(x, y) = \begin{cases} \frac{1}{\pi R^2}, & \text{if } x^2 + y^2 \leq R^2 \\ 0, & \text{elsewhere} \end{cases}.$$

When changing to cylindrical r, θ coordinates

$$x = r \cos \theta, \quad y = r \sin \theta \quad ,$$

we can express the probability distribution function $g(r, \theta)$ in cylindrical coordinates as

$$I = \int_{r=0}^R \int_{\theta=0}^{2\pi} g(r, \theta) dr d\theta = \iint_{x^2+y^2 \leq R^2} f(x, y) dx dy = 1 \quad .$$

The change of coordinate from cartesian to cylindrical is ruled by the Jacobian matrix J

$$\begin{pmatrix} dx \\ dy \end{pmatrix} = J \begin{pmatrix} dr \\ d\theta \end{pmatrix} = \begin{pmatrix} \frac{\partial x}{\partial r} & \frac{\partial x}{\partial \theta} \\ \frac{\partial y}{\partial r} & \frac{\partial y}{\partial \theta} \end{pmatrix} \begin{pmatrix} dr \\ d\theta \end{pmatrix} = \begin{pmatrix} \cos \theta & -r \sin \theta \\ \sin \theta & r \cos \theta \end{pmatrix} \begin{pmatrix} dr \\ d\theta \end{pmatrix}.$$

System from which it can be deduced that

$$dx dy = \det(J) dr d\theta = r dr d\theta.$$

So,

$$I = \iint_{x^2+y^2 \leq R^2} f(x, y) dx dy = \int_{r=0}^R \int_{\theta=0}^{2\pi} \frac{1}{\pi R^2} r dr d\theta.$$

The probability distribution function expressed in cylindrical coordinates is finally $g(r, \theta) = \frac{r}{\pi R^2}$.

$$\langle x \rangle = \int_0^R \int_0^{2\pi} \frac{xr}{\pi R^2} dr d\theta = \int_0^R \frac{r^2}{\pi R^2} dr \int_0^{2\pi} \cos \theta d\theta = 0.$$

$$\langle x^2 \rangle = \int_0^R \int_0^{2\pi} \frac{x^2 r}{\pi R^2} dr d\theta = \int_0^R \int_0^{2\pi} \frac{r^3 \cos^2 \theta}{\pi R^2} dr d\theta = \frac{1}{\pi R^2} \left[\frac{r^4}{4} \right]_0^R \int_0^{2\pi} \frac{1}{2} (\cos 2\theta + 1) d\theta = \frac{R^4}{4\pi R^2} \pi = \frac{R^2}{4}.$$

Therefore,

$$\sigma_x = \sqrt{\langle x^2 \rangle} = \frac{R}{2}.$$

Maxwell-Boltzmann velocity distribution function

$$P(v_x, v_y, v_z) dv_x dv_y dv_z = \left(\frac{m}{2\pi kT} \right)^{\frac{3}{2}} e^{-\frac{m(v_x^2 + v_y^2 + v_z^2)}{2kT}} dv_x dv_y dv_z,$$

$$\iiint_{-\infty}^{+\infty} P dv_x dv_y dv_z = \int_{-\infty}^{+\infty} p(v_x) dv_x \int_{-\infty}^{+\infty} p(v_y) dv_y \int_{-\infty}^{+\infty} p(v_z) dv_z = 1,$$

with

$$p(v_x) dv_x = \left(\frac{m}{2\pi kT} \right)^{\frac{1}{2}} e^{-\frac{mv_x^2}{2kT}} dv_x,$$

$$\langle v_x \rangle = \left(\frac{m}{2\pi kT} \right)^{\frac{1}{2}} \int_{-\infty}^{+\infty} v_x e^{-\frac{mv_x^2}{2kT}} dv_x = \left(\frac{m}{2\pi kT} \right)^{\frac{1}{2}} 2 \int_0^{+\infty} (v_x - v_x) e^{-\frac{mv_x^2}{2kT}} dv_x = 0,$$

$$\langle v_x^2 \rangle = \left(\frac{m}{2\pi kT} \right)^{\frac{1}{2}} \int_{-\infty}^{+\infty} v_x^2 e^{-\frac{mv_x^2}{2kT}} dv_x \quad .$$

Using the integration by parts' technique $\int (uw)' = [uw] = \int u'w + \int uw'$,

$$u'(v_x) = v_x e^{-\frac{v_x^2}{A}} \quad \Rightarrow \quad u(v_x) = -\frac{A}{2} e^{-\frac{v_x^2}{A}} \quad ,$$

$$w(v_x) = v_x \quad \Rightarrow \quad w'(v_x) = 1 \quad .$$

Thus,

$$\langle v_x^2 \rangle = \int_{-\infty}^{+\infty} v_x^2 e^{-\frac{mv_x^2}{2kT}} dv_x = \left(\frac{m}{2\pi kT} \right)^{\frac{1}{2}} \left(\left[-\frac{2kT}{2m} e^{-\frac{mv_x^2}{2kT}} v_x \right]_{-\infty}^{+\infty} - \int_{-\infty}^{+\infty} \frac{-2kT}{2m} e^{-\frac{mv_x^2}{2kT}} dv_x \right) \quad ,$$

$$\langle v_x^2 \rangle = \left(\frac{m}{2\pi kT} \right)^{\frac{1}{2}} \left(0 + \frac{kT}{m} \int_{-\infty}^{+\infty} e^{-y^2} dy \sqrt{\frac{2kT}{m}} \right) \quad ,$$

$$\langle v_x^2 \rangle = \frac{kT}{m} \quad .$$

Therefore,

$$\sigma_{x'} = \sqrt{\langle v_x^2 \rangle} = \sqrt{\frac{kT}{m}} \quad ,$$

and

$$\epsilon_{N,x} = \sigma_x \sigma_{x'} = \frac{R}{2} \sqrt{\frac{kT}{m}} \quad .$$

The intermediate results to calculate the electron source normalized emittance are proposed in the Tab. II.10.6. The value for the normalized emittance is $\epsilon_{N,x} = 0.55 \pi \cdot \text{mm} \cdot \text{rad}$. Finally, by symmetry of the problem, the value of the vertical emittance is equal to the horizontal one $\epsilon_{N,x} = \epsilon_{N,y}$.

II.10.7.2 Solutions to exercise 2 (see Sec. II.10.6.2)

$$(1) \quad \vec{E} = -\vec{\nabla}V \quad .$$

$$(2) \quad \vec{\nabla} \cdot \vec{E} = \frac{\rho}{\epsilon_0} \quad .$$

Using (1) and (2), yields $\Delta V = -\frac{\rho}{\epsilon_0}$.

In one dimension, $f(z)$ only $\Rightarrow \frac{d^2V}{dz^2} = 0$ (no charge, $\rho = 0$) and $\vec{E} = E(z)\vec{z} = -\frac{dV}{dz}\vec{z}$. Therefore, $V(z) = az + b$ with $V(0) = V_0$ and $V(d) = 0$, which yields

$$V(z) = \frac{V_0}{d}(d - z) \forall z \in [0, d] \quad .$$

Table II.10.6: Calculations for the exercise in Sec. II.10.6.1.

Parameter	Symbol or Equation	Value	Unit
Electron kinetic energy	K	10^5	eV
Electron mass	m_e	$5.11 \cdot 10^{-5}$	eV/c ²
Lorentz factor	$\gamma = 1 + \frac{K}{m_e c^2}$	1.196	
Velocity factor	$\beta = \sqrt{1 - \frac{1}{\gamma^2}}$	0.5482	
	$\gamma\beta$	0.6555	
Temperature	T	2000	K
Boltzmann constant	k	$1.38 \cdot 10^{-23}$	J/K
Electron charge	e	$1.6 \cdot 10^{-19}$	C
Light velocity	c	$3 \cdot 10^8$	m/s
	$\sigma_{x'} = \sqrt{\frac{kT}{m_e}}$	$1.06 \cdot 10^{-3}$	m/s
Radius	R	0.005	m
	$\sigma_x = \frac{R}{2}$	0.0025	m
Normalized emittance	$\epsilon_{N,x} = \gamma\beta\sigma_x\sigma_{x'}$	$1.73 \cdot 10^{-6}$	m.rad
Normalized emittance	$\epsilon_{N,x}$	1.73	mm.mrad
Normalized emittance	$\epsilon_{N,x}$	0.553	π .mm.rad

And finally,

$$\vec{E} = \frac{V_0}{d} \vec{z} \quad .$$

II.10.7.3 Solutions to exercise 3 (see Sec. II.10.6.3)

$$m \frac{d\vec{v}}{dt} = q\vec{E} \quad .$$

At one dimension, this leads to

$$m \frac{dv_z}{dt} = q \frac{V_0}{d} \quad \text{along } z \quad ,$$

$$v_z = v = \frac{dz}{dt} \quad ,$$

$$m \frac{dv}{dt} = m \frac{dv}{dz} \frac{dz}{dt} = q \frac{V_0}{d} \quad ,$$

$$\Rightarrow \quad m v dv = q \frac{V_0}{d} dz \quad ,$$

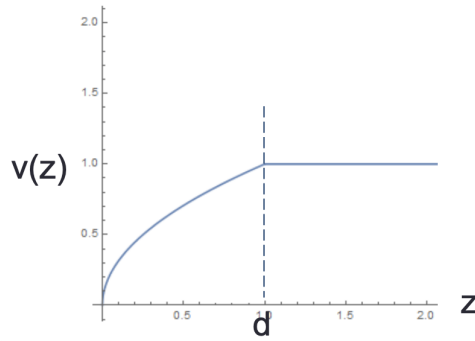
$$\Rightarrow \frac{1}{2} dv^2 = \frac{qV_0}{md} dz \quad ,$$

$$\Rightarrow \frac{1}{2} \int_0^z dv^2 = \frac{qV_0}{md} \int_0^z dz \quad ,$$

$$\Rightarrow v^2(z) - v^2(0) = \frac{2qV_0}{md}(z - 0) \quad ,$$

$$\Rightarrow v(z) = \sqrt{\frac{2qV_0 z}{md}} \quad , \quad z \leq d \quad ,$$

$$v(z) = v(d) \quad \text{if} \quad z > d \quad .$$



II.10.7.4 Solutions to exercise 4 (see Sec. II.10.6.4)

No motion is considered in the x -direction: $x = 0$ and $v_x = 0 \forall t$.

$$\vec{v}_y = v_y \vec{y} \quad \text{at} \quad t = 0 \quad \text{particle at} \quad \begin{cases} y(0) = 0 \\ z(0) = 0 \\ v_y(0) = v_y = \text{const} \\ v_z(0) = 0. \end{cases}$$

$$m \frac{d\vec{v}}{dt} = q\vec{E} \quad \Rightarrow \quad \begin{cases} \frac{dv_y}{dt} = 0 \quad , \quad (1) \\ \frac{dv_z}{dt} = \frac{qV_0}{md} \quad . \quad (2) \end{cases}$$

$$(1) \Rightarrow v_y(t) = \text{const.} = v_y \quad \text{and} \quad \frac{dy}{dt} = v_y \quad , \quad \text{which yields} \quad y(t) = v_y t. \quad (3)$$

$$(2) \Rightarrow v_z(t) = \frac{qV_0}{md}(t - 0). \quad (5)$$

$$\Rightarrow \frac{dz}{dt} = \frac{qV_0 t}{md} \Rightarrow z(t) - z(0) = \frac{qV_0 t^2}{md \cdot 2}. \quad (4)$$

$$\text{Using (3) and (4) yields} \quad y(t) = v_y t = v_y \sqrt{\frac{2mdz(t)}{qV_0}}. \quad (7)$$

$$\text{From Ex. 2, } v_z(z) = \sqrt{\frac{2qV_0 z}{md}} \quad \text{and} \quad v_z(d) = v = \sqrt{\frac{2qV_0}{m}}. \quad (6)$$

Using (6) and (7) yields

$$y(z) = \frac{v_y}{v} 2\sqrt{dz} \quad \forall z \leq d \quad ,$$

and

$$y(d) = \frac{2v_y}{v} d.$$

At $z = d$,

$$\begin{cases} y(d) = \frac{2v_y}{v} d \\ z = d \end{cases} .$$

For $z \geq d$,

$$v_z(t) = \text{const} = \sqrt{\frac{2qV_0}{m}} \quad ,$$

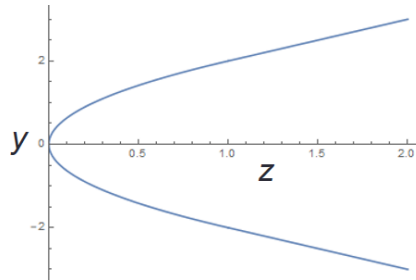
$$z(t') = vt' + d \quad (\text{for } t' \text{ such that } z \geq d; t' = 0 \implies z(t' = 0) = d) \quad ,$$

$$v_y(t') = \text{const} = v_y \Leftrightarrow \frac{dy}{dt} = v_y \quad ,$$

$$y(t') = v_y t' + y(0) \quad .$$

Therefore,

$$y(z) = v_y \frac{z - d}{v} + 2\frac{v_y}{v} d = \frac{v_y}{v} (z + d), \quad z \geq d \quad .$$



II.10.7.5 Solutions to exercise 5 (see Sec. II.10.6.5)

II.10.7.5.1

$$\text{Energy} = \text{const} = \frac{1}{2}mv^2(z) + qV(z) = \frac{1}{2}mv^2(0) + qV(0) = qV_0 \quad ,$$

and therefore,

$$v(z) = \sqrt{\frac{2q(V_0 - V(z))}{m}}, \quad 0 \leq z \leq d \quad . \tag{1}$$

II.10.7.5.2

$$\tilde{\nabla} \cdot \vec{J} = \frac{\partial \rho}{\partial t} \quad ,$$

which, in stationary conditions implies that

$$\tilde{\nabla} \cdot \vec{J} = 0 \quad .$$

For one-dimensional problems, $J = f(z)$ only and therefore it leads to

$$J(z) = J_0 = \text{const.}$$

By definition, $J = \rho v$ and therefore

$$J(z) = J_0 = \rho(z)v(z) = \text{const.} \quad (2)$$

II.10.7.5.3

$$\Delta V = -\frac{\rho}{\epsilon_0} \quad ,$$

which for one-dimensional problems, leads to

$$\frac{d^2 V(z)}{dz^2} = -\frac{\rho(z)}{\epsilon_0} \quad . \quad (3)$$

Using (1) and (2) yields

$$\rho(z) = \frac{J_0}{v(z)} = J_0 \sqrt{\frac{m}{2q}} \cdot \frac{1}{(V_0 - V(z))^{1/2}} \quad . \quad (4)$$

Using (4) and (3) yields

$$\frac{d^2 V(z)}{dz^2} = -\frac{J_0}{\epsilon_0} \sqrt{\frac{m}{2q}} \cdot \frac{1}{(V_0 - V(z))^{1/2}} \quad . \quad (5)$$

Defining $k = \frac{J_0}{\epsilon_0} \sqrt{\frac{m}{2q}}$ and the positive potential

$$U(z) = V_0 - V(z) \geq 0 \quad \forall z \in [0, d] \quad . \quad (6)$$

Therefore,

$$\frac{dU}{dz} = -\frac{dV}{dz} \quad , \quad (7)$$

using (5) and (7), one gets

$$\frac{d^2 U(z)}{dz^2} = \frac{k}{\sqrt{U(z)}} \quad . \quad (8)$$

II.10.7.5.4

$$\vec{E} = -\vec{\nabla} V \quad .$$

$$1\text{D in } z \implies \vec{E}(z) = -\frac{dV}{dz}\vec{z} \quad ,$$

$$\implies E(z) = \frac{dU(z)}{dz} \quad ,$$

$$\frac{d^2U(z)}{dz^2} = \frac{d}{dz}(E(z)) = \frac{dE}{dz} = \frac{dE}{dU} \frac{dU}{dz} = E \frac{dE}{dU} \quad . \quad (9)$$

Using (8) and (9) yields

$$E \frac{dE}{dU} = \frac{k}{U^{1/2}} \implies E dE = k \frac{dU}{U^{1/2}} \quad . \quad (10)$$

II.10.7.5.5

$$(10) \implies \int_{E(0)}^{E(z)} E dE = k \int_{U(0)}^{U(z)} \frac{dU}{U^{1/2}} \quad ,$$

$$\implies \frac{1}{2}E^2(z) - \frac{1}{2}E^2(0) = 2k \left(\sqrt{U(z)} - \sqrt{U(0)} \right) \quad ,$$

$$\implies E^2(z) - E^2(0) = 4k\sqrt{U(z)} \quad . \quad (11)$$

II.10.7.5.6

Space charge upper limit when $E(0) \rightarrow 0$:

$$(11) \implies E^2(z) = \left(\frac{dU}{dz} \right)^2 = 4kU^{1/2} \implies \frac{dU}{dz} = \sqrt{4k}U^{1/4} \quad .$$

$$\int_{U(0)}^{U(d)} \frac{dU}{U^{1/4}} = \sqrt{4k} \int_0^d dz \quad ,$$

$$\implies \left[\frac{4}{3}U^{3/4} \right]_{U(0)}^{U(d)} = \sqrt{4k}(d-0) \quad ,$$

$$U(0) = V_0 - V(0) = 0 \quad \text{and} \quad U(d) = V_0 - V(d) = V_0 \quad .$$

II.10.7.5.7

$$\frac{4}{3}V_0^{3/4} = \sqrt{4k}d \quad ,$$

$$k = \frac{J_0}{\epsilon_0} \sqrt{\frac{m}{2q}} \quad \text{so} \quad \frac{16}{9} \frac{V_0^{3/2}}{d^2} = \frac{4J_0}{\epsilon_0} \sqrt{\frac{m}{2q}} \quad ,$$

which finally gives

$$J_0 = \frac{4}{9} \epsilon_0 \sqrt{\frac{2q}{m}} \cdot \frac{V_0^{3/2}}{d^2} \quad .$$

II.10.7.6 Solution to exercise 6 (see Sec. II.10.6.6)

II.10.7.6.1

The atomic number of ^{39}K potassium ion is $A=39$. The ion mass is

$$M = A.amu = 39 \times 931.49 \text{ MeV}/c^2.$$

The ion kinetic energy of the K^+ ion exiting the source is $K=10$ keV. Let's assume that the ion is relativistic with the usual Lorenz factor γ and velocity β .

$$K = (\gamma - 1)Mc^2 \implies \gamma = 1 + \frac{K}{Mc^2} = 1 + \frac{10^4}{39 \times 931.49 \times 10^6} = 1 + 2.75 \times 10^{-7}.$$

$$\beta = \sqrt{1 - \frac{1}{\gamma^2}} = 0.000742.$$

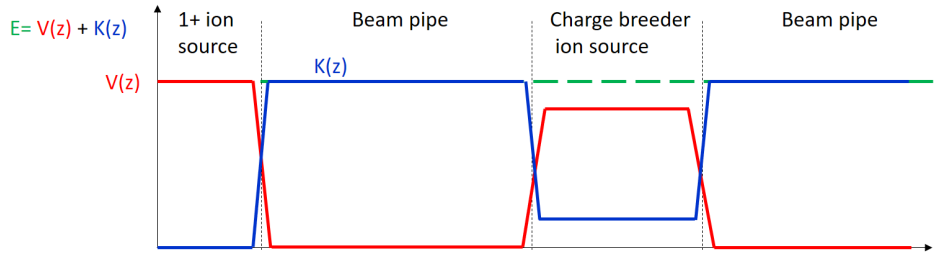
$\beta \ll 1$, so the ion is non-relativistic.

$$v = 2.23 \times 10^5 \text{ m/s}.$$

II.10.7.6.2

The evolution of the ion total energy E (sum of the potential energy $q.V$ and the kinetic energy K) is a constant of motion from the 1^+ source to the Charge breeder. For convenience, the evolution of K and qV is proposed in the following figure.

When the ions enter the charge breeder set to 9.9 keV, they are decelerated to the kinetic en-



ergy $K = 10 - 9.9 = 0.1$ keV. Their new velocity is such that $\frac{1}{2}mv^2 = K = 100$ eV $\implies v = \sqrt{\frac{2K}{m}} = \sqrt{\frac{2 \times 100 \text{ e}}{39 \times 931.49 \times 10^6 \text{ e}/c^2}} = 2.23 \times 10^4 \text{ m/s}$.

II.10.7.6.3

Substituting the kinetic energy of the impacting electron $K = 90$ eV in the simplified Lotz formula, along with the other data provided in the text, gives $\sigma \sim 9.9 \times 10^{-17} \text{ cm}^2$. The mean free path is $\lambda = \frac{1}{\sigma n} = \frac{1}{9.9 \times 10^{-17} \times 10^{12}} \sim 101 \times 10^2 \text{ cm} \sim 101 \text{ m}$.

II.10.7.6.4

In a plasma slab of thickness dx , the number of collision is $\delta N = N(x).n.\sigma.dx$, where $N(x)$ is the remaining number of ions at position x . The infinitely small variation of $N(x)$ relates with δN as $N(x + dx) - N(x) = -\delta N$. The negative sign is due to the fact that $N(x)$ decreases with x (the collisions destroy the 1^+ ions).

$$N(x + dx) - N(x) = dx \cdot \frac{dN}{dx} = -N \frac{x}{\lambda} dx \quad ,$$

$$\begin{aligned} \implies \frac{dN}{N} &= -\frac{dx}{\lambda}, \\ \implies \int_{N(0)}^{N(x)} \frac{dN}{N} &= \int_0^x \frac{dx}{\lambda}, \\ \implies \log\left(\frac{N(x)}{N(0)}\right) &= -\frac{x-0}{\lambda}, \\ \implies N(x) &= N(0)e^{-\frac{x}{\lambda}}. \end{aligned}$$

The ratio of 1^+ ions converted to 2^+ in the plasma of length L is such that $N(L) = N(0)e^{-\frac{L}{\lambda}}$.

At every position x the sum of the 1^+ and 2^+ population is constant $N(0) = N_{1^+}(x) + N_{2^+}(x) = \text{const}$

$$\implies \frac{N_{2^+}}{N(0)} = 1 - \frac{N_{1^+}}{N(0)} \sim 1 - 0.95 \sim 0.05.$$

II.10.7.7 Solution to exercise 7 (see Sec. II.10.6.7)

II.10.7.7.1

The current density J generated by the electron gun is calculated with the corrected Richardson-Dushman equation $J = A_0 \lambda T^2 e^{-W/kT}$, with $A_0 = \frac{4\pi m_e k^2 e}{h^3} = 1.20173 \times 10^6 \text{ A/m}^2/\text{K}$ and $\lambda = 0.24$.

$$\frac{kT}{e} = 8.6 \times 10^{-5} \times 2000 = 0.1723 \text{ eV} \implies J = 1.03 \times 10^6 \text{ A/m}^2.$$

$$\text{The cathode surface is } S = \pi \frac{D^2}{4} = 3.14 \frac{0.004^2}{4} = 1.25 \times 10^{-5} \text{ m}^2.$$

The electron current is $I = J.S \sim 13 \text{ A}$.

II.10.7.7.2

The electron beam diameter D' in the source is such that $\pi \frac{D'^2}{4} = \frac{1}{10} \pi \frac{D^2}{4} \implies D' = \frac{1}{\sqrt{10}} D = 1.26 \text{ mm}$.

The new current density is $J' = \frac{I}{S'} = 10J = 10.3 \times 10^6 \text{ A/m}^2$.

II.10.7.7.3

$$N = N^{1^+}(t) + N^{2^+}(t), \forall t.$$

At $t = 0$, $N^{1^+}(0) = N$ and $N^{2^+}(0) = 0$.

$$\nu = n_e \sigma_{1^+ \rightarrow 2^+} v_e = \frac{J}{e} \sigma_{1^+ \rightarrow 2^+} \text{ (collision frequency)}.$$

$$dN^{1^+} = -N^{1^+}(t) \nu dt \implies N^{1^+}(t) = N e^{-\nu t}.$$

$$\implies N^{2^+}(t) = N(1 - e^{-\nu t}).$$

II.10.7.7.4

$$N^{2^+}(t) = N^{1^+}(t) \implies e^{-\nu t} = \frac{1}{2} \implies t = \tau = \frac{\log(2)}{\nu}.$$

From Tab. II.10.5, one can see that the ionization potential energy to pass from 1^+ to 2^+ is 28 eV. The electron beam energy is 6000 eV. So the electron impact cross section is

$$\sigma_{1^+ \rightarrow 2^+} = 4.5 \times 10^{-14} \times 5 \times \frac{\log\left(\frac{6000}{28}\right)}{6000 \times 28} \sim 7.19 \times 10^{-18} \text{ cm}^2.$$

$$\nu = \frac{10.3 \times 10^2}{1.6 \times 10^{19}} \times 7.19 \times 10^{-18} = 46.4 \text{ kHz},$$

$$\implies \tau \sim 14.9 \mu\text{s}.$$

II.10.7.7.5

The electron beam kinetic energy is set to 900 eV. From Tab. II.10.5, one can see that the highest achievable charge state is Ar^{15^+} as the IP to pass from 14^+ to 15^+ is 855 keV, while the next level

is 918 > 900 eV.

References

- [1] R. Nagai, R. Hajima, and N. Nishimori, Magnetic emittance suppression using a bucking coil for a dc photocathode electron gun, *Rev. Sci. Instrum.* 83, 123303 (2012), [doi:10.1063/1.4772397](https://doi.org/10.1063/1.4772397).
- [2] F. Muraz, et al., *Nucl. Instrum. and Meth. in Phys. Res. Sect. A: Accelerators, Spectrometers, Detectors and Associated Equipment*, Vol. 1062, 2024, 169214, ISSN 0168-9002, [doi:10.1016/j.nima.2024.169214](https://doi.org/10.1016/j.nima.2024.169214).
- [3] G. Gaertner, W. Knapp, R. G. Forbes, *Modern Developments in Vacuum Electron Sources*, 2020, Topics in Applied Physics, Springer, Volume 135, ISBN: 978-3-030-47290-0.
- [4] C. J. Smithells, *Metals Reference Book*, Vol III, Butterworths, London, 1967, 737ff.
- [5] P. D. Frost, O.T. Purl and H. R. Johnson, "Electron guns for forming solid beam of high-perveance and high-convergence", *Proc. IRE.* Vol. 50, pp1800-1807; August, 1962.
- [6] Luigi Faillace, *Recent Advancements of RF Guns*, *Physics Procedia*, Vol. 52, 2014, pp. 100-109, [doi:10.1016/j.phpro.2014.06.015](https://doi.org/10.1016/j.phpro.2014.06.015).
- [7] R. H. Fowler and L. Nordheim, "Electron emission in intense electric fields," *Proc. R. Soc. Lond. A, Math. Phys. Sci.*, vol. 119, no. 781, pp. 173–181, May 1928.
- [8] F. Charbonnier, Developing and using the field emitter as a high-intensity electron source, *Appl. Surf. Scienc.*, Vol. 94–95, 1996, pp 26-43, ISSN 0169-4332, [doi:10.1016/0169-4332\(95\)00517-X](https://doi.org/10.1016/0169-4332(95)00517-X).
- [9] C.A. Spindt (1968), "A Thin-Film Field-Emission Cathode", *Journal of Applied Physics*. AIP Publishing. 39 (7): 3504–3505, ISSN 0021-8979, [doi:10.1063/1.1656810](https://doi.org/10.1063/1.1656810).
- [10] Asish Kumar Singh, Sushil Kumar Shukla, Meduri Ravi and Ranjan Kumar Barik, A Review of Electron Emitters for High-Power and High-Frequency Vacuum Electron Devices, *IEEE TRANSACTIONS ON PLASMA SCIENCE*, VOL. 48, NO. 10, OCTOBER 2020.
- [11] K.L. Jensen et al., *Jour. Appl. Phys.* 107, 014903 (2010).
- [12] Carlos Hernandez-Garcia, Patrick G. O'Shea, Marcy L. Stutzman, Electron sources for accelerators, *Physics Today* 1 February 2008, 61 (2): 44–49 [doi:10.1063/1.2883909](https://doi.org/10.1063/1.2883909).
- [13] Jana Schaber, Rong Xiang and Nikolai Gaponik, Review of photocathodes for electron beam sources in particle accelerators, *J. Mater. Chem. C*, 2023, 11, 3162-3179, [doi:10.1039/D2TC03729G](https://doi.org/10.1039/D2TC03729G).
- [14] T. Nishitani et al., JAEA Photocathode DC-Gun for an ERL Injector, jacow online proceedings, TUPPH007, p. 319, Proceedings of FEL 2006, BESSY, Berlin, Germany.
- [15] N. Nishimori et al., DEVELOPMENT OF A PHOTOEMISSION DC GUN AT JAEA, MOPD53, p. 161, Proceedings of FEL2012, Nara, Japan.
- [16] I. Martini, Characterization of Cs-Sb cathodes for high-charge RF photoinjectors, Politecnico di Milano, February 2016, CERN-THESIS-2016-143.
- [17] S.V. Kuzikov, S.P. Antipov, P.V. Avrakhov, E. Dosov, C.-J. Jing, E.W. Knight, G. Ha, W. Liu, P. Piot, J.G. Power, D.S. Scott, J.H. Shao, E.E. Wisniewski, X. Lu, W.H. Tan, "An X-Band Ultra-High Gradient Photoinjector", *IPCA2021*, [doi:JACoW-IPAC2021-WEPA163.html](https://doi.org/10.1063/1.5111111).

- [18] T.G. Lucas, X.F.D. Stragier, P.H.A. Mutsaers, O.J. Luiten, RF design of a compact, X-band travelling-wave RF photogun made from halves, *Nuclear Inst. and Methods in Physics Research, A* 1013 (2021) 165651.
- [19] Grames, J., Poelker, M. (2023). Polarized Electron Sources. In: Méot, F., Huang, H., Ptitsyn, V., Lin, F. (eds) *Polarized Beam Dynamics and Instrumentation in Particle Accelerators. Particle Acceleration and Detection*. Springer, Cham, [doi:10.1007/978-3-031-16715-7_11](https://doi.org/10.1007/978-3-031-16715-7_11).
- [20] Maruyama, T.; Luh, D.; Brachmann, A.; Clendenin, J. E.; Garwin, E. L.; Harvey, S.; Jiang, J.; Kirby, R. E.; Prescott, C. Y.; Prepost, R.; Moy, A. M., Polarized Electron Emission from Strained GaAs/GaAsP Superlattice Photocathodes, SPIN 2004, Proceedings of the 16th International Spin Physics Symposium and Workshop on Polarized Electron Sources and Polarimeters, 10-16 October 2004, Trieste, Italy. Published by World Scientific Publishing Co. Pte. Ltd., 2005. ISBN #9789812701909, pp. 917-921.
- [21] <https://alpha.web.cern.ch/science/antiproton-source>.
- [22] Diktys Stratakis and David V Neuffer, *J. Phys. G: Nucl. Part. Phys.* 41 125002 (2014), [doi:10.1088/0954-3899/41/12/125002](https://doi.org/10.1088/0954-3899/41/12/125002).
- [23] <http://www.ne.ncsu.edu/nrp/ips.html>.
- [24] R. W. Pringle, H. W. Taylor, and K. I. Roulston, Radiative Capture of Thermal Neutrons by Cd113, *Phys. Rev.* 87, 1016 (1952).
- [25] L. Rinolfi *et al.*, “Brilliant positron sources for CLIC and other collider projects” CERN-OPEN-2013-022 ; CLIC-Note-985, *Nucl. Instrum. Methods Phys. Res., B* Presented at 5th International Conference on charged and neutral particles channeling phenomena, Alghero, Italy, 23–28 Sep 2012, <https://cds.cern.ch/record/1602023/files/CERN-OPEN-2013-022.pdf>.
- [26] Bernhard Wolf, *Handbook of ion sources*, CRC Press, 1995. ISBN 0849325021, 9780849325021.
- [27] I.G. Brown, *The Physics and Technology of Ion Sources*, Wiley, ISBN:9783527404100, [doi:10.1002/3527603956](https://doi.org/10.1002/3527603956).
- [28] M.J. Dresser, "The Saha-Langmuir Equation and its Application" (PDF), *Journal of Applied Physics.* 39 (1): 338–339 (1968), [doi:10.1063/1.1655755](https://doi.org/10.1063/1.1655755).
- [29] Dan Faircloth and Scott Lawrie, An overview of negative hydrogen ion sources for accelerators, 2018, *New J. Phys.* 20 025007.
- [30] Chou S H and Voss J, An orbital-overlap model for minimal work functions of cesiated metal surfaces, *J. Phys.: Condens. Matter* 24 445007 (2012).
- [31] X-RAY DATA BOOKLET, Lawrence Berkeley National Laboratory, USA, <https://xdb.lbl.gov/>.
- [32] Thomas A. Carlson, C. W. Nestor, IR., Neil Wasserman, and J. D. McDowell, Calculated ionization potentials for multiply charged ions, *Atomic Data*, 2, 63-99 (1970).
- [33] W. Lotz, An empirical formula for the electron-impact ionization cross-section. *Z. Physik* 206, 205–211 (1967), [doi:10.1007/BF01325928](https://doi.org/10.1007/BF01325928).
- [34] W. Lotz, Electron-impact ionization cross-sections and ionization rate coefficients for atoms and ions from hydrogen to calcium, *Z. Physik* 216, 241–247 (1968), [doi:10.1007/BF01392963](https://doi.org/10.1007/BF01392963).

- [35] Alfred Müller, Erhard Salzborn, Scaling of cross sections for multiple electron transfer to highly charged ions colliding with atoms and molecules, *Physics Letters A*, Vol. 62, Issue 6 (1977), pp. 391-394, [doi:10.1016/0375-9601\(77\)90672-7](https://doi.org/10.1016/0375-9601(77)90672-7).
- [36] A.A. Sorokin, L.A. Shmaenok, S.V. Bobashev, B. Möbus, M. Richter, and G. Ulm, Measurements of electron-impact ionization cross sections of argon, krypton, and xenon by comparison with photoionization, *Phys. Rev. A* 61, 022723 (2000).
- [37] H. A. Kramers. On the theory of X-ray absorption and of the continuous X-ray spectrum, *Philos. Mag.*, 46:836, 1923.
- [38] M.F. Gu, *Astrophysical Journal*, Radiative Recombination Rate Coefficients for Bare through F-like Isosequences of Mg, Si, S, Ar, Ca, Fe, and Ni, 589:1085-1088 (2003).
- [39] Y. Hahn and D. W. Rule. Direct radiative capture of high-energy electrons by atomic ions. *J. Phys. B. At. Mol. Phys.*, B10:2689, 1977.
- [40] Ali, S. (2012). Electron - Ion Recombination Data for Plasma Applications - Results from Electron Beam Ion Trap and Ion Storage Ring (PhD dissertation, Department of Physics, Stockholm University).
- [41] J. Lettry, M. Kronberger, R. Scrivens, E. Chaudet, D. Faircloth, G. Favre, J.-M. Geisser, D. Küchler, S. Mathot, O. Midttun, M. Paoluzzi, C. Schmitzer, D. Steyaert; High duty factor plasma generator for CERN's Superconducting Proton Linac. *Rev. Sci. Instrum.* 1 February 2010; 81 (2): 02A723, [doi:10.1063/1.3277188](https://doi.org/10.1063/1.3277188).
- [42] G.D. Shirkov, « A classical model of ion confinement and losses in ECR ion sources », *Plasma Sources Sci. Technol.* 2(1993) 250-257.
- [43] R. G. Wilson, Surface Ionization Ion Sources, in *IEEE Transactions on Nuclear Science*, vol. 14, no. 3, pp. 72-74, June 1967, [doi:10.1109/TNS.1967.4324525](https://doi.org/10.1109/TNS.1967.4324525).
- [44] G.D. Alton, Sources of Low-Charge-State Positive-Ion Beams, *Methods in Experimental Physics*, Academic Press, Vol. 29, Part A, 1995, pp. 69-168, ISSN 0076-695X, ISBN 9780124759749, [doi:10.1016/S0076-695X\(08\)60654-7](https://doi.org/10.1016/S0076-695X(08)60654-7).
- [45] T. Stora, Radioactive Ion Sources (2014). CAS-CERN Accelerator School: Ion Sources - Proceedings. 10.5170/CERN-2013-007.331.
- [46] M.C. Chen, Y. C. Kuo, Indirect hot cathode ion source, US Patent, US6348764B1, Feb. 19, 2002.
- [47] R. Hollinger, M. Galonska, B. Gutermuth, F. Heymach, H. Krichbaum, K.-D. Leible, K. Ochs, P. Schäffer, S. Schäffer, P. Spädtke, M. Stork, A. Wesp, R. Mayr; Status of high-current ion source operation at the GSI accelerator facility. *Rev. Sci. Instrum.* 1 February 2008; 79 (2): 02C703, [doi:10.1063/1.2801623](https://doi.org/10.1063/1.2801623).
- [48] European Patent EP 2704535 A1 20140305 (EN), <https://data.epo.org>.
- [49] <https://home.cern/fr/science/experiments/isolde>.
- [50] S. Sundell, H. Ravn, Ion source with combined cathode and transfer line heating, *Nucl. Instr. and Methods in Phys. Res. Sec. B: Beam Interactions with Materials and Atoms*, Vol. 70, Issues 1-4, 1992, pp. 160-164, [doi:10.1016/0168-583X\(92\)95926-I](https://doi.org/10.1016/0168-583X(92)95926-I).
- [51] V. Fedosseev et al, 2017, *J. Phys. G: Nucl. Part. Phys.* 44 084006, [doi:10.1088/1361-6471/aa78e0](https://doi.org/10.1088/1361-6471/aa78e0).

- [52] M. Bacal, M. Sasao, and M. Wada, Negative Ion Sources, *Appl. Phys.* 129, 221101 (2021), [doi:10.1063/5.0049289](https://doi.org/10.1063/5.0049289).
- [53] Yu.I. Belchenko et al, A powerful injector of neutrals with a surface-plasma source of negative ions, 1974 *Nucl. Fusion* 14 113.
- [54] James G. Alessi; Performance of the Magnetron H- Source on the BNL 200 MeV Linac. *AIP Conf. Proc.* 2 December 2002; 642 (1): 279–281, [doi:10.1063/1.1522646](https://doi.org/10.1063/1.1522646).
- [55] R. Keller; R. Thomae; M. Stockli; ,Design, Operational Experiences and Beam Results Obtained with the SNS H- Ion Source and LEBT at Berkeley Lab, *AIP Conf. Proc.* 639, 47–60 (2002), [doi:10.1063/1.1517905](https://doi.org/10.1063/1.1517905).
- [56] R.F. Welton et al, Recent H- ion source research and development at the Oak Ridge National Laboratory, 2023 *JINST* 18 C12011, [doi:10.1088/1748-0221/18/12/C12011](https://doi.org/10.1088/1748-0221/18/12/C12011).
- [57] T. Taylor and J. Mouris, An advanced high-current low-emittance dc microwave proton source, *NIM A* 336 (1993) 1 – 5.
- [58] O. Tuske, G. Adroit, O. Delferrière, J-F. Denis, Y. Gauthier, P. Girardot, R. Gobin, F. Harrault, P. Graehling, P. Guiho, J. Hosselet, C. Maazouzi, Y. Sauce, D. Uriot, T. Vacher, C. Van Hille; Light ion source for proton/deuteron production at CEA Saclay for the Spiral2 project. *Rev. Sci. Instrum.* 1 February 2012; 83 (2): 02A316, [doi:10.1063/1.3665963](https://doi.org/10.1063/1.3665963).
- [59] R. Geller, *Electron Cyclotron Resonance Ion Sources and ECR Plasmas*. Institute of Physics Publishing, Bristol (1996).
- [60] G. Machicoane, N.K. Bultman, G. Morgan, E. Pozdeyev, X. Rao, J.Y. Benitez, C.M. Lyneis, L.T. Sun, Design Status of ECR Ion Sources and LEBT for FRIB, THYO03, Jacow online proc., *ECRIS2012*, Sydney, Australia.
- [61] E. D. Donets, V. I. Ilushenko and V. A. Alpert, Ultrahigh-vacuum electron beam ion source of highly stripped ions, *Proc. First Int. Conf. on Ion Sources*, Saclay, France, 1969, p. 635.
- [62] G. Zschornacka, M. Schmidt, A. Thorn, *Electron Beam Ion Sources*, CAS - CERN Accelerator School, Ion Sources, pp.165-201, [doi:10.5170/CERN-2013-007](https://doi.org/10.5170/CERN-2013-007).
- [63] T. Kanesue, E. Beebe, B. Coe, S. Ikeda, S. Kondrashev, A. Lopez-Reyes, M. Okamura, R. Schoepfer, T. Rodowicz, Operation experience of LION and RHIC-EBIS for RHIC and NSRL, *Journal of Physics: Conference Series*, 2244 (2022) 012101.
- [64] J. Alessi, E. Beebe, S. Bellavia, O. Gould, A. Kponou, R. Lambiase, R. Lockey, D. McCafferty, M. Okamura, A.I. Pikin, D. Raparia, J. Ritter, L. Snyderstrup, A HIGH-PERFORMANCE ELECTRON BEAM ION SOURCE, WE-11, *Jacow online proceedings*, HIAT09, Venice, Italy (2009).
- [65] F. Wenander, Charge breeding of radioactive ions with EBIS and EBIT, *CERN-ATS-Note-2011-010 MD*, [doi:10.1088/1748-0221/5/10/C10004](https://doi.org/10.1088/1748-0221/5/10/C10004).